Advanced Silicon Anode Architectures for High Energy Density Lithium-ion Batteries

by

Rasim Batmaz

A thesis

presented to the University of Waterloo

in fulfillment of the

thesis requirement for the degree of

Doctor of Philosophy

in

Chemical Engineering

Waterloo, Ontario, Canada, 2018

Examining Committee Membership

The following served on the Examining Committee for this thesis. The decision of the Examining Committee is by majority vote.

External Examiner   Dr. Zhibin Ye

                                      Professor

Supervisor   Dr. Zhongwei Chen

                                      Professor

Internal Member   Dr. Mark Pritzker

                                      Professor

Internal Member   Dr. Ting Tsui

                                      Professor

Internal-External Member   Dr. Zhongchao Tan

                                      Professor

AUTHOR'S DECLARATION

This thesis consists of material all of which I authored or co-authored: see Statement of Contributions included in the thesis. This is a true copy of thesis, including any required final revisions, as accepted by my examiners.

I understand that my thesis may be made electronically available to the public.

Statement of Contributions

The body of thesis is based upon a combination of published and unpublished works. Various chapters are adapted from the following list of publications.

Chapter 4 of this thesis consists of a paper that was co-authored by myself, my supervisor, a PhD student, Mr. F. Hassan, two post-doctoral fellows, Drs. J. Li and X. Wang, and two collaborators, Drs. A. Yu and X. Xiao. Mr. F. Hassan and I designed the experiment together with supervision of Dr. Z. Chen. I and Mr. F. Hassan carried out the lab experiments, collected and analyzed the experimental data. Dr. J. Li performed the DFT calculations. Dr. X. Wang assisted with some of the electrochemical measurements. Drs. Z. Chen and X. Xiao supervised the project.

"Evidence of covalent synergy in silicon–sulfur–graphene yielding highly efficient and long-life lithium-ion batteries." *Nature communications* 6 (2015): 8597.

Chapter 5 of this thesis consists of an accepted paper by that was co-authored by myself, my supervisor, two post-doctoral fellows, Drs. F. Hassan and D. Higgins, a PhD student, Mr. Z. Cano and a collaborator, Dr. X. Xiao. I and Dr. F. Hassan designed and carried out the experiment, collected and analyzed the data, as well as the writing of the manuscript. Dr. D. Higgins and Mr. Z. Cano reviewed the manuscript and assisted with the writing of the manuscript. Drs. Z. Chen and X. Xiao supervised the project.

"Highly Durable 3D Conductive Matrixed Silicon Anode for Lithium-ion Batteries."
*Journal of Power Source*s, POWER-D-18-01738R2, accepted.

Chapter 6 of this thesis consists of an unpublished paper that was co-authored by myself, my supervisor, a post-doctoral fellow, Dr. F. Hassan and a PhD student, Mr. M. Li. I and Dr. F. Hassan designed and carried out the experiment, collected and analyzed the data, as well as the writing of the manuscript. Mr. M. Li assisted with the writing of the manuscript. Dr. Z. Chen supervised the project.

"In-Situ Partial Binder Graphenization Revolutionize the Use of Metallurgical Silicon for Lithium-ion Batteries." is under preparation for submission.

Abstract

The pressing environmental issues and the continuous increase in energy demand have drawn tremendous attention to the development of advanced electrochemical energy storage systems (EESS). Lithium-ion batteries are currently the most developed EESS; however, they are insufficient to meet the requirements of energy intensive applications such as electric vehicles. This stems from the intrinsic limitations of commercial cathode and anode materials. Therefore, their electrochemical properties should be either improved by applying new fabrication techniques or replaced with new generation materials to increase their energy density, power density and stability.

Silicon is a promising candidate as a new generation anode material due to its enormous theoretical lithium storage capacity. However, silicon faces some technological hurdles such as poor cycle stability and rate capability. This stems from its intrinsic low electrical conductivity, severe volume change upon reaction with lithium, leading to loss of electrode integrity and formation of an unstable solid electrolyte interphase. In an attempt to address these problems, the proposed research projects have been embodied in this thesis. The main focus of these projects includes: enhancing electronic conductivity, forming stable electrolyte interphase and preventing electrode structural failure. To achieve these goals, novel silicon-carbon composite materials in which the silicon particles were hosted by nano-architectured carbon scaffolds were prepared to improve the electronic conductivity and help form a stable electrolyte interphase. Furthermore, to prevent electrode structure failure, the electrodes prepared from these silicon-carbon composite materials were subjected to thermal treatment to alter the electrode architecture by tuning the chemical structure of the binder.

In Chapter 4, an advanced silicon electrode was developed by using commercially available silicon nanoparticles (SiNPs) as the anode material and sulfur-doped graphene (SG) as a carbon support. The electrode slurry was prepared by mixing these components with polyacrylonitrile (PAN) binder and then applied to the current collector. After the electrodes were dried, a thermal treatment was applied to reconstruct the architecture of the electrodes. In this new electrode architecture, PAN polymer is turned into an aromatic structure (cPAN) with 6-membered rings hosting the nitrogen atoms in pyridinic position. Thus, after the treatment, SiNPs are surrounded by the 3D conductive hierarchical architecture of SG sheets and the aromatic structure of cPAN. It was found that the silicon atoms on the nanoparticle surfaces anchor to and covalently interact with the sulfur and nitrogen atoms of this carbonaceous nanoarchitecture. This prevents the agglomeration of silicon particles, maintains the electrode integrity and stabilizes the solid electrolyte interphase leading to a superior reversible capacity of over 1000 mAh g^{-1} for 2275 cycles at 2.0 A g^{-1}. The excellent performance combined with the simple, scalable and non-hazardous approach render the process as a very promising candidate for lithium-ion battery technology. This lays the basis for the project in Chapter 5. Although a high-performance anode was obtained by utilizing commercially available silicon nanoparticles, the high-cost of nanoparticles hinders the commercialization. To address this challenge, we have fabricated a stable silicon-based anode using low-cost silicon micron particles (SiMPs) by developing a two-step top-down approach. Wet-milling of SiMPs within an electrode precursor slurry (sulfur-doped graphene (SG), polyacrylonitrile (PAN) in dimethylformamide) allows for nanostructuring of the silicon by a straightforward and scalable process. After casting the electrode precursor slurry on the current collector, the electrodes are

annealed to achieve an ideally tuned SG-SiMPs-cPAN electrode structure. In this structure, the polymer binder (PAN) is converted into a 3D aromatic network of cPAN that wraps the silicon particles and forms micron-sized channels throughout the electrode structure. These micro-channels act as a mechanical buffer for the anisotropic volume changes of silicon particles during battery charging/discharging, thereby preventing electrode pulverization. This electrode structure delivers excellent capacity (3081 mAh g^{-1} at 0.1 A g^{-1}) in addition to good rate capabilities and cycle life (1423 mAh g^{-1} at 2.0 A g^{-1} for 500 cycles). Furthermore, the efficiency of this technique makes it possible to expand its application to other anode materials that require mechanical robustness and electrical conductivity with the goal of preparing next generation lithium-ion batteries.

With a practical goal of fabricating low cost, scalable and facile silicon electrodes, we have removed sulfur-doped graphene from the electrode recipe of Chapter 5 and eliminated ball-milling. In this study, metallurgical-sized silicon is used as the anode material. The electrodes deliver an areal capacity of 3.0 mAh cm^{-2} at 0.1 A g^{-1} and more than 1.5 mAh cm^{-2} at 2.0 A g^{-1} for high loading electrodes. For moderate loadings, 1030 mAh g^{-1} (0.5 mAh cm^{-2}) is achieved after 250 cycles at 2.0 A g^{-1}. This excellent performance is attributed to the post-annealing of electrodes in which the in-situ binder graphenization of PAN takes place, leading a 3D robust electrode architecture. The mSiPs are hosted within this architecture which serves as an electron pathway with its π-conjugated aromatic structure and provides channels on the electrode surface to guarantee electrolyte penetration for good ionic conductivity. The partial graphenization of PAN can help to maintain its elastic properties required to accommodate large volume expansion of mSiPs and maintain the electrode integrity. This may lead to the

formation of stable SEI that enables good cycling and rate performance. Furthermore, our approach is compatible with industrial slurry fabrication technique and open to be adopted to other electrode materials.

Acknowledgements

I would like to first thank my supervisor Dr. Zhongwei Chen who gave me the opportunity to study such an exciting project and guided me throughout my PhD studies. He did not let me to give up when I was overwhelmed with personal problems and academic challenges. I would like to next thank to his amazing group consisted of outstanding colleagues such as Dr. Yining Zhang, Pan Xu, Jing Zhang, Dr. Xiaogang Fu, Dr. Jing Fu, Matthew Li, Dr. Pouyan Zamani, Abel Sy, Dr. Xiaolei Wang and Dr. Fathy Hassan. Their support had been crucial to my academic success and appreciating my last five years.

I would also like to thank my PhD examining committee, including Professor Mark Pritzker, Professor Michael Fowler, Professor Zhongchao Tan, Professor Ting Tsui and Professor Zhibin Ye for their time and contributions through this important process.

Moreover, I would like to give my special thanks to Dr. Fathy Hasan for his constant support and motivation with my academic research and for his friendship during my hard times. To meet him was a blessing in my life, hope to keep in touch rest of my life.

I would like to acknowledge my lovely wife, Sumeyye Batmaz, her family and my family most gratefully. Sumeyye was like a harbor that I disburdened all my worries and anxieties during the last five years. Hope she would enjoy the life more after my PhD.

Finally, all thanks to the ONE…

Table of Contents

List of Figures

List of Tables

Chapter 1 Introduction

1.1 Challenges and Motivation

The rechargeable lithium-ion (Li-ion) battery is a member of the electrochemical class of energy storage systems. It is superior to present battery systems such as nickel-cadmium, nickel metal hydride, zinc-manganese in terms of its high volumetric and gravimetric energy density, fast charging and discharging ability, low self-discharge and lower tendency for memory effect. Therefore, it has dominated the market of portable devices such as smart phones, laptop computers and digital cameras. Moreover, it is a very strong candidate for use with alternative clean energy technologies, such as solar and wind, to decrease the dependency on petroleum. However, the-state-of-the-art of commercial Li-ion batteries is not able to meet the demands of these technologies.

The performance of a battery depends on anode, cathode, separators, electrolytes and overall cell and stack design. The active material embedded within the cathode and anode plays the most important role in the energy density, power density and cycle stability of a lithium-ion battery. The current batteries primarily use micron-sized graphite as the anode and $LiCoO_2$ as the cathode, which will have to be replaced with superior anode and cathode materials to meet the future requirements.

The element silicon (Si) can be utilized as an active material in order to provide higher energy density than that of conventional anode (graphite). The theoretical specific capacity of silicon is almost 10 times higher than that possible with graphite. This stems from the fact that it operates via a different mechanism from graphite in incorporating Li^+. Moreover, it is

abundant, environmentally-safe and inexpensive. However, 2 major challenges to be addressed prior to the real application:

1. Severe volume change (>300%) upon lithium insertion and extraction which results in material pulverization, loss of electrode integrity and eventual capacity loss.

2. Low colombic efficiency and unstable solid electrolyte interphase (SEI).

1.2 Thesis Objectives and Approaches

The ultimate objective of this research project is to develop a facile and scalable method to fabricate advanced silicon anodes for use in high energy density lithium-ion batteries. To accomplish this the following approaches were pursued:

1. Preparation of silicon nanoparticle/sulfur-doped graphene composites

   - We discovered from this project that sulfur-doped graphene (SG) can be used to wrap silicon nanoparticles and this composite structure can be sealed with cyclized polymer using a gentle heat treatment. The developed structure shows a strong covalent interaction between the silicon nanoparticles and SG leading to the spatial rearrangement of SiNPs within the graphene layers. This resulted in excellent cycling performance. To decrease the cost of this electrode and eliminate the challenges using nanosilicon particles, we focused on the use of micron-sized silicon instead.

2. Preparation of nano-architectured anode material from silicon micron particles

   - We learned from this project that ball-milling of micron-sized silicon particles slurry can be used as a top-down method to prepare a nanostructured silicon

2

electrode. Furthermore, heat treatment of electrodes leads the formation of a 3D conductive anode matrix with micro-channels. This engineered matrix yields an electrode structure with excellent mechanical robustness which can accommodate large volumetric changes. The success of this project encouraged us to move onto electrodes derived from metallurgical size silicon without any carbon additive other than binder.

3. In-situ partial binder graphenization revolutionize the use of metallurgical silicon for lithium-ion batteries

- We learned from this project that polyacrylonitrile (PAN) can be used as a binder and a conductive additive after subjected to post thermal treatment. This is due to the formation of a nitrogen-doped graphene-like matrix surrounding the silicon particles. The stress generated by the severe volume change of silicon particles during cycling is buffered by the flexibility of the graphene-like medium. Furthermore, the covalent bonds between the nitrogen atoms of PAN and silicon atoms on the surface of the particles provide intimate contact preventing the loss of active material during cycling. Thus, we were able to utilize metallurgical silicon particles as the anode material. This encourages us to further study this commercially available polymer to simplify the fabrication techniques for metallurgical silicon anodes.

1.3 Structure of Thesis

This thesis consists of several chapters. **Figure 1-1** depicts a simplified breakdown of the work described in this thesis. **Chapter 1** provides an introduction which covers the motivation and objectives of the work. In **Chapter 2**, a detailed review of the relevant literature is provided. **Chapter 3** covers the physicochemical and electrochemical characterization techniques used in this thesis. **Chapter 4** focuses on the development of a scalable advanced negative electrode relying on commercially available Si nanoparticles (SiNPs) and sulfur-doped graphene (SG). The battery performance of the developed electrode is elucidated. **Chapter 5** describes an effort to make an effective negative electrode without using silicon nanoparticles by replacing with micron-sized particles. It introduces the concept of milling the electrode slurry as a top-down approach for nanoscaling of micron-sized silicon particles. **Chapter 6** focuses on the binder graphenization using a one-pot thermal treatment. The engineered binder possesses enough flexibility and conductivity to be coupled with metallurgical silicon and provides good battery performance. Finally, **Chapter 7** contains the summary and conclusions of the thesis, along with the recommendations for future directions to exploit the achievements of this research for further improvements of lithium-ion battery performance.

Chapter 4
- **Commercial silicon nanoparticles**
- **Sulfur-doped graphene**
- **Silicon-sulfur covalent synergy**

200 nm
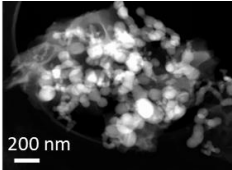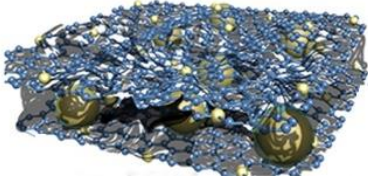
Chapter 5
- **Micron-sized silicon particles**
- **Top-down approach**
- **Slurry milling for particle size reduction**

5µm

200 nm
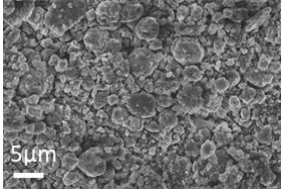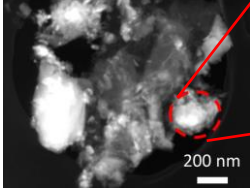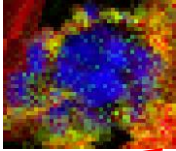
Silicon: Blue
Carbon: Red
Nitrogen: Green

Chapter 6
- **Metallurgical silicon particles**
- **In-situ binder graphenization**

40 µm

Carbon layer

Silicon (111)
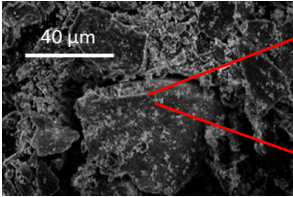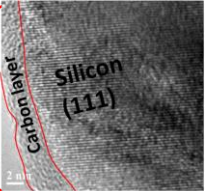
Figure 1-1 Schematic illustration of the research workflow throughout this thesis.

Chapter 2 Literature Review

2.1 Electrochemical Energy Storage Systems

The growing economic, environmental and ecological problems with fossil fuels have driven the urgent need for breakthroughs in electrochemical energy storage systems to pursue renewable energies. Batteries, fuel cells and electrochemical supercapacitors (ECs) are three main systems that can be used to convert chemical energy to electrical energy. Although their energy storage and conversion mechanisms are different, they exhibit some electrochemical similarities. First, all of these systems consist of two electrodes in contact with an electrolyte. The electrolyte must only conduct ions but not electrons to force different conduction pathways for the ions and the electrons and prevent short circuiting. Second, the energy providing mechanism occurs at the electrode/electrolyte interface.

In batteries and fuel cells, chemical energy is converted to electrical energy by redox reactions (Faradaic process); however, in ECs, an accumulation of ions (non-Faradaic process) takes place at the electrical double layer (EDL). The main difference between batteries and fuel cells is their mode of operation. Batteries, other than flow batteries, are closed systems so that the active materials providing the energy must be embedded within the electrodes. Thus, the energy storage and conversion take place in the same compartments. On the other hand, fuel cells are open systems where the active materials undergoing the redox reactions are supplied from a tank or the environment. Therefore the energy storage (in the tank) and energy conversion (electrodes) occurs at different locations[1].

6

2.2 The Basics of Battery Chemistry

The smallest unit of a device converting chemical energy to electrical energy is called an electrochemical cell. Usually, a battery refers to a connection of multiple electrochemical cells but may also be used to refer a single cell. Each cell contains a positive terminal, a negative terminal, a separator and an electrolyte which is either a liquid or a gel filling the space between these electrodes. The potential difference between the anode and cathode creates an electromotive force (V) to drive the redox reactions at each electrode.

In a discharging cell, an oxidation reaction (A $\rightarrow$ A$^+$ + e$^-$) occurs at the negative electrode. This generates positive ions and electrons. The generated electrons pass through the external circuit and engage in a reduction reaction at the cathode with the positive ions present at the electrolyte (B$^+$ + e$^-$ $\rightarrow$ B). The separator is an electrically insulating but ionically conducting physical barrier between the anode and cathode to prevent a short-circuit. The electrolyte is a medium where ions can easily flow and serves as an ionic conductor to allow ions to be transported to and from the electrodes and complete the electrical circuit.

A battery is defined as primary if it is designed to be used until exhausted and then discarded. Primary batteries are not recharged. Therefore, they should be assembled and manufactured in the charged state, ready to be discharged. On the other hand, secondary batteries can be restored to its original state after being discharged by applying an electric current in the direction opposite to the flow of current when the cell is discharged. They are usually assembled in discharged state and have to be charged prior to use.

2.3 Lithium-ion Batteries

2.3.1 A Brief History

The motivation for developing a high energy density electrochemical energy storage system based on lithium metal stems from the fact that lithium is the most electropositive (-3.04 V versus standard hydrogen electrode) and the lightest metal (molecular weight of lithium is 6.94 g mol^{-1} at a density of 0.53 g cm^{-3}) [2]. **Figure 2-1** illustrates the superiority of lithium-based batteries including lithium-metal, lithium-ion, and polymeric lithium-ion over traditional batteries such as lead-acid, nickel-cadmium in terms of energy density. The first non-rechargeable lithium batteries were developed in the 1970s [3]. Since they had high capacity and adjustable discharge rates, they easily found applications as power sources in many fields such as watches, calculators and implantable medical devices. In the meantime, it was discovered that various inorganic compounds can react reversibly with alkali metals, making it possible to produce rechargeable systems. These compounds were later identified as intercalation compounds. This discovery enabled the breakthrough in the development of Li-based rechargeable energy storage technology.
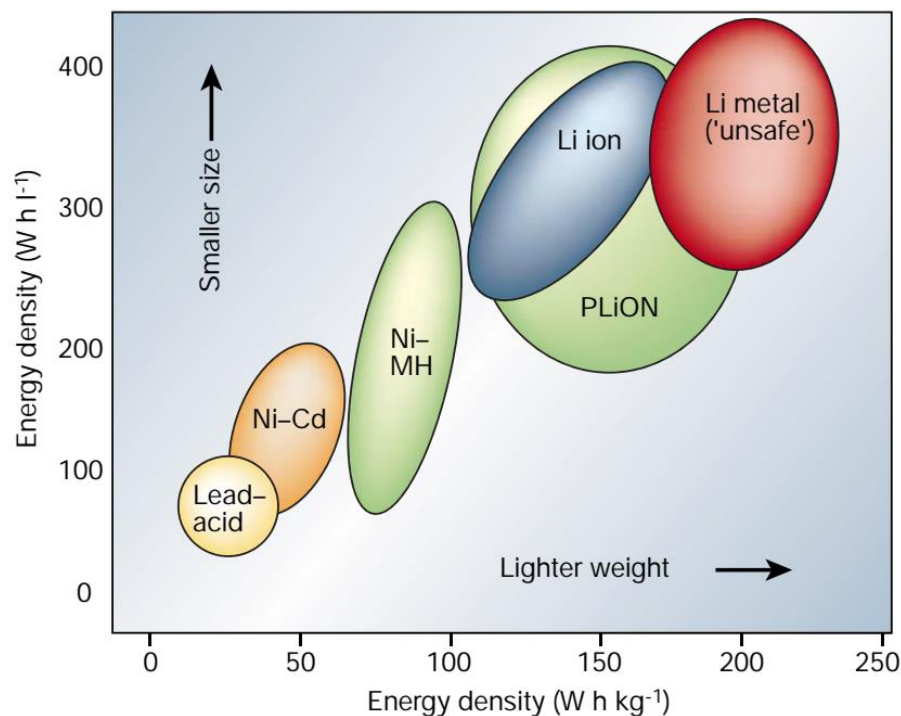
Figure 2-1 Comparison of different battery technologies in terms of their volumetric and gravimetric densities. [2] Reprinted by permission from Springer Nature.

In 1972, TiS_2 was used as a cathode material by M. S. Whittingham against lithium metal [4]. This new technology proved to be very promising and opened up the possibility of developing a rechargeable lithium battery. However, these devices could be unsafe due to the uneven deposition of lithium ions on the lithium surface as dendrites while charging the battery. These dendrites could penetrate the membrane and short-circuit the battery, causing excessive heating of the electrolyte and even explosion (**Figure 2-2**). Therefore, the safety has always been one of the major challenges of commercial rechargeable lithium batteries. Several approaches were attempted to eliminate this problem. The first attempt to solve this problem was the substitution

of lithium metal with a lithium-aluminum alloy, but this brought the issue of low cyclability due to the severe volume change occurring during lithium insertion and extraction [5]. Another solution was to replace the lithium metal with a layered insertion material which can store the lithium in its ionic state rather than metallic state which is inherently safer. This concept was first applied by Murphy et al. (1978) and then by Scrosati (1979) which ultimately led to rocking chair technology at the end of the 1980s and early 1990s [2, 6, 7]. However, insertion of Li^+ into the anode material (rutile structured materials and $Li_x WO_2$) reduced the overall battery potential due to the increase of the negative electrode potential. In order to compensate for this loss, high potential insertion positive electrode materials were needed and so the emphasis focus shifted from layered-type transition type metal sulfides to layered or three-dimensional transitional metal oxides [8]. Goodenough discovered that $Li_x CO_2$ (1977) and spinel manganese (1983) can reversibly store lithium [9]. In spite of these developments in cathode materials, it took about 10 years to commercialize the lithium battery due to the lack of a proper negative electrode and electrolyte in terms of performance and/or cost. Although previous attempts had been made to use graphite as the anode material, the decomposition of electrolyte during the operation was a major obstacle to developing a rechargeable battery [10, 11]. Other attempts to address this problem included Yazami's solid state electrolyte [12]. Sonny Corp. commercialized the lithium-ion battery in 1991 using the earlier metal oxide technologies [2] ($LiCoO_2$ and carbon). The operational voltage was 3.7 V which was three times larger than that of alkaline metal batteries and the gravimetric energy density was ~ 120-150 Wh kg^{-1} which was 2 to 3 times that of Ni-Cd batteries.
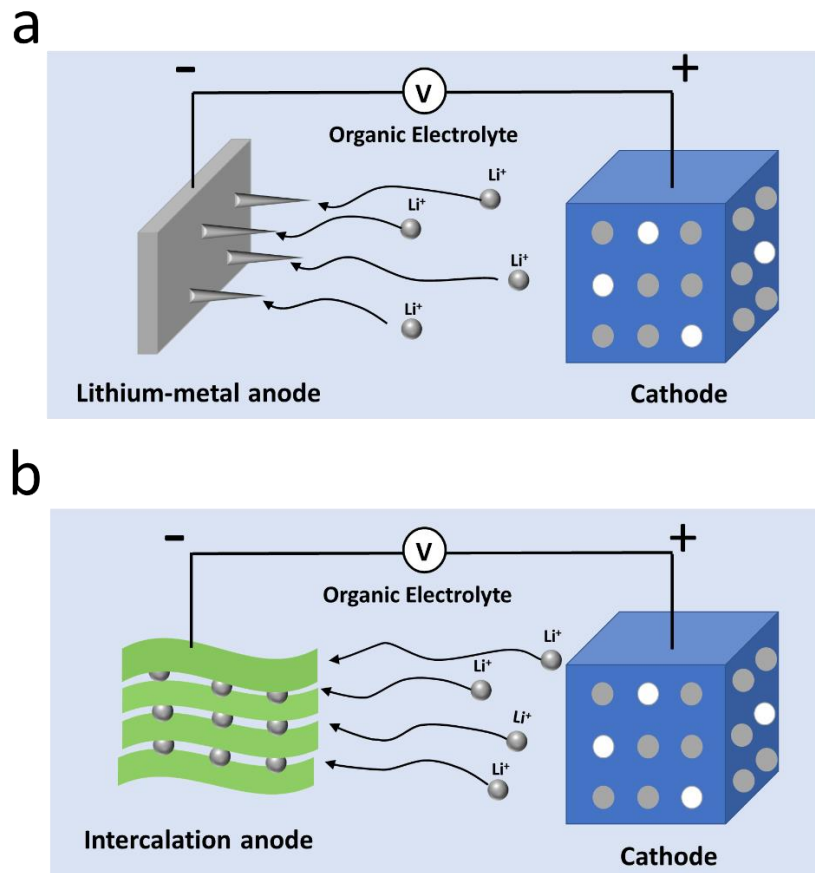
Figure 2-2 Schematic representation of (a) a rechargeable Li metal battery with a dendrite growth at the Li surface and (b) a rechargeable Li-ion battery with no dendrite growth.

2.3.2 Principles of Lithium-ion Batteries

The unit cell of a lithium-ion battery contains an anode, a cathode, an electrolyte, a separator and current collectors (Al, Cu). A typical lithium-ion battery is based on $LiCoO_2$ as cathode, carbon as anode, $LiPF_6$ solution (dissolved in alkyl carbonate solvent) as electrolyte and polypropylene as a separator. Lithium ions (Li^+) shuttle between carbon and $LiCoO_2$ during battery operation (**Figure 2-3**). While charging the lithium ions are extracted from $LiCoO_2$ and

inserted within the carbon layers. During discharging they leave the carbon and intercalate within the Li_xCoO_2 structure. The half-cell and overall reactions are as follows:

$$2\ LiCoO_2 \leftrightarrow Li^+ + e^- + 2\ Li_{0.5}CoO_2\ \text{(Cathode)}$$

$$Li^+ + e^- + C_6 \leftrightarrow LiC_6\ \text{(Anode)}$$

$$C_6 + 2\ LiCoO_2 \leftrightarrow LiC_6 + 2\ Li_{0.5}CoO_2\ \text{(Overall)}$$
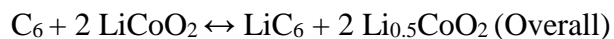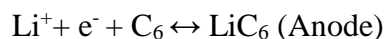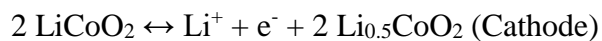
In addition to these reactions, the electrolyte also decomposes at the surface of the anode and cathode due to its electrochemical instability within the operating voltage range. This parasitic reaction occurs at the beginning of the cycling and forms a solid electrolyte interphase (SEI), which is permeable to lithium cations but impermeable to the electrolyte components and electrons. Although the SEI formation does not contribute to the energy generation, it is essential for the durability of rechargeable lithium-ion rechargeable batteries because it prevents further decomposition of the electrolyte and other parasitic reactions.
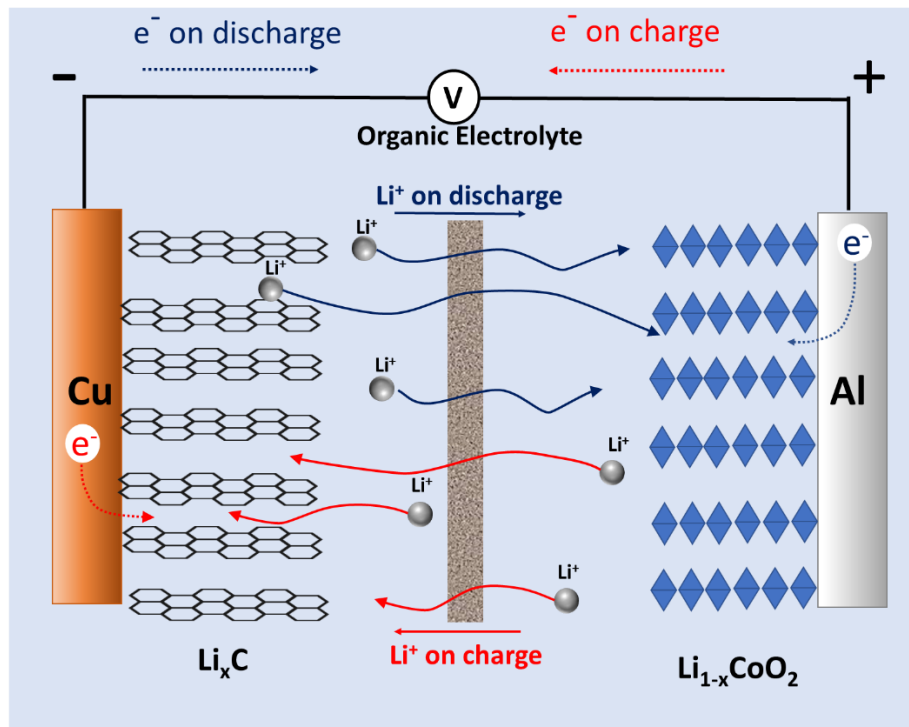
Figure 2-3 Schematic representation of the operating mechanism for a lithium-ion battery.

2.3.3 Cathode Materials

A cathode material is required to have a higher potential with respect to lithium to be utilized in a lithium-ion battery. The electronic conductivity, facile lithium diffusion and structural stability are some other common properties to be an ideal candidate. 3d transition metals such as Mn, Fe, Co and Ni have been intensively studied as cathode materials for lithium batteries. Since chalcogens, especially oxygen, give more structural stability than halogens, the transition metal oxides are common cathode materials [13]. They can be classified based on their structure as follows:

2.3.3.1 Transition Metal Oxides

2.3.3.1.1 Layered Structure

The general formula of this class is $LiMO_2$ where M is Co, Ni, Mn, and etc. $LiCoO_2$ is the most common layered structure cathode material. The atoms are arranged in cubic closed packing, in which lithium and cobalt ions occupy octahedral sites in alternating layers. It has a theoretical capacity of 272 mAh g^{-1} although the practical capacity is only 145 mAh g^{-1}. This stems from the fact that the crystalline structure of $LiCoO_2$ collapses upon complete lithium extraction. Therefore, only 0.5 mole of lithium per mole of $LiCoO_2$ should be extracted to maintain the structure integrity of the material [13]. The environmental and economical concerns arising from the toxicity and high price of cobalt and safety concerns associated with overcharge are challenging for this material.

2.3.3.1.2 Spinel Structure

$LiMn_2O_4$ is a typical spinel cathode material. The oxygen atoms are arranged in a cubic closed packing structure, in which lithium and manganese atoms are distributed to the available tetrahedral and octahedral sites, respectively. The theoretical capacity is 148 mAh g^{-1}. In this case, the practical capacity is limited to ~ 120 mAh g^{-1} due to a discharge cutoff voltage (3.0 V) to avoid distortion of the spinel structure. Capacity fade occurs upon prolonged cycling at 4.0 V attributed to the dissolution of manganese ions and subsequent strain generation on the

crystal [13]. Doping of other transition metals such as Ni, Fe, Ti, Cu and Zn has been studied to improve the cycle stability [14-16].

2.3.3.1.3 Olivine Structure

$LiFePO_4$ is the most common cathode material possessing an olivine structure. In this structure, Li and Fe ions are surrounded by six oxide ions in an octahedral structure and the phosphate group, PO_4, has tetrahedral structure. The $LiFePO_4$ has a capacity of 170 mAh g^{-1}, which is higher than $LiCoO_2$ [13]. Beside the capacity, it has also excellent cycle stability along with low-cost, non-toxic and environmentally friendly nature, which makes it a promising cathode material. However, the strong binding of oxygen to Fe and P leads to a low electrical conductivity and ion diffusivity at room temperature [13]. The carbon coating and reducing the particle size is used to improve the electrochemical properties [17, 18].

2.3.4 Anode Materials

Since lithium metal has a low potential and high gravimetric and volumetric capacity (3860 mAh g^{-1} and 2062 mAh cm^{-3}, respectively), it was used as the anode in rechargeable lithium batteries in the early stage of the development. However, safety issues associated with dendrite formation shifted the focus of research to find alternative safe anode materials [19, 20].

2.3.4.1 Graphite Anode

Today, graphite is the most common anode material in commercial lithium-ion batteries (**Figure 2-4**). Lithium ions can be stabilized within the stacks of the sheets by intercalation

mechanism at low operating voltages (~ 0.1 V vs. Li/Li$^+$). However, the theoretical capacity of graphite is 372 mAh g^{-1}, which is not enough to meet future energy requirements. Therefore, great effort has been made to find new anode materials that can fit the requirements [20].
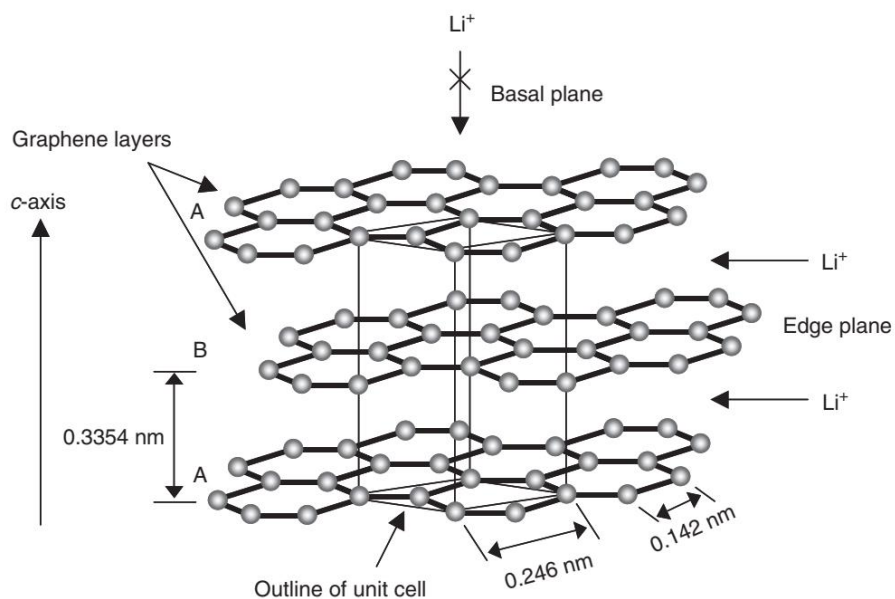
Figure 2-4 Crystal structure of graphite showing the stacking of graphene sheets and the unit of cell[19]. Reprinted by permission from Elsevier.

2.3.4.2 Silicon Anode: opportunities and challenges

In the early 1970s, it was discovered that that lithium metal can combine with other metallic and semi-metallic elements to form a family of intermetallic compounds [21]. The high capacity of silicon (4200 mAh g^{-1}) along with its low-cost, abundance and environmentally benign nature attracted attention as an anode material (**Figure 2-5**). The enormous capacity difference between graphite and silicon stems from the fact that 6 carbon atoms can accommodate only 1 lithium ion (intercalation mechanism) in the charged state; on the other hand, 1 silicon atom

can coordinate with 4.4 lithium ions (alloying mechanism). However, the commercialization of silicon as an anode material suffers from the same problems as other alloy-type anodes due to two major obstacles.
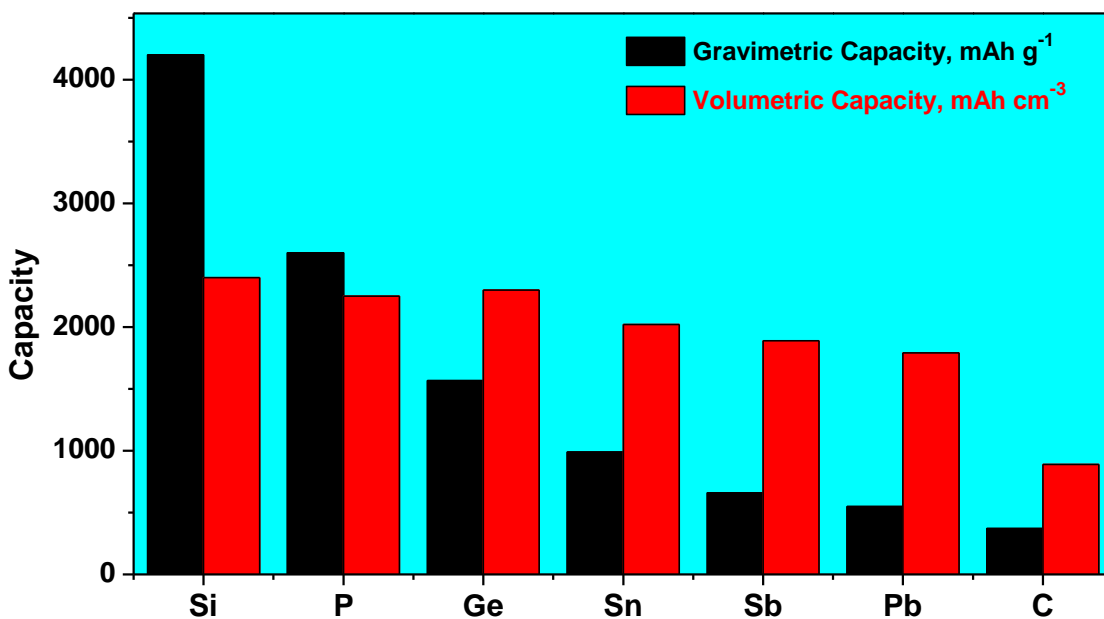
Figure 2-5 Comparison of the gravimetric and volumetric capacities of different alloying reactions vs carbon (C)[22].

2.3.4.3 Obstacle 1: Pulverization and Loss of Active Material

The enormous volume change (~300 %) upon lithium insertion/extraction induces a stress and eventually fractures the silicon particles, disconnects them from each other and peels them from current collector (**Figure 2-6**). This results in a loss of electronic contact between the silicon particles and electrode framework leading to a dramatic loss of capacity. After observing that fracture can be avoided by reducing the silicon size to nano-scale in at least one

dimension, tremendous effort has been focused on using nanostructured silicon as the anode material [23-29]. However, fabrication of silicon nanostructures often requires expensive and complex synthesis methods such as chemical vapor deposition from silane gas precursors or template growth. Thus, processing complexity associated with producing nanostructured silicon materials makes it difficult to scale up. 3D silicon nanoparticles (SiNPs), on the other hand, are closer to the scale up due to their commercial availability and compatibility with conventional slurry coating manufacturing process for battery electrodes. However, the conventional binder (polyvinylidene fluoride, PVDF) does not connect the 3D SiNPs well due to the severe volume change leading to higher interfacial resistance and loss of active material. To address this challenge, different binders such as polyacrylonitrile (PAN)[30], sodium carboxymethyl cellulose (CMC)[31], sodium alginate[32], polyacrylic acid (PAA)[33] have been studied.
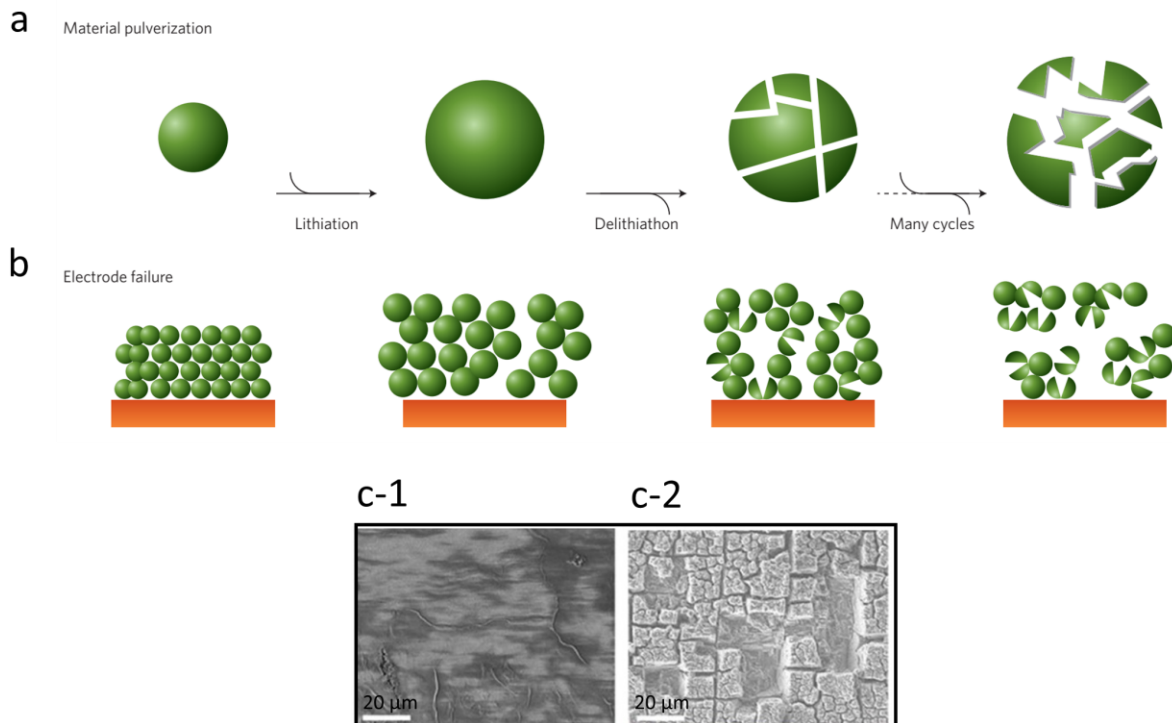
Figure 2-6 Schematics of the failure mechanism of silicon electrode: (a) material pulverization[29], (b) morphology and volume change of silicon electrode[29], reproduced with permission from Springer nature, (c-1) scanning electron microscopy (SEM) of silicon wafer (500 µm thickness) after 3 cycles[34], (c-2) scanning electron microscopy (SEM) image of silicon wafer (500 µm thickness) after 50 cycles[34], reproduced with permission, open access under a Creative Commons Attribution 4.0 International License.

2.3.4.4 Obstacle 2: Instability of Solid Electrolyte Interphase

Despite the success of preventing particle fracture by using SiNPs and keeping all the active materials well-connected by using advanced binders, the cycling performance is still limited. This stems from the unstable solid-electrolyte interphase (SEI). Basically, the SiNPs are

directly in contact with electrolyte and at low electrochemical potentials reductive decomposition of the electrolyte takes place on the surface of SiNPs and forms a passivative solid layer. This solid layer or SEI prevents the further contact of electrolyte with SiNPs. However, unlike the SEI formed on graphite anodes, the SEI layer on SiNPs is not mechanically stable during battery cycling due to the volume change of SiNPs. For each cycle, the SEI is ruptured during lithium insertion causing fresh silicon surface to be exposed to the electrolyte again. Thus, with each cycle more electrolyte breaks down, causes continual growth of the SEI layer leading to poor coulombic efficiency (CE, calculated by the percentage of stored charged which can be extracted) excessive decomposition of the electrolyte, low ionic conductivity, high electronic resistance and eventually dry-out of the cell[35].

To address this problem, encapsulation of silicon particles with carbon and metals has been extensively studied. These coatings were also prone to fracturing without creating a pre-defined void space between silicon particles and carbon coating. Void spaces could act as buffer regions helping to counteract the challenge of volume expansion (**Figure 2-7**)[36-38]. Although these engineered silicon structures with pre-defined void spaces have demonstrated excellent electrochemical performance, their scale up is still an issue. Because the preparation of conformal coatings with void (buffer) regions requires expensive, complex and/or environmentally-unfriendly synthesis methods such as chemical vapor deposition and hydrogen fluoride etching.
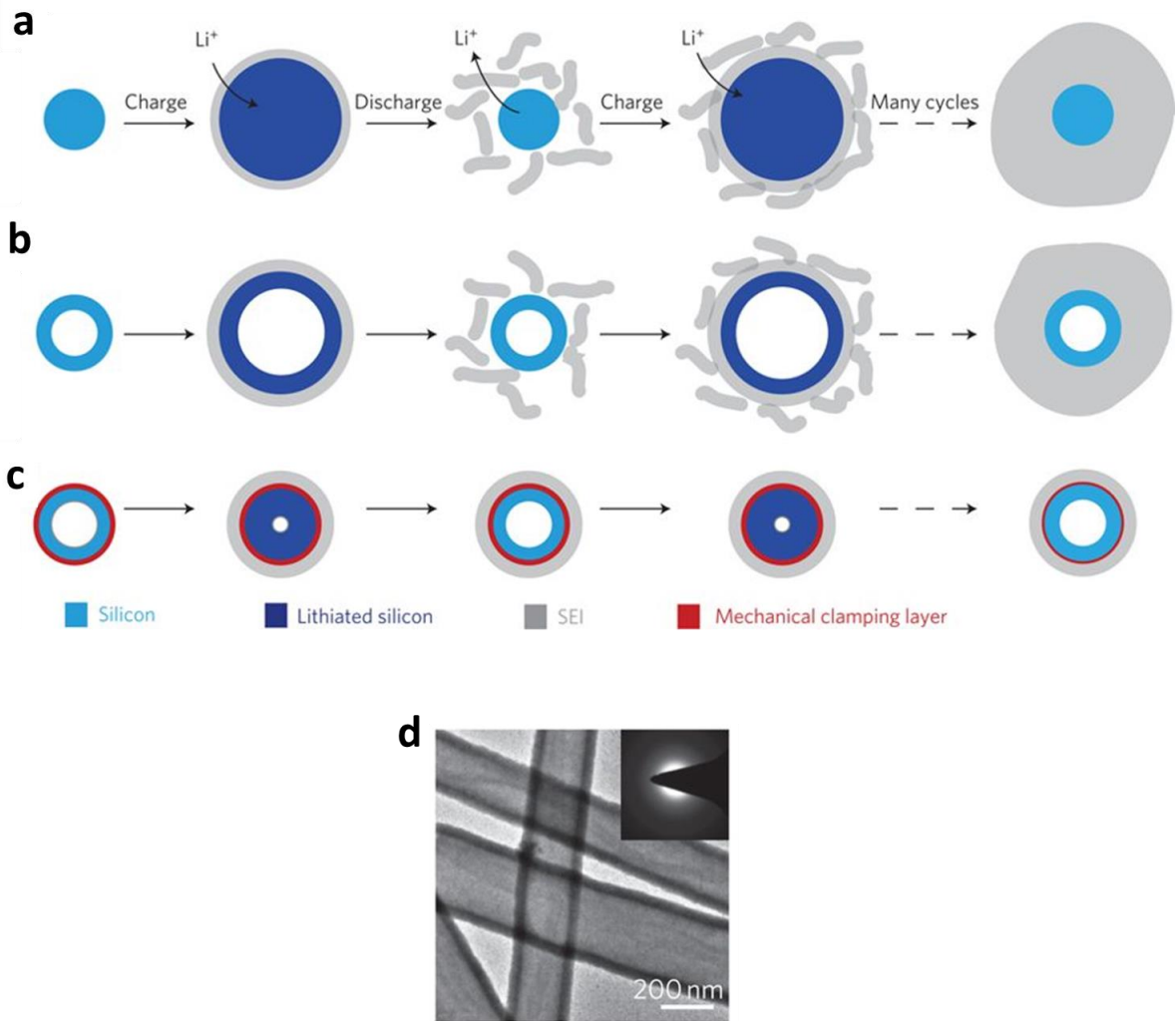
Figure 2-7 (a) Schematic of an unstable SEI layer formation and continual growth on silicon nanoparticles, (b) schematic of an unstable SEI layer formation built on silicon nanowires with pre-defined interior void space, (c) schematic of a stable SEI layer formation built on silicon nanowires with pre-defined interior void space and mechanical clamp layer, (d) TEM image of silicon nanotubes with pre-defined void spaces[38], reproduced with permission from Springer Nature.

2.3.4.5 Revisiting of Micron-Sized Silicon

Despite the excellent performance of anodes prepared with nano-sized silicon structures, the intrinsic problems of nanostructure introduce fundamental challenges such as cost, low tap density and lower columbic efficiency associated with high surface area and complex synthesis. Hence, it is more practical to utilize silicon microparticles (SiMPs) as anode material due to their abundance and low cost. In earlier studies, the durability of SiMPs suffered significantly from particle fracturing and detachment from the electrode surface upon deep discharging[39-41], leading to poor cycle life including a 20 % capacity loss in just 10 cycles. The cycling stability limitation of SiMPs electrodes was circumvented by applying a cut-off voltage. This helped to maintain a two-phase (crystalline-amorphous) silicon microstructure in which only the amorphous phase is active.[40] However, controlling the discharge potential reduces the energy density of the electrode since the crystalline core of the particle remains inactive.[40] To address this problem, SiMPs were engineered by chemical etching with hydrofluoric acid to create internal nanopores (void spaces) to buffer the volume change occurring with deep galvanostatic cycling [42-44], whereas exterior void spaces were created by encapsulating the SiMPs with various carbon frameworks [45] (**Figure 2-8**). Despite promising achievements in cycling performance, the scalability of these electrode manufacturing processes is limited due to the hazardous nature of the etching techniques.

Recently, an advanced binder with high elasticity was engineered from a traditional binder (PAA) by integrating with 5 wt% of polyrotaxanes[46]. The sliding-rings of polyrotaxanes are covalently bonded to the PAA but move freely along the thread component, thus acting like

pulleys to substantially reduce the tension exerted on the binder network. When silicon particles are mixed with this binder and conductive agent without any further physical and chemical treatment, the cycle life has shown impressive improvement. This proves that the binder still plays a very important role in the success of SiMPs as anode material.
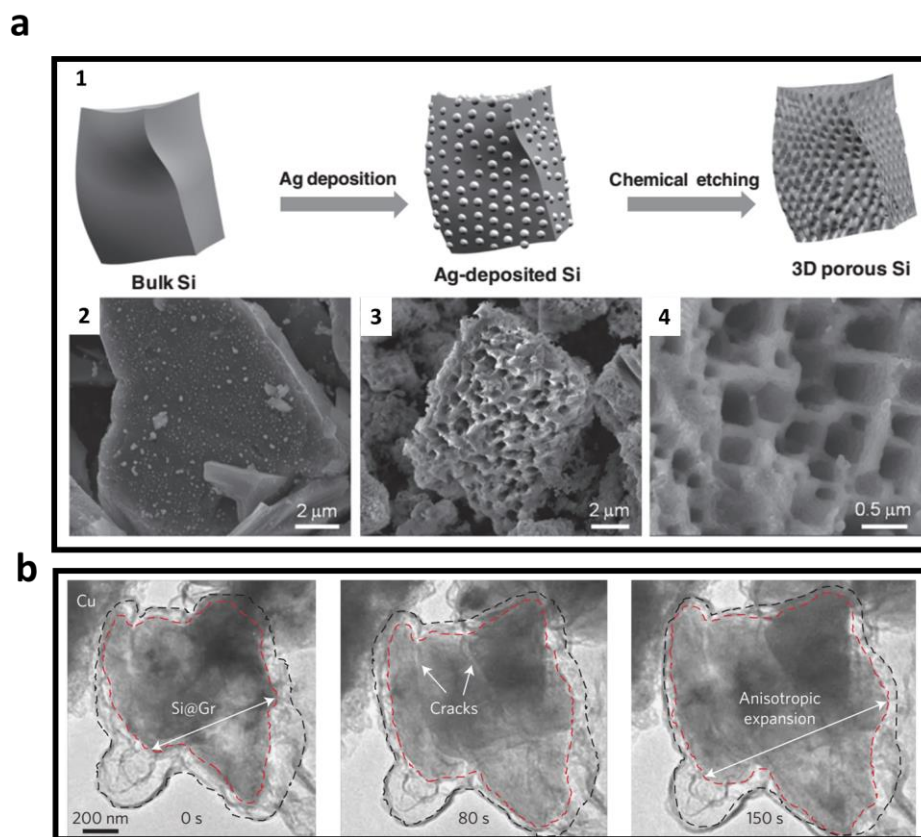
Figure 2-8 (a-1) Schematic of 3D porous SiMP preparation with HF etching, (a-2) SEM image of SiMP after Ag deposition, (a-3) SEM image of SiMP after etching with HF, (a-4) magnified SEM image of SiMP after etching with HF [44], reproduced with permission from John Wiley and Sons, (b) TEM images of a SiMP caged with graphene, (b-1) before lithium insertion, (b-

2) 80 seconds after lithium insertion, (b-3) 150 seconds after lithium insertion[45], reproduced with permission from Springer Nature.

2.3.5 Electrolytes for Lithium-ion Batteries

Lithium ions can shuttle between anode and cathode within the electrolyte. Since non-aqueous electrolytes are stable at high voltages up to 4.5 V, they are commonly used in lithium-ion batteries. The electrolyte is usually prepared by dissolving an inorganic salt in an organic solvent. Lithium hexafluoro phosphate ($LiPF_6$), lithium tetra fluoroborate ($LiBF_4$) and lithium perchlorate ($LiClO_4$) are the most common salts used in lithium-ion batteries. The solvent is usually a mixture of linear or cyclic esters due to the their ability to form stable SEI[47].

Chapter 3 Experimental Section

3.1 Characterization Techniques

3.1.1 X-Ray Diffraction

X-ray diffraction is a non-destructive technique used to determine the composition and crystalline structure of a sample. Since the wavelength of X-rays (1 to 100 angstroms) is in the same order of magnitude as the spacing between the atomic planes, they can be used to obtain crystalline diffraction patterns. During the operation of the instrument, a monochromatic X-ray source is swept over a range of angles to bombard the sample and the diffracted X-rays are collected by a detector rotating about the sample to measure the intensity at different angles. The angle of diffraction is determined by Bragg's law as shown in the equation below,

$$2d \sin\theta = n\lambda$$

where d, θ, n and λ represent the spacing between diffracting planes, incident angle, order of the spectrum (any integer) and wavelength of the X-rays, respectively (**Figure 3-1**). The obtained diffraction patterns are compared with the database having the theoretical diffraction patterns to identify the elements in the sample. It is important to note that amorphous materials cannot be investigated by XRD due to the lack of ordered crystal planes in their structures. In this project, SEM is used to investigate the graphenization of PAN upon annealing.
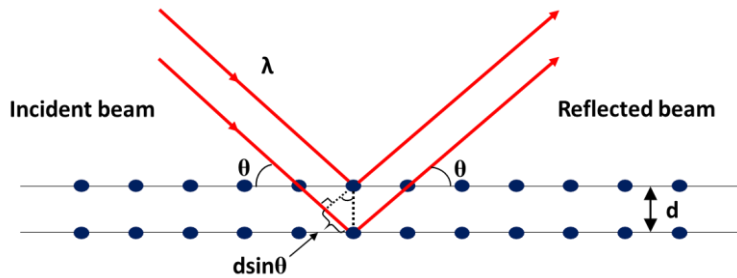
Figure 3-1 Illustration of Bragg's law.

3.1.2 Scanning Electron Microscopy

Scanning electron microscopy (SEM) is a powerful characterization technique to investigate the morphology of samples in micro and nanoscale. The basic difference of SEM from optical microscope is the source to create the magnified image. Unlike an optical microscope which uses the visible light to interact with the sample, SEM utilizes an electron beam to obtain high resolution images of nanostructured samples. The electron beam is accelerated in a chamber and subsequently focused on the sample by a set of electromagnetic lenses to scan an area in a raster fashion. After the beam hits the sample, the secondary electrons scattered from the surface of the sample are detected and converted into an electric signal to produce the final image. The spatial image resolution can reach as high as 0.5 nm [48]. In this project, SEM is used to investigate the morphology of the electrodes.

3.1.3 Transmission Electron Microscopy

Transmission electron microscopy (TEM) is another technique utilizing an electron beam to produce high resolution images of nanostructured samples. The mechanism of the generation

26

and acceleration of electrons in TEM is similar to that of SEM, although the electrons in TEM should be accelerated more than those of SEM to be able to transmit through the specimen. The transmitted electrons are then converted to an electrical signal to produce the final magnified image. The resolution of TEM can reach as high as 0.2 nm which makes it possible to resolve features on a near-atomic scale, allowing the visualization of crystal orientation [49]. In this project, TEM is used to visualize the medium surrounding the silicon nanoparticles within the electrode.

3.1.4 Energy Dispersive X-RAY Spectroscopy

Energy dispersive x-ray spectroscopy (EDX) is an analytical technique which can identify the elemental composition of a sample. EDX is usually coupled with SEM and TEM by simply adding an extra EDX detector within the instrument. Upon electron bombardment of the sample, x-rays are also emitted from the sample beside the secondary electrons. Since each element has specific binding energies, the energy and intensity of emitted x-rays can be used as a fingerprint for elemental identification and quantification. Moreover, the x-rays emitted from a selected area can be used for elemental mapping of the distribution of localized elements. In this project, it is used to map the sulfur, nitrogen, carbon and silicon atoms within the electrode to investigate the performance of the electrodes.

3.1.5 Raman Spectroscopy

Raman spectroscopy is a vibrational spectroscopy technique relying on inelastic scattering of monochromatic light. When a molecule interacts with light, the molecule is excited from a

ground state to a virtual energy state (**Figure 3-2**). Upon relaxation of the molecule, a photon is emitted and the molecule returns to a different vibrational state. The energy difference between the ground state and this final vibrational state causes a shift in the emitted photon frequency from the excitation wavelength. Stokes shift occurs if the final vibrational state is more energetic than the ground state. If the final vibrational state is less energetic than the ground state, an anti-stokes shift occurs to balance the total energy of the system. Thus, the shift in energy provides the information about the vibrational modes in a sample. In this project, Raman spectroscopy is used to determine the changes that occurred at the electrode after thermal treatment [50].
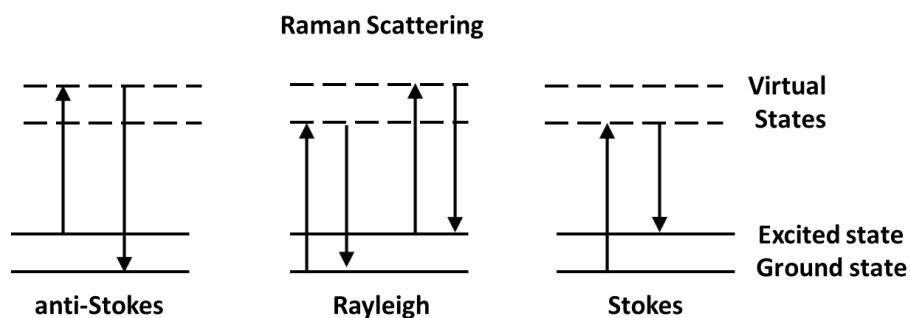
Figure 3-2 Energy level diagram showing the states involved in Raman spectroscopy[50], reproduced with permission from Elsevier.

3.1.6 Fourier-transform Infrared Spectroscopy (FTIR)

Infrared spectroscopy is another vibrational spectroscopic technique relying on the absorption of the photons of infrared wavelength by a molecule. However, rather than using monochromatic light, this technique uses a beam composed of different wavelengths at once and detects the amount of the beam absorbed by the sample. Since the functional groups/bonds

of a sample absorb at different wavelengths, the resulting signal at the detector is a spectrum which can be used as a 'fingerprint' of these functional groups. The usefulness of infrared spectroscopy arises because different chemical structures (molecules) produce different spectral fingerprints. In this study, FTIR is used to obtain information concerning the composition and chain structure of the binder [50].

3.1.7 Thermal Analysis

Thermal gravimetric analysis (TGA) and differential scanning calorimetry (DSC) are two techniques helping to study the physical and chemical properties of a material as a function of temperature. The mass change and thermal flow from a sample are measured by changing the temperature in a linear manner by using TGA and DSC, respectively. The obtained data can be used to determine the thermal degradation temperature of polymers, oxidation of the materials and phase transformations. In this project, these complementary techniques are used to determine the cyclization temperature of polyacrylonitrile (PAN).

3.2 Electrochemical Analyses

3.2.1 Galvanostatic Cycling

Galvanostatic cycling is a powerful method used to investigate the durability of the capacity and reversibility of batteries. In a single cycle, the battery is charged and discharged at a constant current within a predetermined voltage range. Since the time elapsed during the operation is measured by the instrument, it is possible to determine the amount of charge stored

and released by the cell at each cycle. This allows the coulombic efficiency to be monitored during each cycle [20].

3.2.2 Cyclic Voltammetry

Cyclic voltammetry is an electrochemical analysis technique that scans the voltage of an electrochemical cell at a certain rate within a desired potential window. The obtained current-voltage curves are characteristic to the system's redox properties. A low scan rate enables a more detailed analysis of electrochemical reactions [20].

3.2.3 Electrochemical Impedance Spectroscopy (EIS)

Electrochemical impedance spectroscopy is a widely used non-destructive technique to examine and understand the change of impedance of an electrode during a long-term testing. The diagnosis of impedance is done by recording the current response under an applied potential at varying frequencies. Due to the non-linear response of a lithium-ion cell, the impedance is investigated in a perturbative manner where an AC voltage of 1-10mV (with frequency range from 1 mHz to 1MHz) is applied on top of the open-circuit voltage (OCV). The Nyquist plot is the most popular way to present the spectrum by plotting the negative of the imaginary part of impedance versus real part of impedance for varying frequencies. The plot usually consists of one or more semicircles at high frequencies (which are charge-transfer processes) and a tail at low frequencies (which is the diffusion of lithium ions, Warburg impedance) [51, 52].

Chapter 4 High Performance Sulfur-doped Graphene and Silicon Nanoparticle Composite

This chapter is adapted from an article published in Nature Communications, under a Creative Commons Attribution 4.0 International License. http://creativecommons.org/licenses/by/4.0/

Hassan, F.M., Batmaz, R., Li, J., Wang, X., Xiao, X., Yu, A. and Chen, Z., 2015.

"Evidence of covalent synergy in silicon–sulfur–graphene yielding highly efficient and long-life lithium-ion batteries." Nature communications, 6, p.8597.

4.1 Introduction

The success of high performance portable electronics and hybrid (or electric) vehicles strongly depends on future technological progress of commercially available rechargeable batteries[53]. Lithium-ion batteries (LIB) are considered the most likely energy storage devices to satisfy these demands,[54, 55] although they require significant advances in terms of power density, energy density, cycle life, safety and lower production costs. Current LIB systems utilize graphite anodes, which store chemical energy in the form of Li^+ intercalated within graphite layers. This arrangement, while commercially successful, can only deliver a maximum theoretical capacity of 370 mAh g^{-1}.[56] Incorporation of additional components enables the capacity to be dramatically improved, whereby silicon can provide up to 4,200 mAh g^{-1} in theory. While Si-based composites offer immense promise as new generation anode materials, extreme changes in volume during lithiation and delithiation lead to structural degradation and debilitating performance loss over time that has impede their practical application.[35, 56-66]

31

Significant efforts have been devoted to tackling these problems by engineering Si-based electrodes at the nanoscale.[27, 38, 57, 67, 68] For example, silicon nanoparticles (SiNP) were embedded in a carbon matrix through a multistep process to create nanosized void spaces to accommodate volume changes during lithiation/delithiation.[67] Mesoporous silicon sponges have also been prepared by electrochemical etching of B-doped Si wafers, which were used to minimize the pulverization of silicon. With an additional carbon coating, these materials delivered a capacity of 500 mAh g^{-1} for 1000 cycles (at a rate of 1 A g^{-1} and an areal capacity of ca. 1.5 mAh cm^{-2}).[69] Another promising method involved *in-situ* polymerization of a conducting hydrogel to coat the SiNP, providing porous space for the large volume expansions.[28] In order to further improve the performance at a high active material electrode loading, the same group proposed another novel electrode design concept analogous to pomegranates to stabilize the solid electrolyte interface and provide stable cycling up to 1000 cycles.[69] Thus, the use of nanostructured materials produced different solutions to increase the performance of lithium-ion battery. Nevertheless, new challenges are showing up. The high surface area associated with the very small particle sizes can promote the unnecessary reactions with electrolyte leading to high irreversible capacity loss. Furthermore, the higher resistance between the particles leads to poor conductivity. It has become necessary to design electrode materials that are structured on micro-scale while nano-architecture engineered.

We have introduced the concept of using a flash heat treatment that dramatically improves the interfacial properties in the electrode design.[70, 71] However, the limitation in electrode loading and the high cost of high temperatures have led us to think of a new electrode design.

The present chapter introduces a new electrode design concept that capitalizes on the strong covalent interactions occurring between Si, sulfur, defects and nitrogen. This involves wrapping SiNP with S-doped graphene (SG) and then shielding this composite arrangement with cyclized polyacrylonitrile (PAN). Firstly, we mix SiNP (~60%), SG, graphitic oxide (GO) and PAN in dimethylformamide (DMF) to form homogenous mixture under ultrasonic agitation. Then, we cast the slurry on a Cu current collector followed by drying in a convection oven. Finally, the electrodes are cut and pressed, then subjected to a sluggish heat treatment (SHT) by slowly heating in inert gas to 450 $^{\circ}$C, then holding for 10 minutes, followed by furnace cooling. This provides a robust hierarchical nano-architecture that stabilizes the solid electrolyte interphase and results in a superior reversible capacity of ~ 1033 mAh g^{-1} for 2275 cycles at 2 A g^{-1}. The improved electrode design limits electrolyte access leading to a high coulombic efficiency of 99.9% as well as high areal capacity of 3.4 mAh cm^{-2}.

4.2 Experimental Section

4.2.1 Preparation of Graphene Oxide (GO)

The reaction procedure to prepare GO from natural graphite flakes was adapted from the James Tour method.[72] A 9:1 mixture of concentrated H_2SO_4/H_3PO_4 (360:40 mL) was poured into a beaker containing 3 g graphite powder. The solution was mixed for 30 min in an ice bath before adding 27 g of $KMnO_4$ and mixing for another 1 hour. The contents were then transferred to a hotplate and stirred at 50 $^{\circ}$C. After the reaction was completed, 600 mL distilled water was added to the solution while it was being stirred in an ice bath. After the addition of water, 30

mL hydrogen peroxide (H_2O_2) was poured into the solution to reduce the unreacted $KMnO_4$. The final solution was washed several times with 5 % HCl solution and distilled water by centrifugation.

4.2.2 Preparation of Sulfur-Doped Graphene (SG)

100 mg of GO was mixed with 100 mg of phenyl disulfide by grinding. The materials were loaded into a tube furnace and kept outside the heating zone until the furnace temperature reached 1,000 $^{\circ}$C. The sample was then moved into the heating zone where it remained for 30 min under argon protection, followed by cooling to room temperature. Graphene was prepared under identical conditions without phenyl disulfide.

4.2.3 Electrode Fabrication and Coin Cell Assembly

Electrodes were fabricated using commercially available (Nanostructured & Amorphous Materials, Inc., Houston, USA) SiNP with a size range of 50–70 nm. A slurry consisting of 60wt% SiNP, 20 wt% PAN, 19 wt% SG and 1 wt% GO was prepared in DMF. The purpose of adding GO was to induce cyclization of PAN by oxidation. The slurry was mixed under alternating magnetic stirring and ultrasonic radiation (1 h each) three times. The slurry was then coated on Cu foil, dried in a convection oven at 80 $^{\circ}$C for 1 h and then in a vacuum oven at 90 $^{\circ}$C overnight. Circular working electrodes of 1 cm^2 were cut with the average mass loading of silicon on the electrodes ranging from 0.8 to 1.5 mg cm^{-2}. The electrodes were then subjected to the SHT process. They were placed in a quartz tube in a horizontal furnace, slowly heated to 450 $^{\circ}$C over 2 h, then hold for 10 min and finally cooled over another 2 h. The

34

treatment was performed under argon gas flow of 100 standard cubic centimeter per minute (SCCM). Coin-type half cells were fabricated in an argon-filled glove box with the working electrode and a Li metal counter electrode. The electrolyte used was 1M $LiPF_6$ in 30 wt% ethylene carbonate, 60 wt% dimethyl carbonate and 10 wt% fluorinated ethylene carbonate. Galvanostatic charge/discharge testing was carried out over a voltage range of 0.05–1.5 V at different current densities for rate capability testing. Cyclic voltammetry was conducted, at a scan rate of 0.05 mV s^{-1} between 1.5 and 0.05 V, using a Princeton Applied Research VersaSTAT MC Potentiostat. One reference coin cell electrode for performance comparison with SG-Si was prepared with the same composition as above, except that SG was not included, was replaced with graphene. Another reference electrode with the composition of 70 wt% SiNP and 30% PAN as binder was fabricated. These electrodes were subjected to SHT treatment.

4.2.4 Material Characterization

The morphologies of the electrode material were imaged using a TEM (JEOL 2010F TEM/STEM field emission microscope) equipped with a large solid angle for high X-ray throughput and a Gatan imaging filter for energy-filtered imaging. TGA and DSC were conducted using TA instrument Q500. The TGA testing was carried out in air over a temperature range of 25–850 $^{\circ}$C and ramp rate of 10 $^{\circ}$C min^{-1}. Raman spectroscopy spectra were obtained using a Bruker Senterra unit, applying a laser beam with a wavelength of 532 nm.

4.2.5 Quantum Mechanics Computational Method

The DFT calculations were carried out using the Amsterdam Density Functional "ADF". [73, 74] The electron wave functions were developed using a basis set of numerical atomic orbitals (NAOs) and Slater-type orbitals (STOs). In addition, the triple polarization (TZP) basis of Slater-type orbitals was utilized. We used PBE−D3 to perform the calculations [75] where the generalized gradient approximation (GGA) for the exchange and correlation energy terms was used. This explicitly takes into account the dispersion correction. This is a widely used function for catalysis applications and can produce reliable energies on graphene systems. [76, 77]

4.3 Results and Discussion

Mixing of SiNP (~60%), SG, PAN, GO and DMF was conducted using ultrasonic irradiation (**Figure 4-1a**). This helped achieve a homogeneous distribution of electrode components and possibly preferential attachment of Si to S and defect sites in the sulfur-doped graphene. Schematic illustration of the SHT of the electrodes, after being coated on copper foils and dried, is shown in **Figure 4-1b-c**. The optical images of the electrode before and after SHT clearly show the color changes from light to dark, consistent with the partial carbonization with PAN during the SHT treatment. In this arrangement, we speculate that SiNP preferentially adsorbs on the sulfur and defect sites in graphene and is coated with PAN. As a result, the electrode materials consist of interconnected microparticles. These microparticles are composed of SG nanosheets that sandwich the SiNP clusters. This entire arrangement is encapsulated with PAN. After SHT, PAN is cyclized, tethering the SiNP and SG nanosheet

composites together, resulting in a robust structure providing both inner porosity and flexibility.
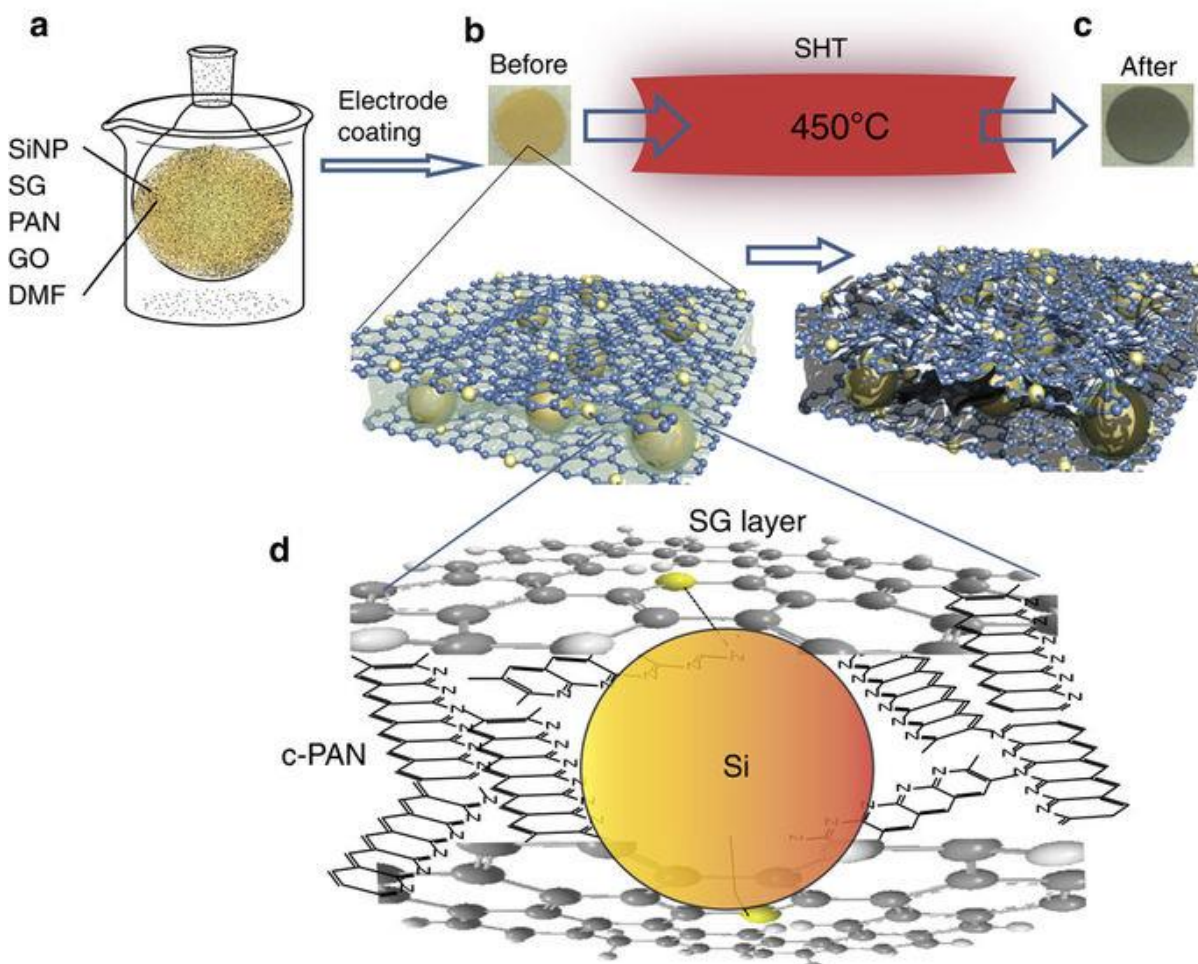
Figure 4-1 (a) Components mixing with ultrasonic irradiation, (b) optical image of the as-fabricated electrode made of SiNP, SG and PAN, (c) optical image of the electrode after SHT and (d) schematic of proposed atomic structure of the electrode.

The high angle annular dark field (HAADF) scanning transmission electron microscope (STEM) image in **Figure 4-2a** shows a micron scale cluster in which the SiNPs are well wrapped by SG and invariably dispersed within the nanosheets matrix. **Figure 4-2b** displays a higher magnification HAADF-STEM image of the SG-Si electrode, while **Figure 4-2c** displays the corresponding electron energy loss spectroscopy (EELS) image (RBG mixed color mapping) of the highlighted area in **Figure 4-2b**. Each pixel in the EELS image corresponds to a 3.4 nm x 3.4 nm area. The yellow color corresponds to Si, while the red color denotes sulfur (mixed red and yellow give orange with different degrees relative to the concentration). It can be inferred that sulfur tends to concentrate along the circumference of the SiNP. The corresponding spectrum of the EELS-based elemental mapping is shown in the **Figure 4-2d.** It again confirms the presence of Si, S, N and C, with S coming from the SG and N from the cyclized PAN (c-PAN). In order to show how the binder PAN is attached to the particles and connects them, a regular TEM image is presented in **Figure 4-2e**. It clearly shows that the particles are interconnected and wrapped with graphene. A closer image of HRTEM focusing on one particle (**Figure 4-2f**) shows the crystalline Si particles with a shell of c-PAN and graphene nanosheets. Raman spectra of a PAN film deposited on copper foil, then dried, before and after SHT are shown in **Figure 4-3a**. While no features appear before SHT, two characteristic peaks at ~1346 cm^{-1} and ~1605 cm^{-1} are observed after SHT. These peaks correspond to the "D" and "G" bands from the structural defects and disorder of sp^3-carbon atoms and the plane vibration of the sp^2-carbon atoms in the two-dimensional lattice of the c-PAN, respectively. This result again confirms that cyclization of PAN is associated with

38

graphitized carbon. The same features appeared with the electrode materials after subjecting them to SHT(**Figure 4-3b)**.
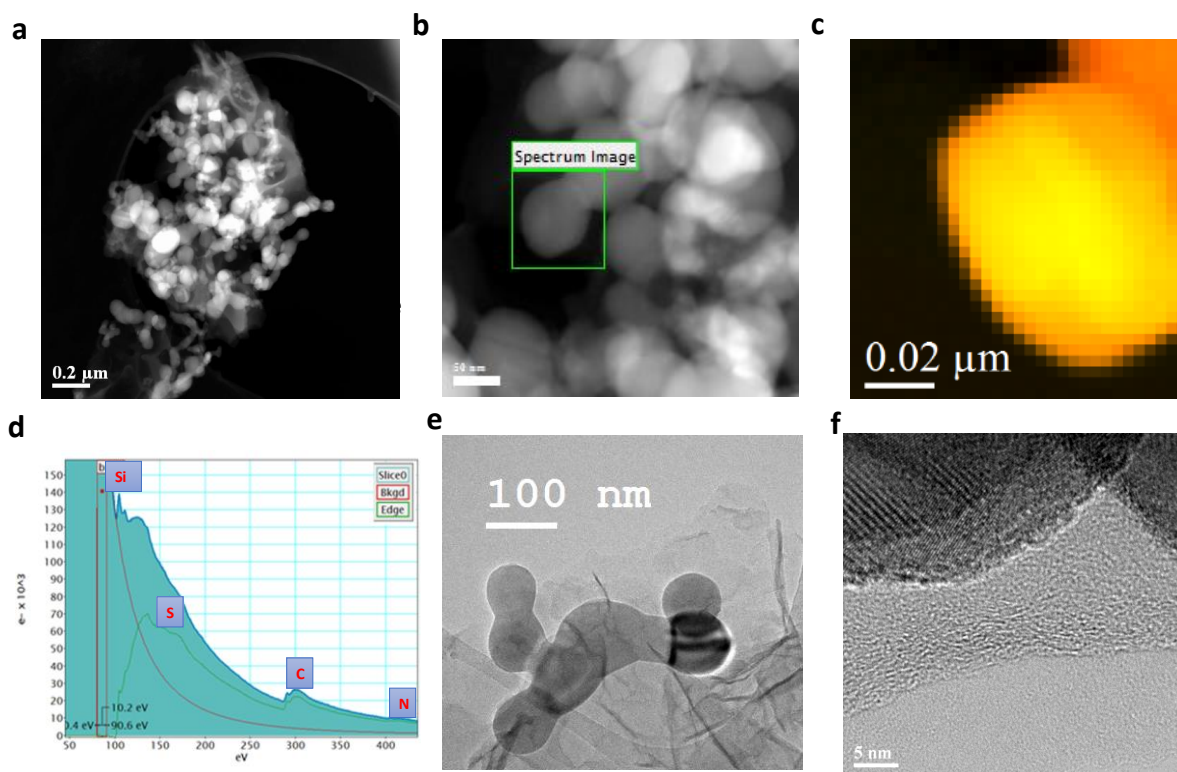
Figure 4-2 (a) HAADF–STEM image of the SG–Si electrode, (b) higher magnification HAADF–STEM image of SG–Si and (c) EELS mapping of the elements Si (yellow) and S (red), with each pixel representing 3.4 × 3.4 nm, (d) electron energy loss spectrum for SG-Si electrode after sluggish heat treatment, (e) regular TEM image zooming in on interconnected SiNPs in the SG–Si electrode, (f) HRTEM image of a SiNP with carbon shell and graphene.

It is well established that sluggish heating can cyclize PAN to a form that can stabilize electrode structures. [78, 79] A small proportion of graphitic oxide (GO), ~ 1%, was added as oxidizing agent to promote cyclization of PAN. The characteristic exothermic peak for PAN cyclization is shown in the differential scanning calorimetry (DSC) scan in **Figure 4-3c**, which is consistent with that in previous reports.[80, 81] Upon treatment, PAN loses about 20% of its mass as shown by TGA (**Figure 4-3d**). The SHT treatment has modified the chemical structure of the PAN causing cyclization. The cyclization process is associated with the enrichment of pyridinic-type nitrogen, as shown by the XPS spectrum in **Figure 4-3e**. The presence of pyridinic nitrogen is reflected by the appearance of a second peak at 398.38 eV.[82, 83] After cyclization, PAN has a π-conjugate structure that is believed to lower the electronic and charge transfer resistances of the electrode, as reflected by the EIS Nyquist plot shown in **Figure 4-4a**. After inspecting the HRTEM images introduced in **Figure 4-2** and EDX mapping in **Figure 4-4b-g,** we propose that almost every SiNP is caged in a carbon shell of c-PAN. It is also clearly observed that no agglomeration of SiNP has occurred.
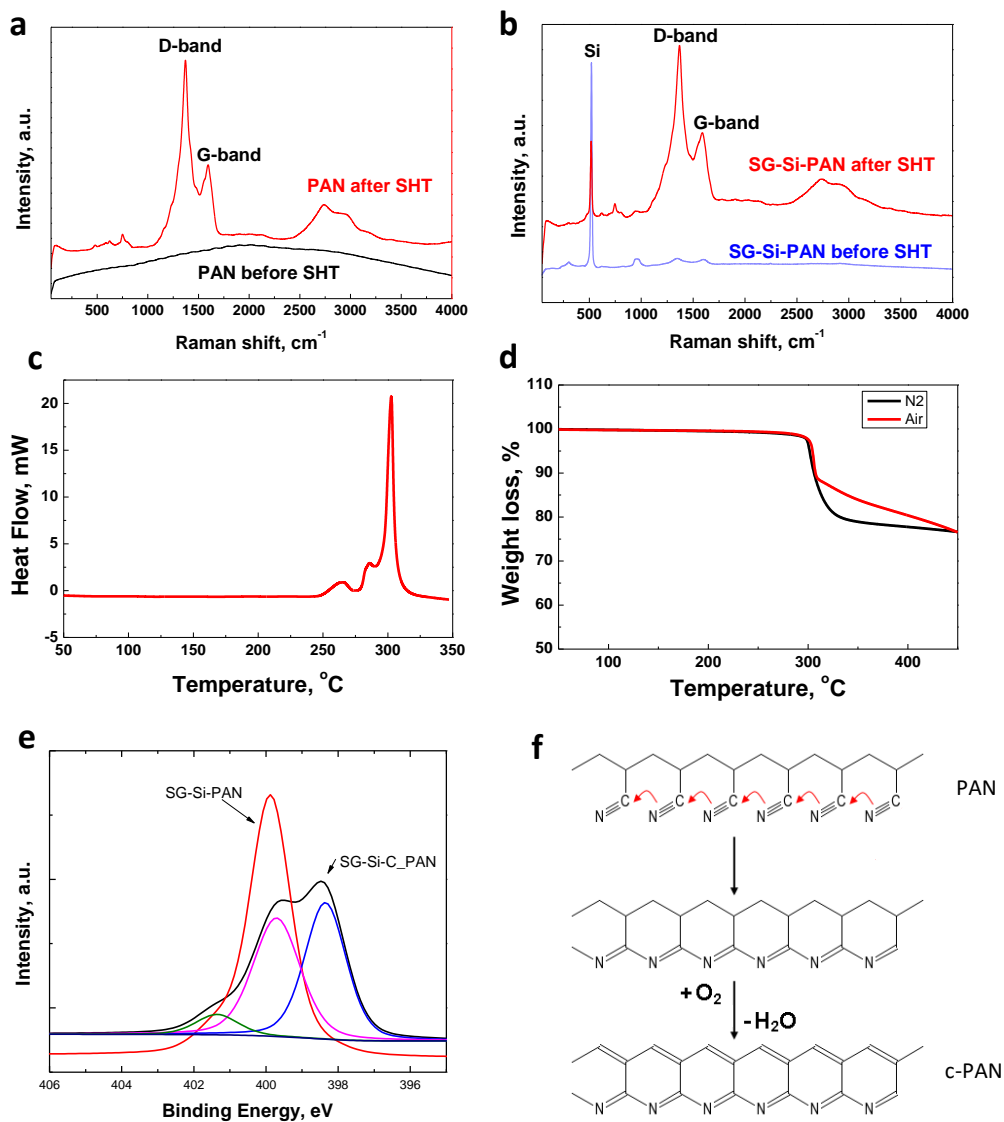
Figure 4-3 (a) Raman spectra for PAN film on copper before and after SHT, (b) Raman spectra for SG–Si-PAN electrode surface before and after SHT, (c) DSC for PAN in nitrogen environment showing a characteristic peak at ~ 300 °C, which corresponds to PAN cyclization as proposed in (f), (d) TGA for PAN in both air and nitrogen environment. During cyclization

PAN loses ~20% of its mass, (e) high resolution XPS of nitrogen in SG-Si-PAN (before SHT), and SG-Si-C_PAN (after SHT), (f) proposed PAN cyclization mechanism.
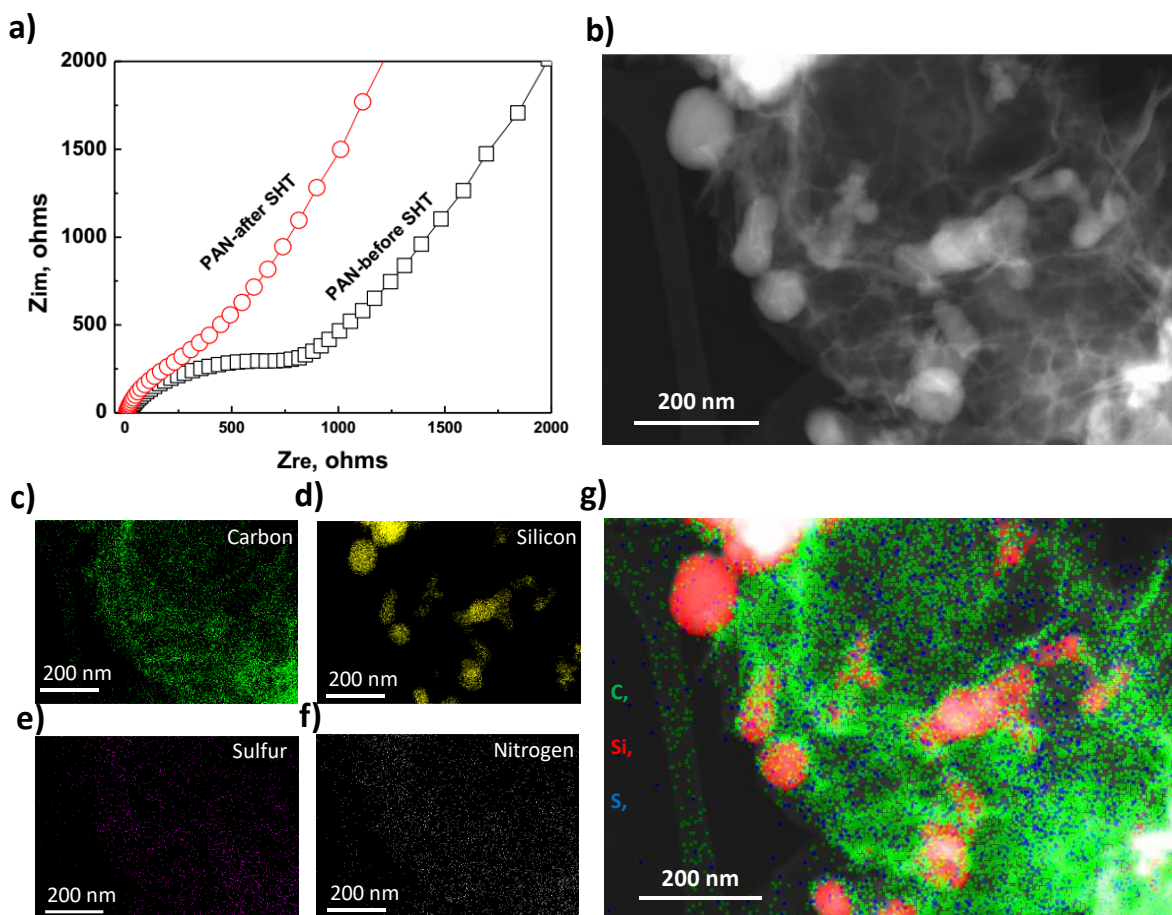
Figure 4-4 (a) EIS Nyquist plot of a coin cell fabricated using PAN-coated copper foil vs lithium before and after SHT, (b) TEM image of SG-Si electrode material, (c-f) the corresponding EDX mapping of the elements carbon, silicon, sulfur and nitrogen, (g) overlaid colour map of carbon (green), silicon (red) and sulfur (blue).

X-ray photoelectron spectroscopy. The elemental analysis of the electrode material after being subjected to SHT is determined by the XPS survey spectrum as shown in **Figure 4-5a**,

confirming the presence of Si (40%), S (5%), C (40%), N (11%) and O (4%), with all compositions given in atomic %. It should be pointed out that XPS is surface sensitive with analysis depth of about 8-10 nm. Therefore, this elemental quantification is different from the expected values estimated to be 60% Si and ~0.5% S.   The C spectra in **Figure 4-5b** shows several peaks: the first one (1) centered at 284 eV corresponding to sp^2 hybridized graphitic-type carbon, (2) centered at 284.8 eV due to the presence of sp^3 bonded carbon, (3) and (4) associated with oxygenated carbon and (5) related to plasmon loss.[84-86] The core-level spectra in **Figure 4-5c** shows the typical elemental Si peak (1) located at 99.4 eV, with minor peaks at higher binding energies (~103.4 eV) related to oxygenated silicon or silicon bonded to sulfur.[87] **Figure 4-5d** shows the core-level spectrum of S in pure SG containing ~ 2.5 atomic % S. The S_{2p} doublet corresponding to the sulfide (C-S-C) form of S is observed at 164.0 and 165.2 eV and labeled (1) and (2). These peak locations are in good agreement with the reported $S_{2p3/2}$ and $S_{2p1/2}$ spin orbit couplet.[88-90]   The other minor peaks labeled as (3) in **Figure 4-5d** and located at higher binding energies are attributed to oxidized forms of sulfur (-SO_x).[91]

The structure elucidation of SG using XPS are used as the base to determine the basic SG cluster used for DFT calculations discussed later. It is important to note that sulfur is distributed homogenously in the graphene sheets, both on the edges and in the basal planes. This is reflected by the STEM-EDX and EELS maps shown in **Figure 4-6**. A set of samples were prepared as described below and analysed in order to investigate the covalent chemisorbed interactions between Si and S in SG. The four samples prepared are: (1) elemental sulfur microparticles, SiNP and PAN dispersed in DMF followed by solvent removal; (2) Sample 1

annealed at 450 °C (same as in SHT process); (3) SG + PAN + SiNP dispersed in DMF followed by solvent removal; and (4) Sample 3 annealed at 450 °C (same as the SHT process). High resolution XPS spectra for these samples are shown in **Figure 4-5e**. Sample 1 shows the regular S2p orbital split (doublet at 163.98 and 165.08 eV). Additionally, a very depressed broad peak is observed at average 168 eV which may be attributed to silicon loss plasmon resonance. [92, 93] Plasmon loss peaks involve a strong probability for loss of a quanta of energy due to electron interaction with the photoelectron.[94] For Sample 2, growth of Si plasmon loss can be attributed to the covalent interactions of silicon with sulfur, while the majority of sulfur is lost after annealing due to sublimation (m.p. ~120°C). The XPS results show a greatly enhanced peak signal for the silicon loss plasmon resonance. SG rather than elemental sulfur is examined in Samples 3 and 4. The XPS signals for both these samples also show a strong peak for silicon loss plasmon resonance, indicating possible interactions between the Si and S atoms even before the annealing process. This feature does not change with annealing, indicating a similarly strong interaction between the two elements in both cases. We speculate that the enhanced plasmon loss in samples 2-4 can be attributed to the interaction of Si with S. Some previous studies have shown possible reaction between silicon and sulfur.[95-98] The morphology investigated by SEM and pore size distribution investigated by BET of the electrode before and after the SHT process are shown in **Figure 4-7**, respectively. The micron-sized particles comprising SiNP dispersed on the sheets of SG and capped with c-PAN are demonstrated. The results of BET analysis also show that the nanoporosity of the electrode structure increased after SHT.
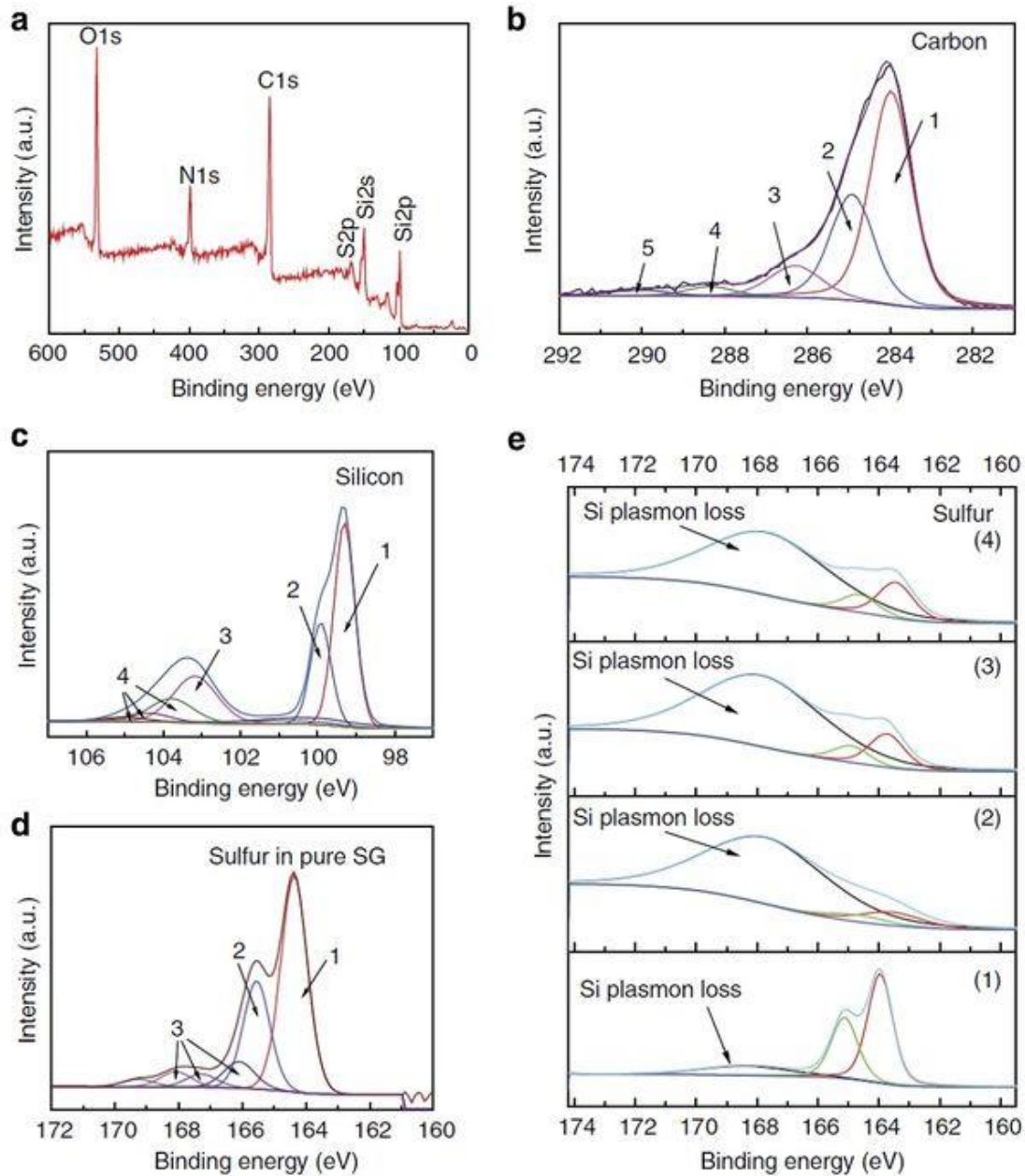
Figure 4-5 (a) XPS survey spectra confirming the elements Si, S, C, N and O, (b) high-resolution XPS spectra of carbon in SG–Si, (c) high-resolution XPS of Si–2p in SG–Si, (d) high-resolution XPS spectra of sulfur in pure SG and (e) high-resolution XPS of sulfur in (1) electrode material made of elemental S, SiNP and PAN, (2) electrode material of (1) after being

subjected to SHT, (3) electrode material made of SG, SiNP and PAN and (4) electrode material of (3) after being subjected to SHT.
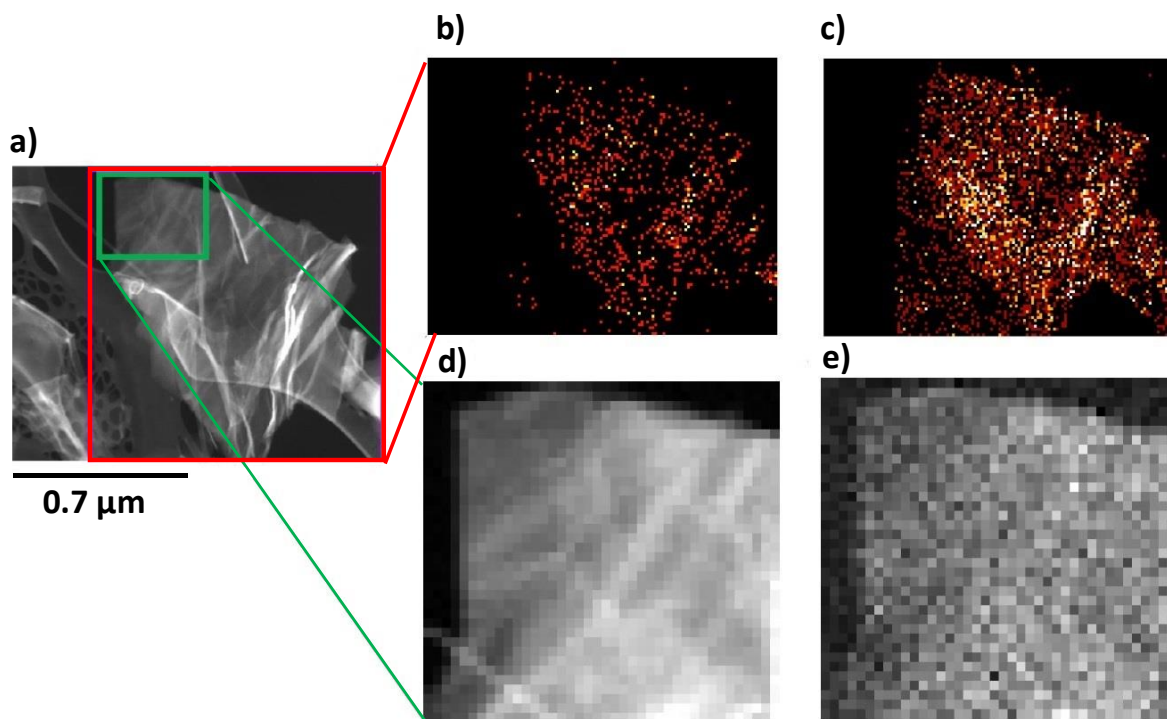
Figure 4-6 (a) STEM-HAADF of a SG nanosheet; (b) and (c) present the EDX maps for sulfur and carbon, respectively, (d) and (e) represent the EELS maps of carbon and sulfur, respectively, in pixilated grey color, each pixel represent 10 x 10 nm.
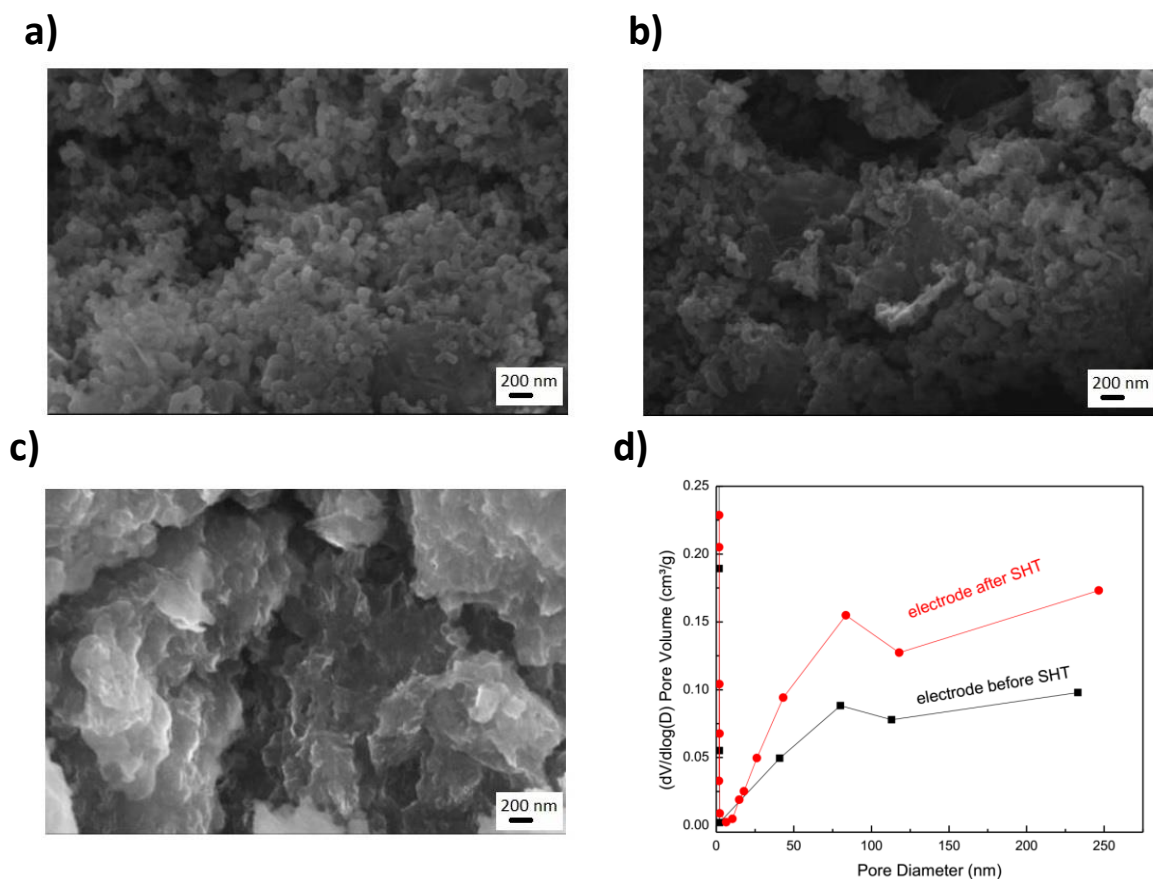
Figure 4-7 (a) The as-prepared electrode after drying, (b) the electrode after sluggish heat treatment, (c) the electrode extracted from a coin cell after 100 cycles, (d) comparison of pore size distribution for the SG-Si electrode before and after SHT.

Figure 4-8a presents typical galvanostatic charge/discharge profiles of the SG-Si based electrode tested at 0.1 A g^{-1} between 1.5 and 0.05 V. The observed plateau in the first discharge curve is caused by the alloying of crystalline silicon with lithium.[24, 67] The SG-Si delivers a discharge capacity of 2865 mAh g^{-1} during the first cycle based on the total mass of SG, c-PAN and Si, with a high coulombic efficiency of 86.2%. If not mentioned otherwise, all reported capacities are based on the total mass of SG, c-PAN and Si. The voltage profiles

47

during the subsequent cycles show slightly different behaviour, which is common for lithiation of amorphous Si formed during the first cycle. It is noteworthy that the areal charge capacity is about 3.35 mAh cm^{-2}, which is close to the performance targets for next generation high energy lithium-ion batteries.[27] **Figure 4-8b** shows the cycling stability of the SG-Si at 0.1 A g^{-1}. A stable performance up to 100 cycles can be obtained, with an average capacity of 2750 mAh g^{-1} (~ 3.35 mAh cm^{-2}). These results compare favourably to a recently published report.[27] The charge storage behavior is also characterized by cyclic voltammetry (CV). **Figure 4-8c** shows the first 5 cycles of the SG-Si electrode in a coin cell at a scan rate of 0.05 mV s^{-1}. During cathodic scan, two distinctive peaks appear at 0.27 and 0.22 V vs Li/Li$^+$, indicating the formation of Li$_{12}$Si$_7$ and Li$_{15}$Si$_4$ phases, respectively.[99, 100] In the anodic direction, the corresponding two peaks are located at 0.31 and 0.49 V, representing the dealloying of Li$_x$Si to Si. All anodic and cathodic peaks become broader and larger as a result of cycling, which is a common feature attributed to the conversion of Si into an amorphous phase during lithiation/delithiation. Similar features are observed for a G-Si electrode investigated for comparison as shown in **Figure 4-9a.** The rate capability curve of the SG-Si electrode in **Figure 4-8d** reveals the excellent kinetics of the SG-Si electrode at different currents up to 4 A g^{-1}. Moreover, the robust structure enables very stable cycling, where a capacity of ca.1033 mAh g^{-1} can be maintained for 2275 cycles at a rate of 2 A g^{-1}. By comparison, a similar electrode structure prepared by replacing SG with non-doped graphene exhibits inferior rate capability and cycling stability, as shown in **Figure 4-8e**. The high capacity of the G-Si persists only for 80 cycles, then fades gradually, reaching ~ 400 mAh g^{-1} after 800 cycles. Such a

capacity fade is mainly attributed to the degradation of the Si structure, where the expansion and shrinkage of SiNP during cycling leads to separation from the graphene scaffold and subsequent loss of conductivity and instability of the solid electrolyte interphase (SEI) structure.

The significantly different electrochemical performances put a spotlight on the important role of sulfur in binding the SiNP to the surface of SG. This has encouraged us to further investigate its role using density functional theory (DFT), as discussed below. As a reference, a coin cell made of a SiNP/PAN electrode fabricated using SiNP and PAN subjected to a SHT also shows poor rate performance. In addition, its cycle stability persists for only 65 cycles and then degrades rapidly to almost zero capacity (**Figure 4-8f).** These results emphasize the important role of the covalent binding between Si and SG to achieve the impressive performance. In all cases, SG-Si, G-Si and even just Si when fabricated using PAN and followed by our SHT treatment persist for at least 2275, 80 and 65 cycles, respectively. On the other hand, a coin cell fabricated using the same SiNP (60%), Super P (20%), and the traditional binder polyvinylidene fluoride (PVDF) (20%) without any SHT treatment degrades very rapidly, (**Figure 4-9b)**. Since we consider the total mass of the electrode during calculation of the capacity, it is important to show the relative contribution of each of the electrode components. **Figure 4-8g** is a pie chart showing the relative % contribution of the capacity observed in **Figure 4-8d**. These contributions are estimated form the battery performance for SG under similar conditions, which shows average reversible capacity of 235 mAh g^{-1}, and an electrode coated with only PAN after SHT treatment, which gave an average capacity of 18 mAh g^{-1}

(**Figure 4-9c-d**). To investigate the specific role of cyclized PAN and SG, reference cells were fabricated from SG-Si-PVDF and GO-Si-PAN, respectively. The battery performance of these two cells decayed rapidly as shown in **Figure 4-9e-h.** This emphasizes the synergy of the SG-Si-c_PAN in enhancing the electrode stability and providing stable cycling.
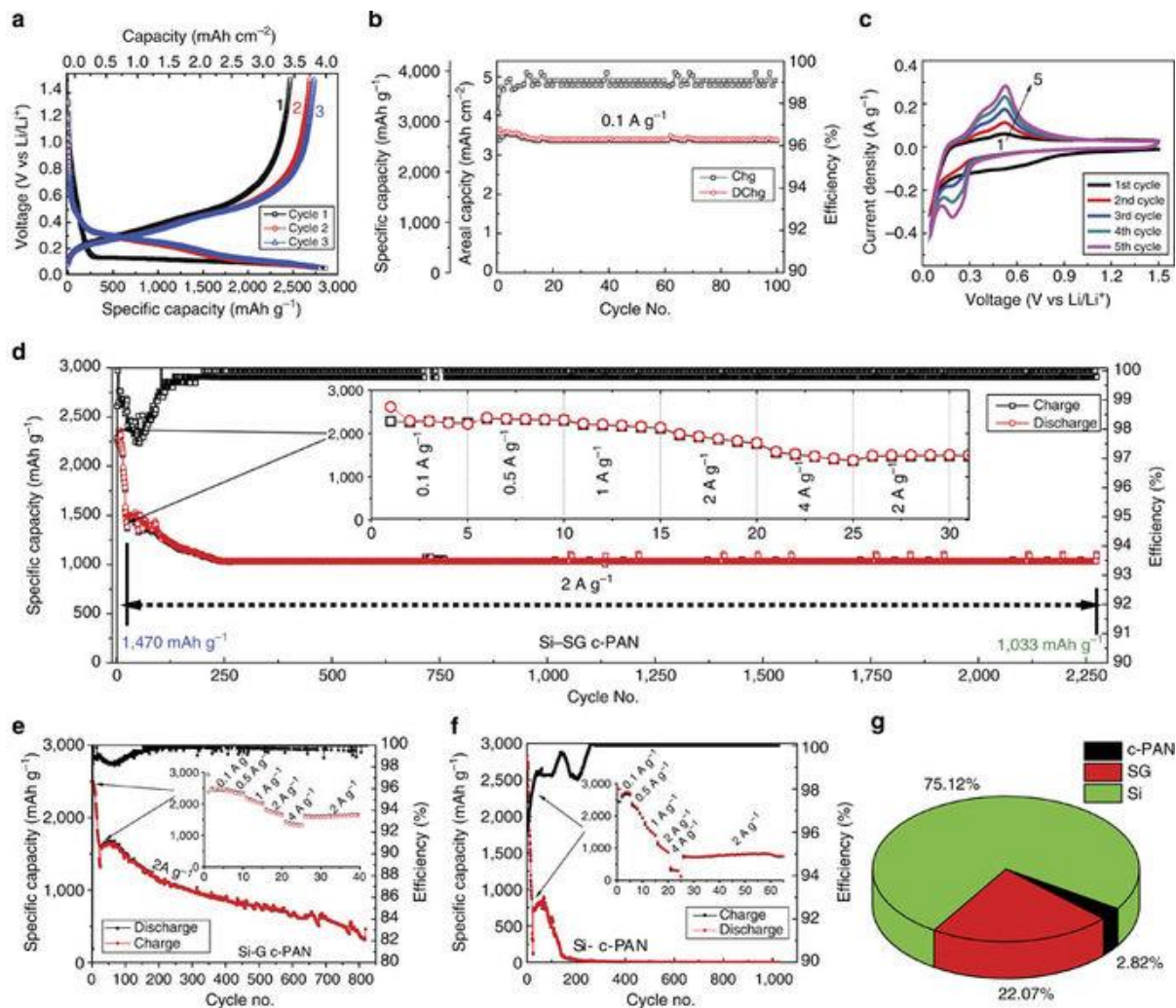
Figure 4-8 (a) Voltage profile of SG–Si anode at 0.1 A g^{-1}, (b) the corresponding cycle stability, (c) cyclic voltammogram curves of the SG–Si coin cell, (d) rate capability of SG–Si anode followed by cycle stability at 2 A g^{-1}, the inset figure is zooming to the first 30 cycles,

(e) rate capability of G–Si anode followed by cycle stability at 2 A g^{-1}, the inset figure is zooming to the first 40 cycles, (f) rate capability of Si–PAN anode followed by cycle stability at 2 A g^{-1}, the inset figure is zooming to the first 60 cycles and (g) a pie chart showing the relative contribution of the electrode materials for the capacity seen in d.
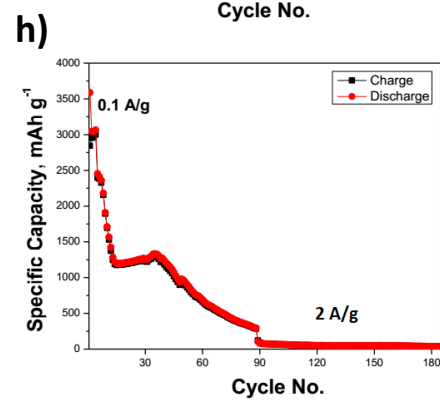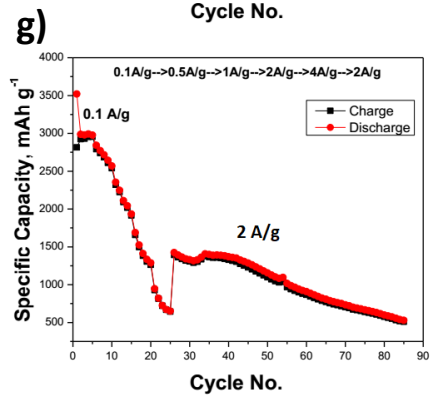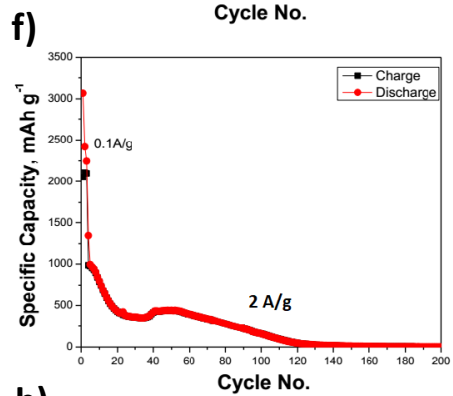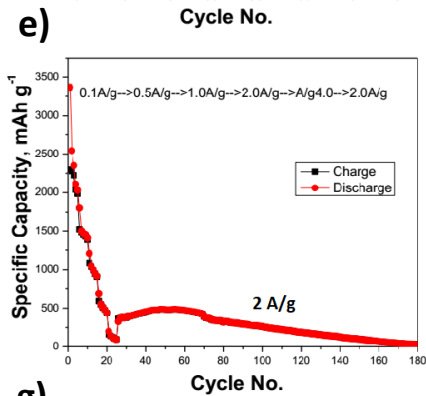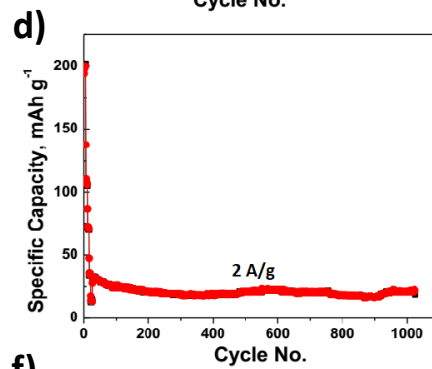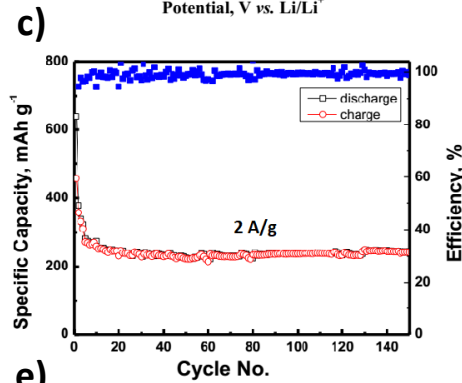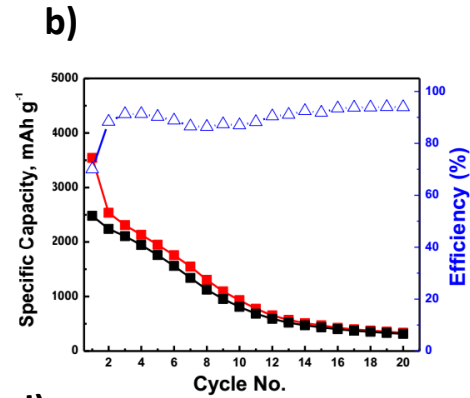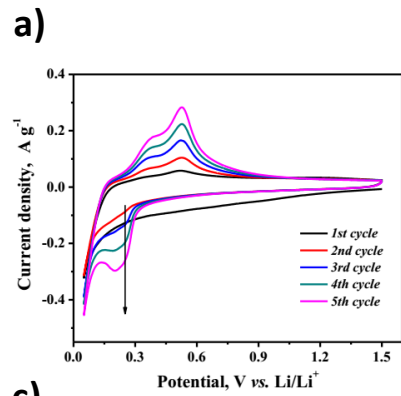
Figure 4-9 (a) Cyclic voltammograms of G-Si coin cell, (b) cycle stability of Si-Super P-PVDF reference cell, (c) cycle stability of SG-PAN reference cell after SHT, (d) cycle stability of c-PAN reference cell after SHT, (e) rate performance and cycle stability of Si-Super P-PVDF reference cell, (f) cycle stability of Si-Super P-PVDF reference cell, (g) rate performance and cycle stability of Si-GO-PAN cell after SHT, (h) cycle stability of Si-GO-PAN cell after SHT.

The volumetric capacity for the cell presented in **Figure 4-8b** was calculated and the result is plotted in **Figure 4-10a**. It reveals that the SG-Si-c_PAN electrode is able to provide a reversible capacity of ~ 2350 mAh cm^{-3} for up to 100 cycles. Coin cells fabricated using a different electrode composition of 40:30:30 (Si-SG-PAN) have also been tested. The results presented in **Figure 4-10b-c** similar trend of stable cycling and improved rate capability.
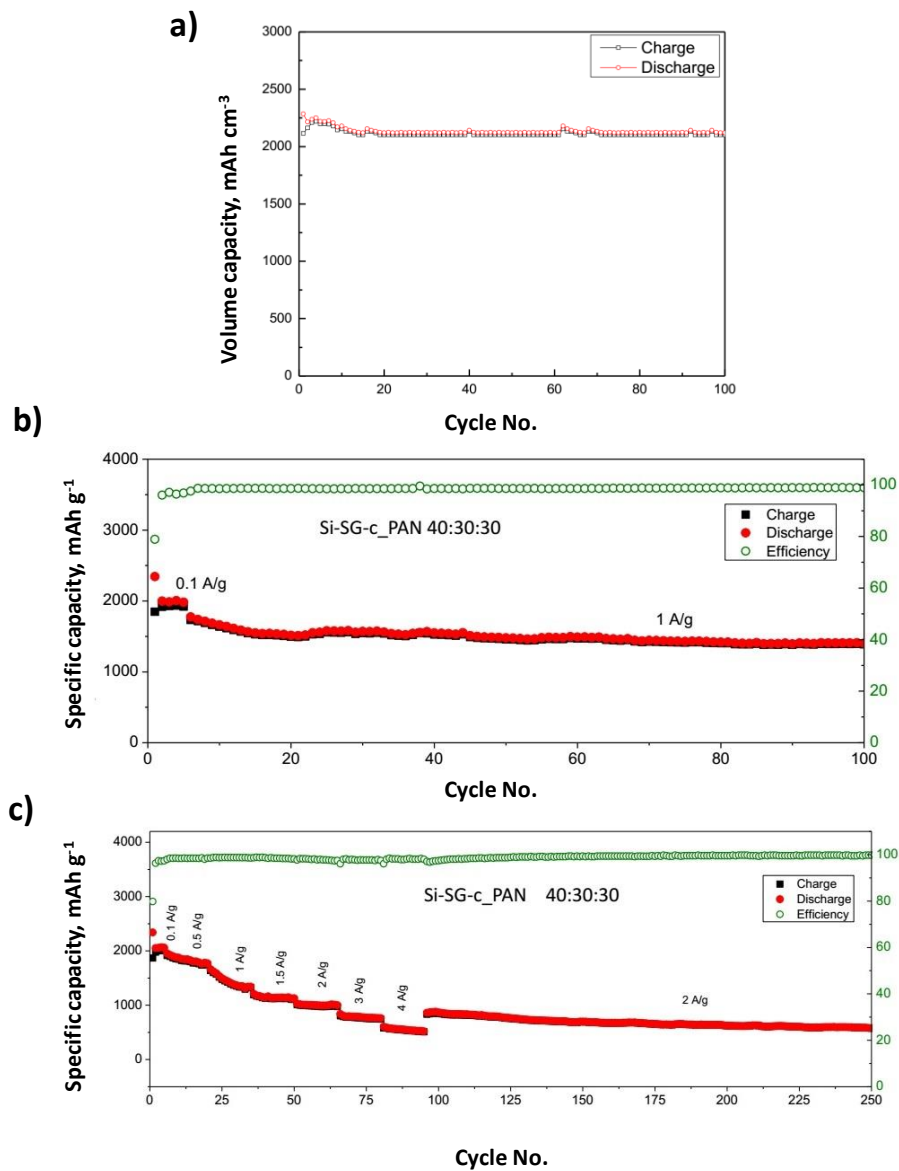
Figure 4-10 (a) Volumetric capacity of the SG-Si-c_PAN electrode shown in **Figure 4-8b**, (b) cycle stability of Si-SG-c_PAN (40:30:30) electrode, (c) rate performance and cycle stability of Si-SG-c_PAN (40:30:30). The capacity of the cell (b) and (c) are per mass of silicon and SG.

54

After cycling a coin cell for 2275 cycles (**Figure 4-8d**), the cell was disassembled and the SG-Si electrode was examined. **Figure 4-11a** shows a HAADF-STEM image of the electrode structure and **Figure 4-11b-d** provide the corresponding colored EELS maps for the elements S, C, and Si, respectively (each pixel is 3.4 x 3.4 nm). This characterization shows that the Si, as a result of frequent cycling, is confined in the wrinkles of SG and capped with cyclized PAN, utilizing the covalent interaction between Si, SG and N. The location of the SiNP is associated with regions of high sulfur and carbon. It is clear that the engineered nano-architecture of the electrode along with the covalent interaction between Si an SG has prevented agglomeration of Si and maintained stable reversible cycle stability for 2275 cycles. The same electrode is mapped using EDX for comparison and the results was presented in **Figure 4-12**. It is important to emphasize here that EELS provides a near atomic scale resolution to depict the distribution of atoms throughout the sample. EELS also has a high sensitivity for lighter elements, explaining why the signals from both carbon and sulfur are clearly distinguished. **Figure 4-11e** presents a conceptual of the electrode structure before and after frequent cycles of continuous lithiation/delithiation. On the other hand, inspection of the electrode of the cell based on G-Si-c_PAN after being cycled under the same conditions shown in **Figure 4-8e** by STEM reveals that continuous cycling leads to agglomeration of silicon (**Figure 4-13**). This emphasizes the important role of SG in preventing agglomeration of silicon and maintaining electrode stability over a large number of cycles.
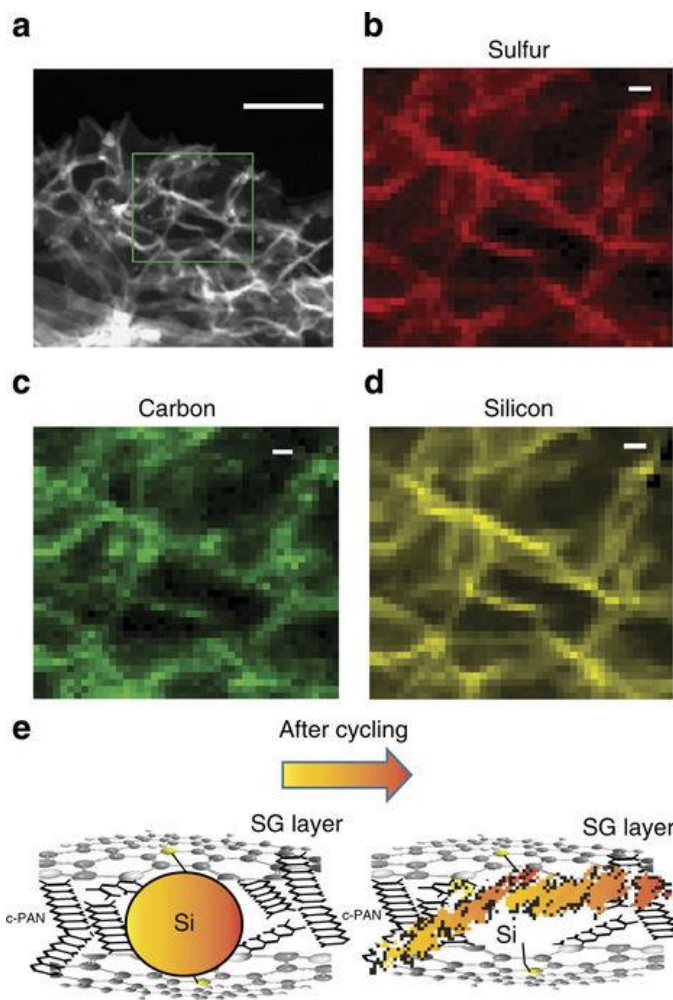
Figure 4-11 (a) HAADF–STEM image of the SG–Si electrode after cycling, (b–d) the elements mapping by EELS for the area marked in image. Scale bar, 100 nm in a and 10 nm in b–d. Each pixel in b–d represents 3.4×3.4 nm, (e) a schematic representation to explain the structure change in the electrode before and after cycling. Before battery cycling SiNP are dispersed, and bond with S on the surface of SG with c-PAN further connect the SiNP with SG. After battery cycling, the SiNP change to amorphous structure and spread and confine in the crinkles of SG.
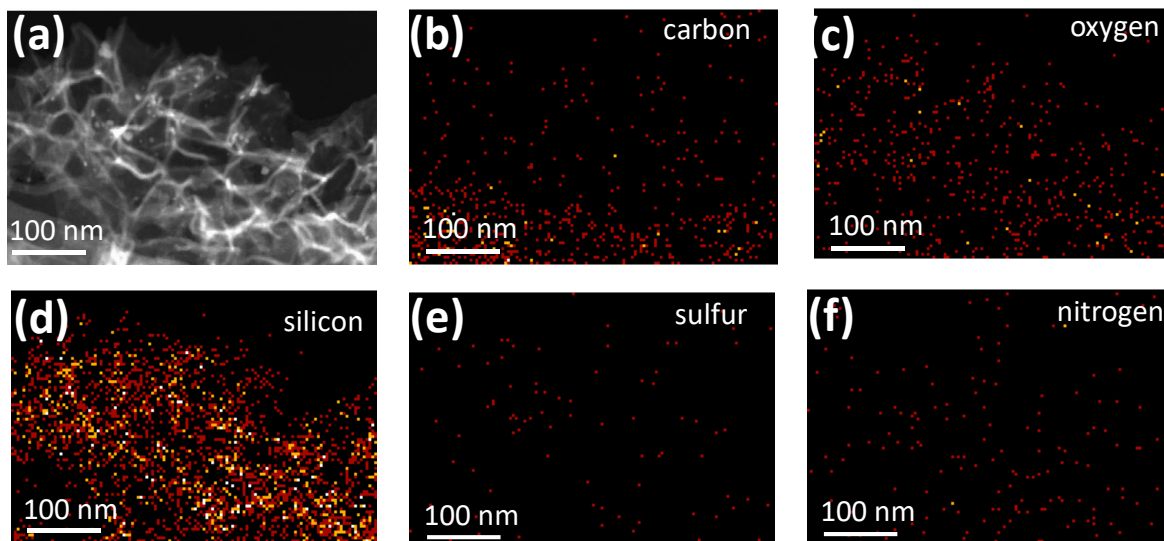
Figure 4-12 (a) STEM image of SG-Si electrode material after 2275 cycles, (b-f) the corresponding EDX mapping of the elements carbon, oxygen, silicon, sulfur and nitrogen, respectively.
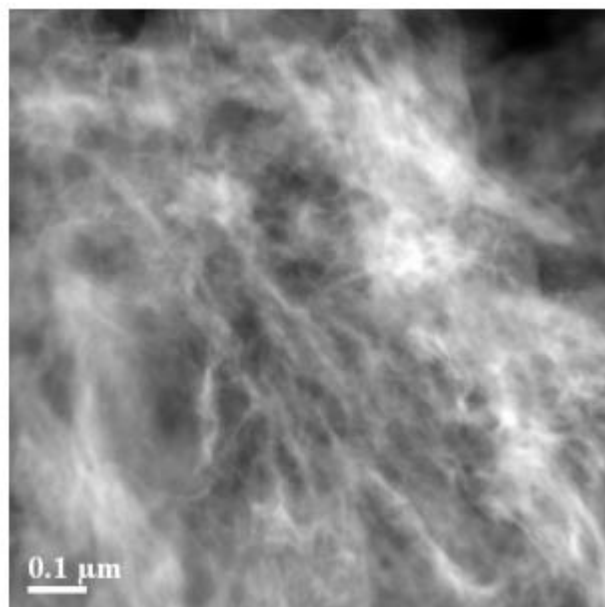
Figure 4-13 The figure shows the HAADF-STEM image of the G-Si electrode material after cycling for 800 cycles as shown in Figure 4-8e.

Density functional theory calculations. In the present study, the graphene surface is modeled using a hydrogenated graphene cluster ($C_{54}H_{18}$), which is also referred to as H-passivated graphene (**Figure 4-14**). The optimized bonding distances of C–C (1.42 Å) and C–H (1.09 Å) in this model are in good agreement with that for bulk graphite. [101] Based on this H-passivated $C_{54}H_{18}$ cluster and based on bonding configuration elucidated by XPS spectrum in **Figure 4-5d**, a structure of sulfur-doped graphene (SG) is proposed. The optimized SG structure with some key structural parameters is shown in **Figure 4-15**. It can be seen that the SG has a distorted configuration. In all the calculations, all the atoms in the cluster were allowed to relax.

a)

1.42

3 1
2

b)
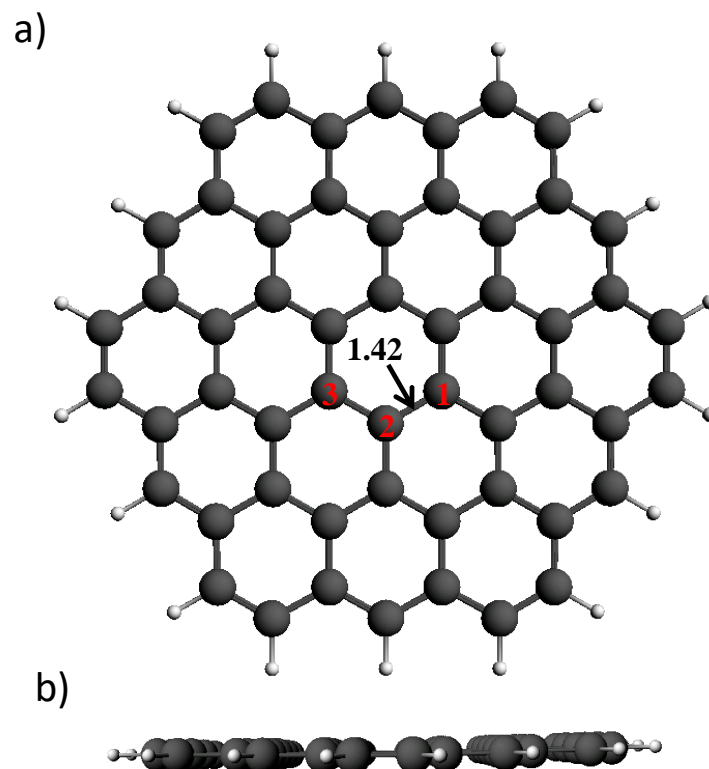
Figure 4-14 The optimized geometry of H passivated graphene (G). Carbon atoms are colored

grey, hydrogen atoms are white. Bond length is in angstrom. (a) top view, (b) side view.
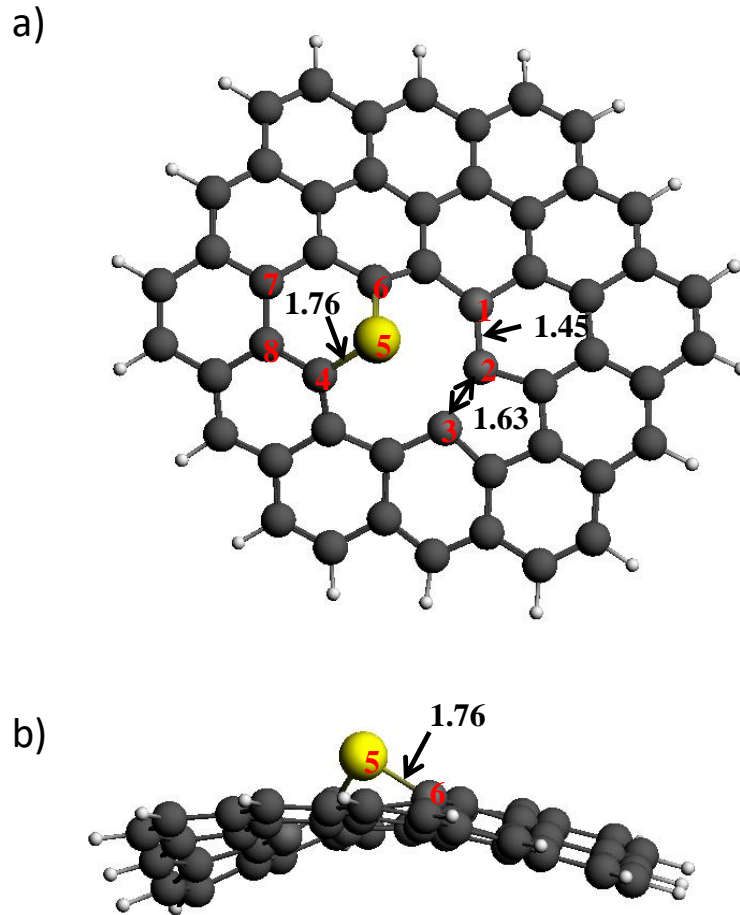
Figure 4-15 The optimized geometry of sulfur-doped graphene (SG). Carbon atoms are colored grey, hydrogen atoms are white and sulfur atom is yellow. Bond lengths are in angstrom, (a) top view, (b) side view.

In order to describe the interactions between the Si and graphene, the bonding energies (BE) of Si were defined by equation (1):

$$BE = E_{Si-graphene} - E_{graphene} - E_{Si} \tag{1}$$

where $E_{Si-graphene}$, E_{Si}, and $E_{graphene}$ represent the energies of Si-bound to the graphene structure, Si atom and graphene structure, respectively.

Si adsorption on different sites of the SG was studied. The results are compared with those obtained on undoped graphene. **Figure 4-16a** presents the configuration of stable Si adsorption on graphene (G-Si), with Si sitting at the bridge site with adsorption energy of 0.45 eV. Two stable configurations for Si adsorption on sulfur-doped graphene are observed. The first is represented as SG-Si(A) and reveals the bonding of Si to location (A) (**Figure 4-16b**). The second represents binding to location (B) represented as SG-Si(B) (**Figure 4-16c**). In SG-Si(A), Si binds to S and two "saturated" C atoms (C_7 and C_8), with the corresponding binding energy of -2.02 eV. On the other hand, at the SG-Si(B) position, Si binds to S and two C's at the defect sites (C_2 and C_3) forming two Si-C and one Si-S bonds, leading to a binding energy of -3.70 eV. The higher binding energy in the latter case indicates Si would be more energetically favorable to bind to the defect C_2 and C_3 atoms. Most importantly, the results show that Si attached on either SG structure has a much higher binding energy than that on graphene (G-Si). This result introduces a strong explanation for the much longer cycle stability of SG-Si than G-Si. The binding energy of a cluster made of 9 silicon atoms to different defect configuration in SG, **Figure 4-16d-e**, was also studied. As expected, the covalent interaction occurs between only two of the silicon atoms in the cluster adjacent to the S and defect in SG. The binding energy is also dependent on the defect configuration. **Figure 4-17** shows the binding configuration of a smaller cluster of 4 Si atoms. The same cluster binds to SG more strongly than to defect-free graphene.
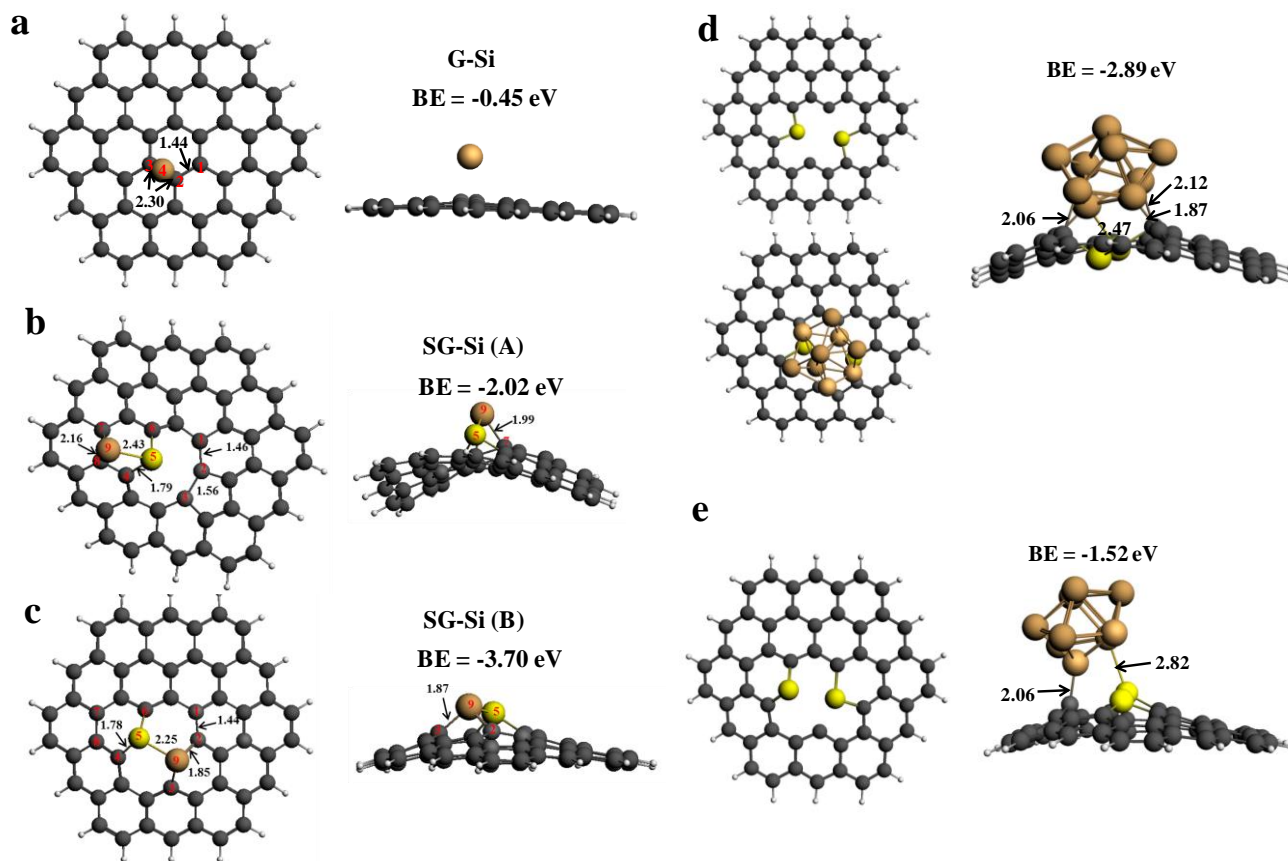
Figure 4-16 Geometries and binding energy (BE) of stable Si adsorption configurations on (a) graphene referred as G–Si; (b,c) sulfur-doped graphene, referred as SG–Si(A) and SG–Si(B), respectively, C atoms are coloured grey, H atoms white, S atom yellow, Si atom brown. Some of the important atoms are labelled, and they correspond to the atoms in Table 1, and (d,e) DFT-calculated BE of a stable cluster of nine Si atoms adsorbed to SG with different defect configurations. The bond lengths shown in the figure are in angstroms.
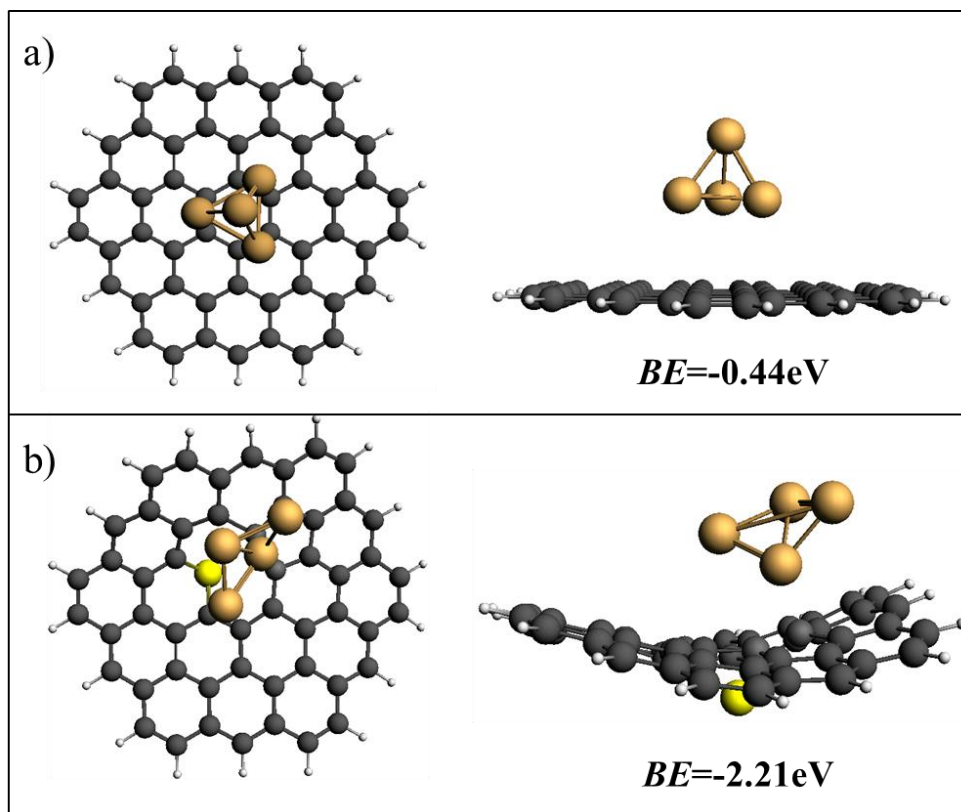
Figure 4-17 Geometries and bonding energy (BE) of stable Si_4 cluster adsorption configurations on (a) graphene and (b) sulfur-doped graphene. Carbon atoms are colored grey, hydrogen atoms are white, sulfur atom is yellow and silicon atoms are brown.

Hirshfeld charge analysis is also conducted to evaluate the stability of Si on G and SG. The calculated charge distributions before and after the Si adsorption on G and SG are given in **Table 4-1**. The results show that Si has a positive charge after its adsorption on G and SG, which indicates that electrons flow from the Si atom to the graphene substrate upon Si adsorption. However, the electron flow is more significant for Si adsorption on SG than that on G, because Si deposited on SG has a larger positive charge than that on G. **Table 4-1** also

shows that the C atoms that are bonded with the Si atom in SG-Si, such as C_7 and C_8 in SG-Si(A), C_2 and C_3 in SG-Si(B), have more negative charges than in G-Si (C_2 and C_3). All these observations indicate that the bonding between Si and SG is stronger than that on G, providing further support for the stability of Si on SG.

Table 4-1 Hirshfeld charges distribution before and after Si adsorption.

Atoms	Si adsorption on G		Si adsorption on SG		
	G	G–Si	SG	SG–Si(A)	SG–Si(B)
C_1	−0.001	−0.004	0.010	−0.006	−0.004
C_2	−0.001	−0.028	0.003	−0.022	−0.113
C_3	−0.001	−0.029	0.004	−0.013	−0.100
C_4 (or Si_4)		0.120	−0.016	−0.001	−0.019
S_5			0.093	0.214	0.206
C_6			−0.016	−0.035	−0.024
C_7			−0.003	−0.070	−0.013
C_8			−0.009	−0.028	−0.006
Si_9				0.190	0.145

To better understand the covalent synergy between Si and graphene substrates, the projected density of states (PDOS) of the Si atom over G and SG are calculated based on the electron structure and bonding. As shown in **Figure 4-18a**, there is a harmonic 2p-2p overlaps between the C_1-2p and C_2-2p states at the whole energy level (from 0 to -10eV) in G, showing the strong interaction between the two C atoms. However, for Si and C, the harmonic overlap occurs only between Si_4-2p and C_2-2p at a narrow energy level (-2~-4eV), indicating a weak interaction between Si_4 and C_1 atom. For SG-Si (B), a large overlap between the C_6-2p and S_5-2p state is

observed (**Figure 4-18b**), indicating a strong S-C bonding. **Figure 4-18c** shows that, more Si_9-2p state is occupied in SG-Si (B) and well mixed with C_2-2p state at a much broader energy level (from -1 to -9eV) as compared with that in G-Si. Additionally, there is also a harmonic overlap between Si_9-2p and S_5-2p state (**Figure 4-18d**). The analysis of the PDOS reveals that the covalent synergy arises mainly due to the mixing between the C-2p and Si-2p states and the C_2-Si_9 bond is much stronger than the C_2-Si_4 bond in G-Si, which attributes to the significantly improved cycle stability.
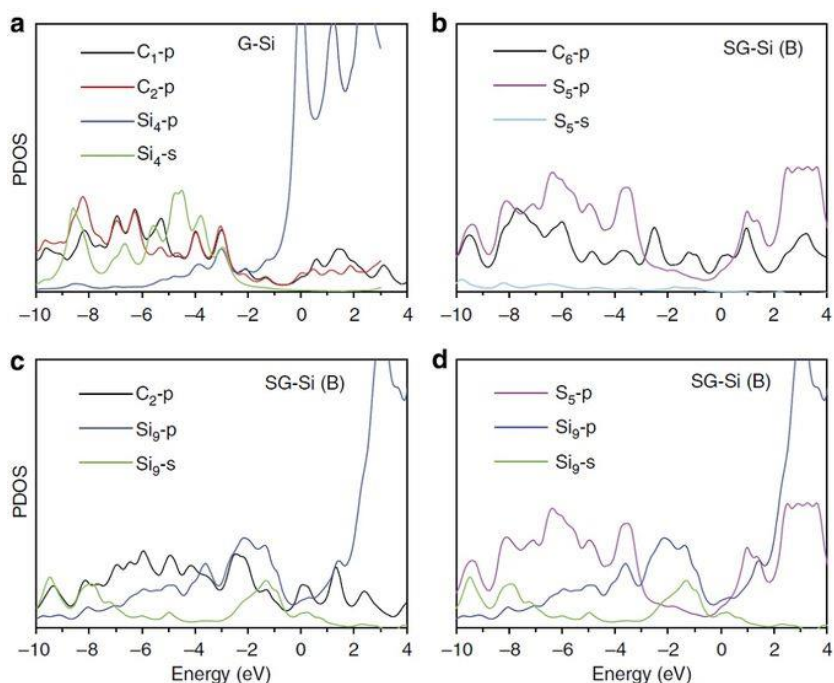
Figure 4-18 The PDOS for Si atom and the individual C atoms involved in (a) Si adsorption on graphene, G–Si, and (b–d) Si adsorption on sulfur-doped graphene, SG–Si(B).

The mobility of the adsorbed Li atom has also been studied. **Figure 4-19** shows the transition state along the diffusion pathway. In order for Li atom to diffuse away from the aforementioned

stable sites in G-Si, it must overcome an energy barrier of 0.75eV, as shown in **Figure 4-19a**.

However, Li surface diffusion along a SG-Si(B) cluster has a barrier of 0.53eV (**Figure 4-19b)**

which is slightly lower than that found on G-Si. This observation indicates that sulfur-doped

graphene could boost the mobility for Li atoms on Si-SG interface and facilitate charge

transfer.
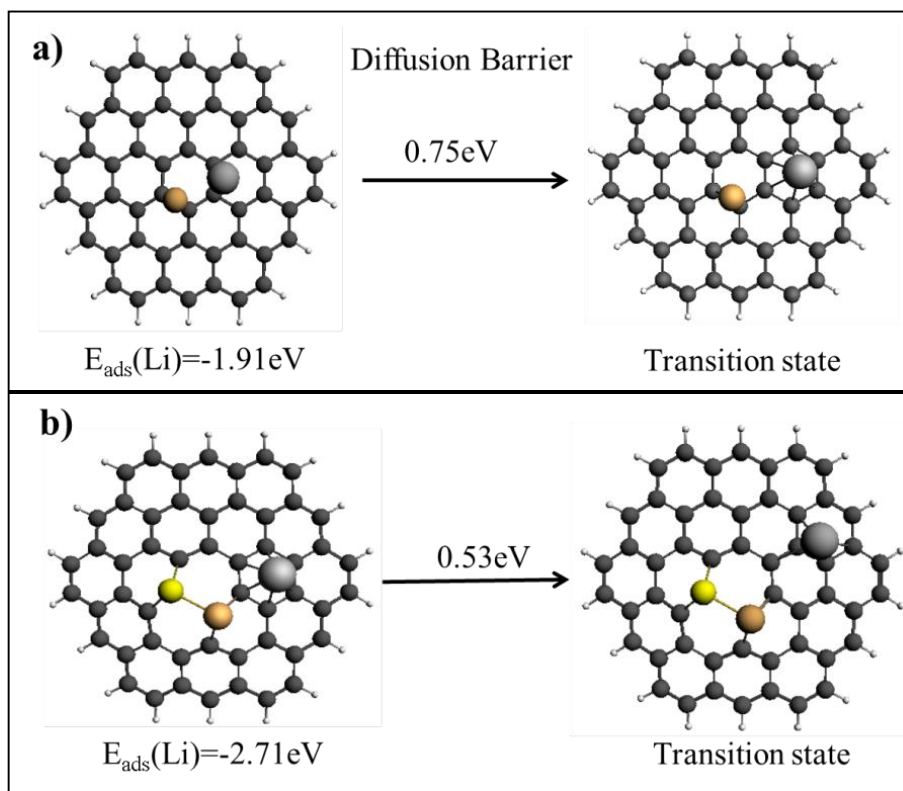
Figure 4-19 Lithium (Li) adsorption and transition state. The figure quantifies the Li diffusion

barrier for (a) G-Si and (b) SG-Si.

Discussion

According to the results presented above, we ascribe the enhanced cycling stability and improved rate capability to the robust, nano-architectured and structurally stable electrode design. This capitalizes on the changes to electrode processing. During the SHT process several changes to the electrode structure are proposed. First, PAN is cyclized by forming graphitized carbon with a 6 membered ring structure hosting the nitrogen atoms in a pyridine-like assembly. Secondly, silicon is anchored and covalently interacts with sulfur atoms, activated carbon associated with nanoholes in SG and nitrogen in the cyclized PAN. Thirdly, the reconstruction and atomic scale architecturing of the electrode lead to a robust structure in which the SiNP is protected by a scaffold of graphene nanosheets and a web of cyclized PAN (c-PAN). The c-PAN effectively shield around the SiNPs, which are already anchored to SG through covalent interactions as confirmed by DFT calculations. In addition, c-PAN sticks between the SG nanosheets, providing a 3-D dimensional, interconnected structure that enables enhanced conductivity and material robustness, as shown schematically in **Figure 4-1d.**

After 2275 repetitive expansion and contraction cycles, SiNPs fractured and pulverized into smaller particles. However, these fractured Si particles are still confined within the continuous channels of the c-PAN shell, which is overlaid on SG and maintains the electrical connection between Si and graphene. The synergy of the interactions within Si/SG/c-PAN leads to excellent cycle efficiency and capacity retention. The unique and elegant special arrangement of the 3D structure of the electrode provides critically sized voids along with elasticity to accommodate repetitive volume expansion and contraction. This helps preserve electrode

integrity and prevent degradation. Furthermore, sandwiching of SiNPs capped with cyclized PAN between SG nanosheets forms laminated structure with limited open channels. This suppress the penetration of the electrolyte into the bulk of the electrode and limits most of the SEI formation to the surface. We believe the TEM (EELS) images shown in **Figure 4-11** provide some indirect evidence that most of the SEI forms on the outside. The surroundings of Si are quiet clean. If the SEI formed on Si nanoparticles, one should see large amounts of SEI covering Si since it is difficult for the fractured SEI to come out. Another possibility is that the SEI would preferentially form on the defective areas in the graphene, which might reduce access of solvent to the space inside. Here, we are trying to emphasis that most of SEI forms on the graphene surface, which is more stable compared with that formed on a Si surface.

Based on our DFT model, Si atom interacts covalently with a sulfur atom in SG and two adjacent carbon atoms. The equivalent strength of this covalent interaction is similar to that of a single covalent bond. This interaction may not involve the Si atom reacting directly with sulfur to form either SiS or SiS_2, as this would require debonding of sulfur from within the graphene matrix and may result in electrode degradation. In the case of Si clusters (to simulate nanoparticles), only a small portion of the silicon atoms covalently interact with the SG. We believe that this type of Si does not participate in alloy formation with lithium; instead, it provides an anchoring site for the majority of Si atoms within the nanoparticle that are readily available for alloying/dealloying and thereby contributes to the observed capacity.

It can be seen that Si bonds more strongly to SG than on G. One reason is the covalent interaction of Si atoms with the sulfur atom. The second reason is the increased charge density

on the defective (with nanoholes) carbon adjacent to sulfur. This indicates the covalent synergy for the interaction between Si and SG leading to superior material electrochemical performance, which is not evident with Si-G. After 2275 cycles of charge/discharge, the amorphous SiNP has re-organised into channels of the cyclized PAN and the sulfur pathway on graphene, as seen in **Figure 4-11**.

4.4 Conclusion

In summary, the novel design of a Si-based electrode through the covalent binding of commercial SiNP and SG along with cyclized PAN offers exceptional potential in the practical utilization of Si anodes for lithium-ion battery technologies. This covalent synergy enables superior cycling stability along with a high areal capacity of the electrode which is close to that of commercial technologies. Such a rational design and scalable fabrication paves the way for the real application of Si anodes in high-performance lithium-ion batteries. The interaction between S and Si plays a critical role of improving the long-term cycle stability, additionally, the synergistic effect of the covalent bonds between Si-S, the facilitated charge transfer by 3D graphene network and cyclized PAN, and the improved electrode integrity all attributed to the superior cycle performance.

Chapter 5

Wet milling of Micron-Sized Silicon as a Top-Down Approach to Prepare Nano-architectured Electrodes

This chapter is adapted from a manuscript that is accepted in Journal of Power Sources.

"Highly Durable 3D Conductive Matrixed Silicon Anode for Lithium-ion Batteries."
Submitted to "Journal of Power Sources", 18-01738R2

Batmaz, R., Hassan, F.M., Higgins, D., Cano, Z.P., Xiao, X., and Chen, Z., 2018.

5.1 Introduction

Lithium-ion (Li-ion) batteries are ubiquitous rechargeable devices that dominate the portable electronics market. However, their limited energy density does not meet the requirements of long-range electric vehicles and long-duration grid-scale energy storage systems.[102] In the past decade, intense efforts have focused on the development of next generation positive and negative electrodes to increase the storage capacity of Li-ion batteries. For the negative electrode, silicon has attracted significant attention due to its high lithium storage capacity ($\sim$4200 mAh g^{-1}), low discharge potential ($\sim$0.5V versus Li/Li^+), natural abundance and environmentally friendly properties.[59, 71] However, the enormous volume change of silicon particles during lithium insertion and extraction causes them to be pulverized. This results in loss of electrical contact within the electrode and formation of an unstable solid-electrolyte interface (SEI) on the silicon surface, ultimately manifesting in rapid capacity decay.[64, 103, 104]

Since the pioneering work of Cui et al.[57] on silicon nanowires as anode active materials, silicon nanomaterials have been extensively used to address the aforementioned problems.[26-28, 32, 67, 104, 105] Below a critical size of 150 nm silicon is intrinsically resistant to particle fracturing and helps to maintain the integrity of the electrode.[25] Furthermore, small particle sizes shorten the lithium ion diffusion path lengths, leading to less polarization and enhanced rate performance. In the last several years, nano-architectured silicon electrodes have been fabricated to improve the stability of silicon-based anodes. This has involved the use of silicon nanoparticles[26-28, 32, 67, 68] silicon nanowires[105, 106] and nanotubes[104]. Despite good cycling performance achieved with these unique electrode architectures, their commercialization is not yet feasible due to the processing complexity associated with nanostructuring of silicon materials, often requiring expensive and complex synthesis methods such as chemical vapor deposition or template growth. Therefore, the utilization of silicon microparticles (SiMPs) is more attractive due to their widespread availability and low cost.

In earlier studies, the durability of SiMPs suffered significantly from particle fracturing and detachment from the electrode surface upon deep discharging[39-41], leading to a poor cycle life including a 20 % capacity loss in just 10 cycles. The cycling stability limitation of SiMPs electrodes was circumvented by applying a cut-off voltage. This helped to maintain a two-phase (crystalline-amorphous) silicon microstructure in which only the amorphous phase is active.[40] However, the approach reduced the energy density of the electrode since the crystalline core of the particle remained inactive.[40] To address this problem, SiMPs were engineered by chemical etching with hydrofluoric acid to create internal void spaces in the

electrode to buffer the volume change occurring with deep galvanostatic cycling[42-44], whereas exterior void spaces were created by encapsulating the SiMPs with graphene.[45] Despite promising improvements to cycling performance, the scalability of these electrode manufacturing processes was limited due to the hazardous nature of the etching techniques. Aside from chemical etching, ball milling of SiMPs with carbon materials has been extensively used to reduce the silicon particle size and enhance cycling performance.[107-111] However, the cells prepared from these SiMPs-carbon composites suffered from electrode level fracturing[29], which resulted in low capacity and insufficient cycle life. This arose due to the mechanical nature of milling, which enabled only physical mixing of components, as opposed to forming an intimate and strategic electrode structure.

It would therefore be useful to redesign existing processing techniques to engineer desired electrode structures and enhance battery cycling. Heat treatments are a popular electrode fabrication technique to carbonize polymeric precursors around electrode active materials (i.e., silicon) and enhance the electronic connectivity throughout the entire 3D electrode structures. However, the volumetric changes during battery cycling commonly detach the electrode from the current collector, resulting in electronic conductivity losses and poor electrode utilization due to active material isolation. Heat treatment should therefore be tuned not only to help enhance the electronic interconnectivity of the active materials, but also to induce void space formation that can provide mechanical stability during battery cycling.

In the present chapter, we develop a two-stage top-down approach to prepare core-shell structured silicon-carbon nano-composite electrodes using commercially available micron-

sized silicon particles as precursors. In the first stage, a new fluid-induced fracture (FIF) technique is applied to a slurry consisting of SiMPs, sulfur-doped graphene (SG), polyacrylonitrile (PAN) and dimethylformamide (DMF). This FIF process is carried out to reduce the size of SiMPs, before being coated on a copper foil current collector. After drying, the electrodes are subjected to thermolysis to modify the chemical structure of the binder and architecture of the electrode. The synergistic effect of FIF and thermolysis results in a hierarchically structured silicon anode in which broken down SiMPs are wrapped with cyclized PAN (cPAN) and SG sheets. This conductive matrix surrounding the silicon particles provides high mechanical resiliency, helping to accommodate significant volume change, while enhancing the electronic conductivity of the electrodes through the intrinsic conductivity of the delocalized electrons of cPAN and SG sheets. In addition, the cyclization of PAN induces the formation of micron-sized channels throughout the electrode structure. These void micro-channels act as a mechanical buffer for the anisotropic volume changes of silicon particles during battery charging/discharging, thereby preventing electrode pulverization. This electrode architecture leads to superior performance compared with conventional electrodes. FIF and thermolysis provide new routes for low-cost electrode preparation with excellent electrochemical performance. Furthermore, the fabrication approach developed herein provides an efficient and non-hazardous manufacturing process for SiMPs based anodes that can be deployed on a commercial scale.

5.2 Experimental section

5.2.1 Preparation of Graphene Oxide (GO)

The reaction procedure to prepare GO from natural graphite flakes was adapted from the James Tour method.[72] A 9:1 mixture of concentrated H_2SO_4/H_3PO_4 (360:40 mL) was poured into a beaker containing 3 g graphite powder. The solution was mixed for 30 min in an ice bath before adding 27 g of $KMnO_4$ and mixing for another 1 hour. The contents were then transferred to a hotplate and stirred at 50 °C. After the reaction was completed, 600 mL distilled water was added to the solution while it was being stirred in an ice bath. After the addition of water, 30 mL hydrogen peroxide (H_2O_2) was poured into the solution to reduce the unreacted $KMnO_4$. The final solution was washed several times with 5 % HCl solution and distilled water by centrifugation.

5.2.2 Preparation of Sulfur-Doped Graphene

100 mg of GO was mixed with 100 mg of phenyl disulfide by grinding. The materials were loaded into a tube furnace and kept outside the heating zone until the furnace temperature reached 1,000 °C. The sample was then moved into the heating zone where it remained for 30 minutes under argon protection, followed by cooling to room temperature.

5.2.3 Electrode Fabrication and Coin Cell Assembly

The electrodes were fabricated by directly coating a slurry onto copper foil using the Blade method. The SG-SiMPs-PAN slurry was prepared by wet ball milling 55 wt% SiMPs, 22 wt% PAN, 22 wt% SG and 1 wt% GO in presence of dimethylformamide (DMF). After coating the

slurry, the electrode was dried in a convection oven at 80 $^{\circ}$C overnight. This foil was punched by a disc cutter to form circular working electrodes that were than subjected to thermolysis at 450 $^{\circ}$C in an argon atmosphere. The heating ramp during annealing was 7.5 $^{\circ}$C min^{-1}.

Coin-type half cells were assembled in a glove box under an argon atmosphere in which the oxygen and water moisture levels were less than 0.5 ppm. The electrolyte was LiPF$_6$ (1M) dissolved in 60 wt% dimethyl carbonate (DMC), 30 wt% ethylene carbonate (EC) and 10 wt% fluorinated ethylene carbonate (FEC). Lithium metal was used as the counter electrode. The electrodes were separated using a polypropylene separator (PP2075, Celgard). The battery performance was tested by galvanostatic charge/discharge cycling using a battery testing instrument (BTS 3000, Neware, China). These cycles were conducted between cut-off voltages of 0.01 V and 1.1 V for discharge and charge, respectively. Different current densities were applied to investigate the rate capability. Finally, the coin cells were subjected to cyclic voltammetry between 1.5 V and 0.01 V at a rate of 0.05 mV s^{-1} using an electrochemical testing platform (Princeton Applied Research, VersaSTAT MC Potentiostat). A conventional/reference cell was fabricated using 60 wt% SiMPs, 20 wt% Super P and, 20 wt% polyvinylidene fluoride (PVDF) and was tested under the same conditions as were the SG-SiMPs-cPAN cells for comparison purposes.

5.2.4 Material Characterization

The morphology and the structure of the electrode materials were examined using scanning electron microscopy (SEM, LEO FESEM 1530) and transmission electron microscopy (TEM, JEOL 2010F TEM/STEM field emission microscope) equipped with a large solid angle for

high X-ray throughput and a Gatan imaging filter (GIF) for energy-filtered imaging. Thermal analysis of samples was conducted by differential scanning calorimetry (DSC) and thermogravimetric analysis (TGA) using a TA instrument Q500. PAN was heated under nitrogen atmosphere from 25 °C to 850 °C at a ramp rate of 10 °C min^{-1}. Raman spectra of PAN film and electrodes were recorded using a Bruker Senterra with a laser wavelength of 532 nm. FTIR analysis was conducted using a PerkinElmer-283B FT-IR spectrometer. XRD analysis was done by using monochromatic Cu K x-rays (154 nm wavelength) and an Inel XRG 3000 diffractometer. Atomic force microscopy (AFM) measurements were conducted with a Bruker Innova AFM in tapping mode.

5.3 Results and discussion

The developed electrode preparation process is shown schematically in **Figure 5-1a**. The FIF technique involved wet milling of SiMPs, SG and PAN in the presence of DMF to prepare the slurry. One hour of milling was sufficient to reduce the size of the silicon particles from the micro- to the nanoscale, compared to previous studies that employ milling times of 4h to 150h.[107-111] The presence of fluid during the milling process accelerates silicon microparticle fracture into nanoparticles in a manner we consider to be similar to the accelerated break down of geological rock formations in the presence of a pressurized fluid.[112-114] Scanning electron microscopy (SEM) images (**Figure 5-1b-c**) and corresponding statistical analyses (**Figure 5-1d-e**) show that the size of the SiMPs reduced from ca. 3.0 microns to ca. 500 nanometers (**Figure 5-1f**) after one hour of FIF. Conversely, when SiMPs are dry-milled for 1h in the absence of a fluid, their size is reduced to only ca. 1.2 microns, demonstrating the important

role the fluid plays in the size reduction of SiMPs (**Figure 5-2a-b**). Furthermore, as shown in **Figure 5-2c-d**, the broadening of the primary silicon (220) x-ray diffraction (XRD) peak reveals the reduction in crystallinity and average crystallite size of the SiMPs that undergo FIF. After slurry coating on a copper foil current collector, the thermolysis process is applied at 450 ºC in an argon environment to modify the electrode architecture. Upon thermolysis, no material rupture and deflagration are observed even after the electrodes are twisted and bent as shown in **Figure 5-3** which is attributed to the mechanical resiliency of the cPAN.
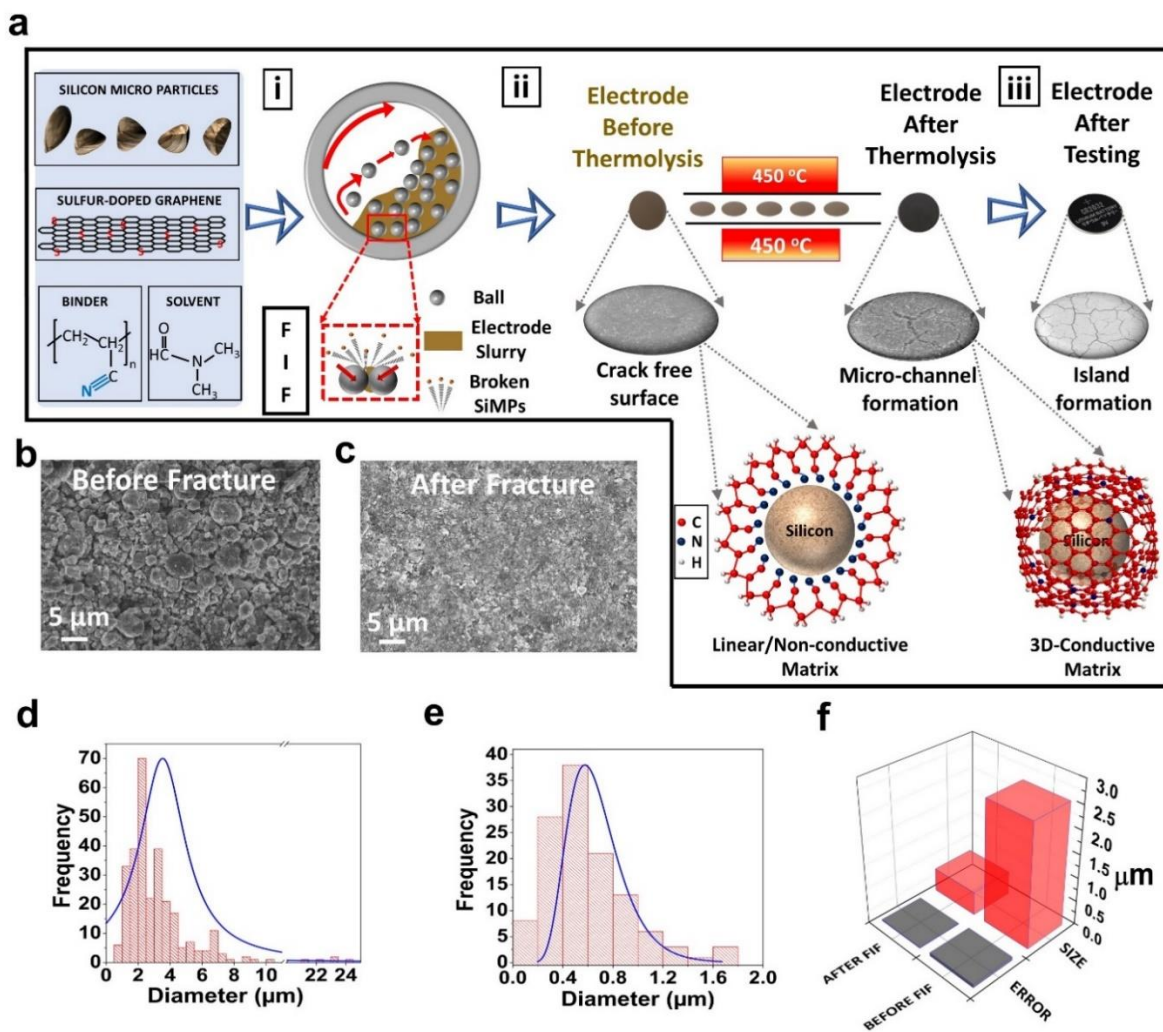
Figure 5-1 (a) Schematic of the electrode fabrication process: (i) milling of the electrode slurry before coating; (ii) thermolysis of the electrodes; (iii) integration into coin cells for battery testing, (b) SEM image of SiMPs before FIF, (c) SEM image of electrode surface after FIF, (d) particle size distribution of SiMPs before FIF, (e) particle size distribution of SiMPs after FIF, (f) average particle size comparison of SiMPs before and after FIF.
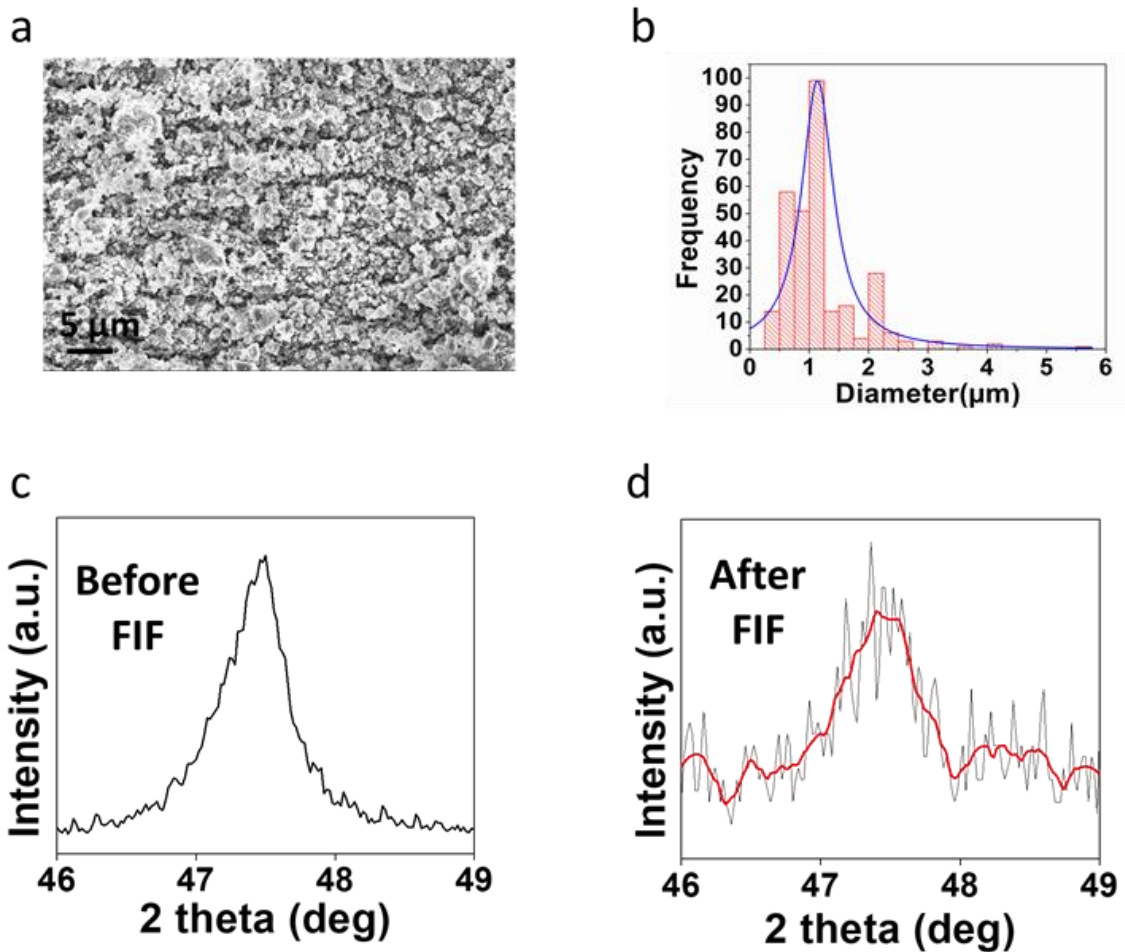
Figure 5-2 (a) SEM image of SiMPs after one-hour dry ball milling, (b) particle size distribution of SiMPs after one-hour dry ball milling, (c) X-ray diffraction scan of silicon 220 peak before fluid-induced fracture (FIF), (d) X-ray diffraction scan of silicon 220 peak after fluid-induced fracture (FIF), the red curve is the smoothed version.
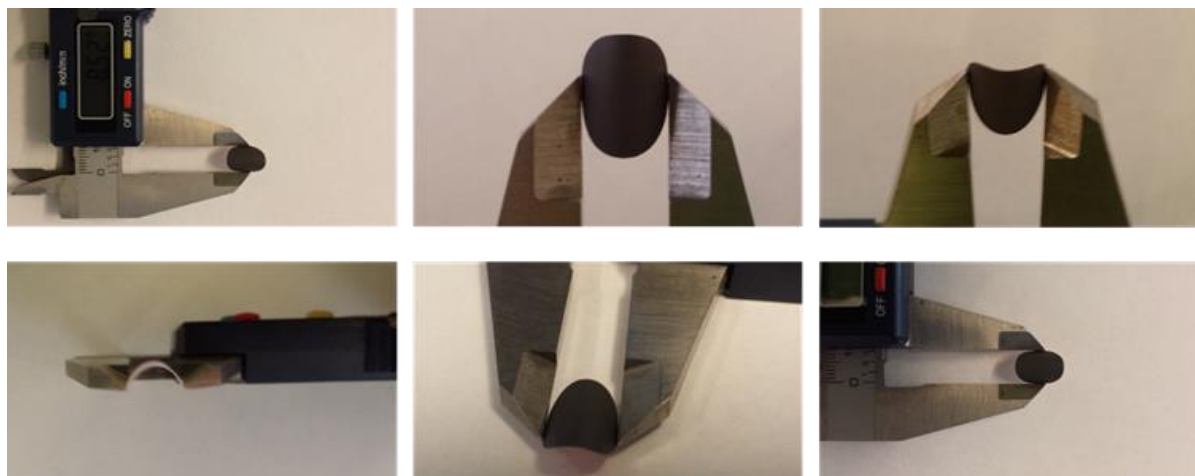
Figure 5-3 The bending of electrodes after thermolysis showing no material rupture and deflagration.

Differential scanning calorimetry (DSC) was used to elucidate the thermal behavior of PAN. As shown in **Figure 5-4a**, a sharp exothermic DSC peak at ~ 300 °C is attributed to the cyclization of the polymer backbone (**Figure 5-5a**). Thermal gravimetric analysis (TGA) is also in good agreement with DSC. The mass loss is initiated at a temperature similar to where the DSC peak appears. In this region, 20 % of the mass loss stems from the dehydrogenation of the polymer structure upon the formation of π conjugate bonds.[115] In addition to the thermal analysis, the chemical transformation of PAN is elucidated by Fourier transform infrared spectroscopy (FTIR) (**Figure 5-4b**). Of particular interest is the cyanide group (C≡N) since its peak is expected to disappear after cyclization of PAN. For pristine PAN, the peak at 2243 cm⁻¹ is assigned to the C≡N stretching, while the other peaks at 1363, 1456 and 2935 cm⁻¹ are characteristic of δ_{C-H} in CH, δ_{C-H} in CH$_2$ and ν_{C-H} in CH$_2$, respectively (**Figure 5-4b**). [116, 117] After undergoing thermolysis the C≡N peak at 2243 cm⁻¹ disappears. At the same time, a

distinct peak which can be attributed to C=C and C=N stretching appears at 1610 cm^{-1} [118] (**Figure 5-4b**) . This is consistent with the transformation of PAN from a linear chain structure to a graphite structure due to cyclization (depicted schematically in **Figure 5-5a**). In addition, the disappearance of the C≡N peak at 2243 cm^{-1} is also observed when the mixture of PAN, SiMPs and SG is subjected to thermolysis (**Figure 5-4b**). This process leads a robust 3D elastic and conductive network within the electrode, facilitating the charge transfer between the silicon particles, SG sheets and copper surface. Furthermore, FTIR spectra also provides insight into the possibility of interaction between the silicon atoms on the particle surface and cPAN after thermolysis. The peak at 840 cm^{-1} is assigned to the asymmetric stretching mode of Si-N (**Figure 5-6**).[119] We believe that cPAN may bind with silicon atoms on the surface of the particles. This bond can help cPAN to strongly attach on the surface of silicon particles, and so stabilize the electrode structure and prevent agglomeration. Cyclization of PAN yields a sheet-like morphology analogous to layered nitrogen-doped graphene (NG). The TEM image in **Figure 5-4e** clearly shows that the PAN cyclization after thermolysis forms sheet-like morphology believed to be multi-layered NG.

The further characterization of the sheets with electron energy loss spectrum (EELS) shows the typical carbon-K ionization and nitrogen-K ionization edges (**Figure 5-5f-g**). This reveals that PAN cyclizes under the influence of thermolysis and changes its structure from a linear chain to sheets of nitrogen-doped multilayer graphene (NG). Such a structure forms a robust and flexible skeleton that acts as a nest hosting the broken SiMPs. Raman spectra of PAN and

the electrodes clearly confirm the formation of G-band and D-band after thermolysis (**Figure 5-5**).

To study the crystalline structure of NG sheets, X-ray diffraction is employed, and the results are provided in **Figure 5-5e**. No obvious peak appears before thermolysis, whereas a major peak (002) at ~ $25.8 \pm 0.2°$ appears after thermolysis. The crystal size is calculated to be 2.17 nm by using the Scherrer equation on this peak. The corresponding interlayer spacing for the NG is 3.45 Å and the number of layers is 6.3. The structural evolution of the SG-SiMPs-PAN composite is further investigated by X-ray photoelectron spectroscopy (XPS) before and after thermolysis. **Figure 5-4c** shows the N 1s spectra of the SG-SiMPs-PAN composite, which clearly confirms the transformation of some of the nitrile nitrogen (C≡N, 400.1 eV) to pyridinic nitrogen (398.6 eV) after thermolysis.[85, 120] XPS spectra of C1s in **Figure 5-4d** reveals four distinct peaks at 288.9, 287.2, 285.7 and 284.6 eV. Peaks (1) and (2) are attributed to sp^2 bonded carbon (graphitic) and sp^3 hybridized carbon (diamond), respectively. Peaks (3) and (4) show the presence of a small amount of oxygenated carbon. The XPS spectrum of C 1s reveals the enrichment of sp^2 carbon after thermolysis, as shown in **Figure 5-4d**. Further inspection of the electrode structure is included in **Figure 5-5.** Raman spectroscopy is used to the investigate the change in molecular structure of polyacrylonitrile (PAN) before and after thermolysis (TH) (**Figure 5-5b**). Before thermolysis, no Raman peak is observed, whereas two characteristic peaks ('D' and 'G' bands) for carbonaceous materials appeared at 1346 cm^{-1} and 1605 cm^{-1}, respectively after thermolysis. These peaks are attributed to sp^3 and sp^2 hybridized carbon atoms, respectively. The I_D/I_G ratio is calculated to be 2.08. **Figure 5-5c-d** shows the

Raman spectra of the SG-SiMPs-PAN electrode before and after thermolysis. The increase in the intensity of 'D' and 'G' bands after thermolysis can be attributed to the graphenization of PAN. In addition, broadening of the Si peak and a shift to slightly lower wave numbers can be attributed to higher stress on the Si surface due to the cyclized PAN.

The above discussion elucidating the electrode structure reveals that the electrodes subjected to thermolysis possess multilayer architecture comprising SG, and NG resulting from cPAN. The silicon particles are nested and sandwiched between these multi-layered structures. The covalent interaction between the high electronegative atoms of N/S, and C/Si maintains the electrode stability by preventing agglomeration, in addition to strong adherence to the current collector.[26] The robust/strong nature of the layers of SG and the in-situ formed NG provide a strong and elastic skeleton that compensates volumetric changes during charge/discharge.
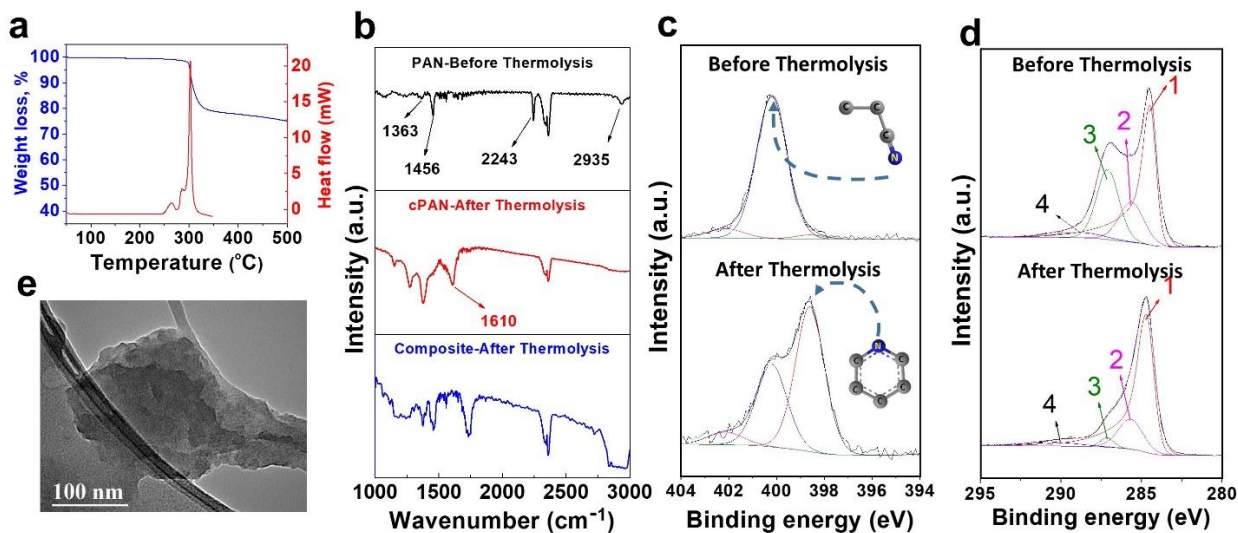
Figure 5-4 (a) Thermal characterization of PAN by DSC and TGA, (b) FTIR spectra of PAN before and after thermolysis and SG-SiMPs-cPAN composite after thermolysis, (c) high resolution XPS spectra of nitrogen in SG-SiMPs-PAN composite before and after thermolysis,

83

(d) high resolution XPS spectra of carbon in SG-SiMPs-PAN composite before and after thermolysis, (e) TEM image of cPAN after thermolysis.
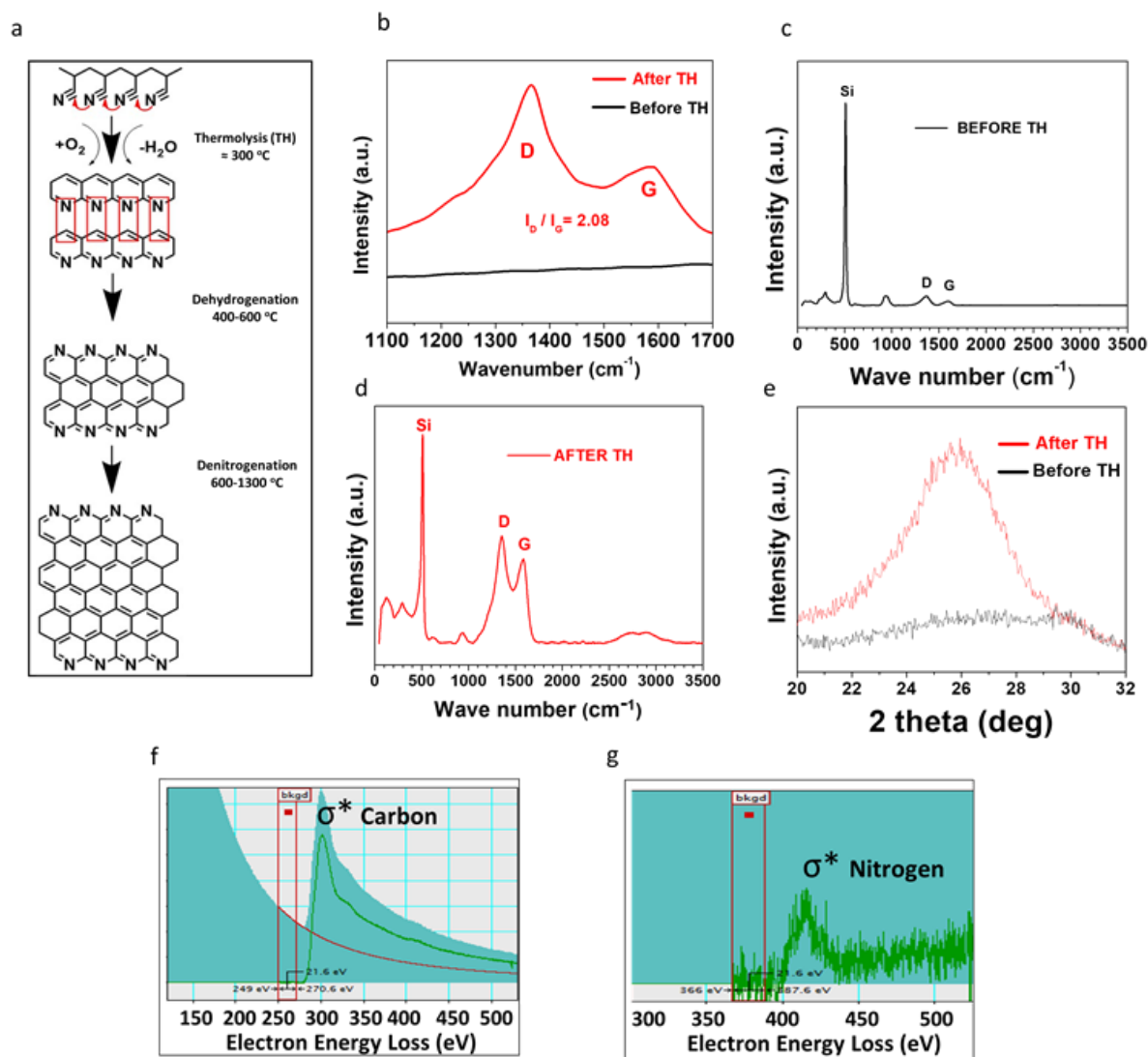
Figure 5-5 (a) Schematic of PAN thermolysis (TH) involving dehydrogenation and denitrogenation, (b) Raman spectra of PAN before and after thermolysis, (c) Raman spectra of SG-SiMPs-PAN electrode before thermolysis, (d) Raman spectra of SG-SiMPs-cPAN electrode after thermolysis, (e) X-ray diffraction scan of PAN before and after thermolysis, (f)

EELS profile of cPAN after thermolysis showing carbon-K edge, (g) EELS profile of cPAN after thermolysis showing nitrogen-K edge.
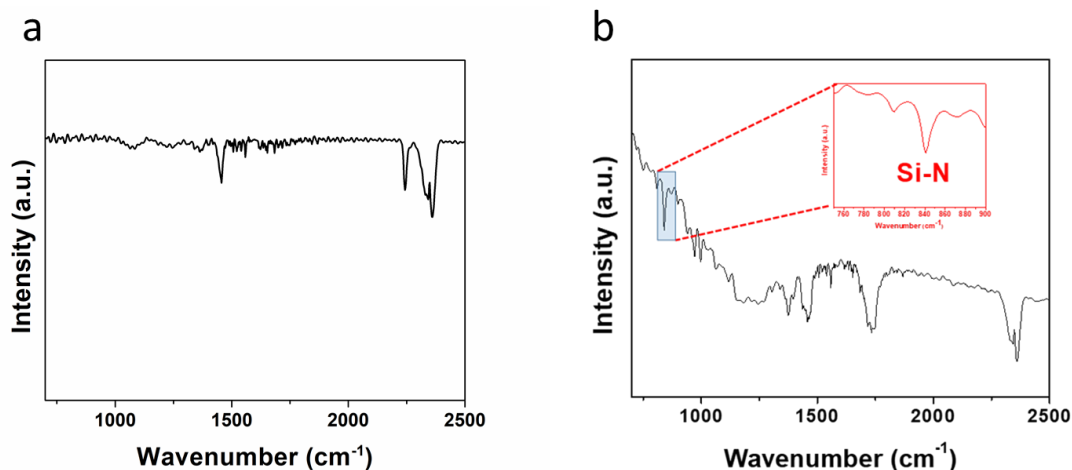
Figure 5-6 FTIR Spectrum of (a) PAN before thermolysis (b) SG-SiMPs-cPAN composite after thermolysis.

The electrode morphology and structure are investigated by high-angle annular dark field scanning transmission electron microscopy (HAADF-STEM). In this imaging mode, the regions of silicon particles appear brighter compared to the regions of the carbon matrix. The HAADF-STEM image (**Figure 5-7a**) and corresponding energy dispersive spectroscopy (EDX) maps (**Figure 5-7b-e**) clearly show that the silicon particles are embedded in the carbon matrix after thermolysis. To focus more on the surface of the silicon particles, electron energy-loss spectroscopy (EELS) have been obtained in selected region of Si_1 (**Figure 5-7f-k**). The brighter areas indicate the location of the corresponding elements. Silicon atoms are surrounded by carbon (C), nitrogen (N), oxygen (O) and sulfur (S) atoms. This further confirms that the silicon particles are wrapped by the carbon matrix of NG and SG, which are the only

sources of C, S, N and O atoms. This illustrates that the cyclization of PAN takes place close to the surface of silicon particles and helps to form a robust electrode structure with high mechanical resiliency and conductivity.
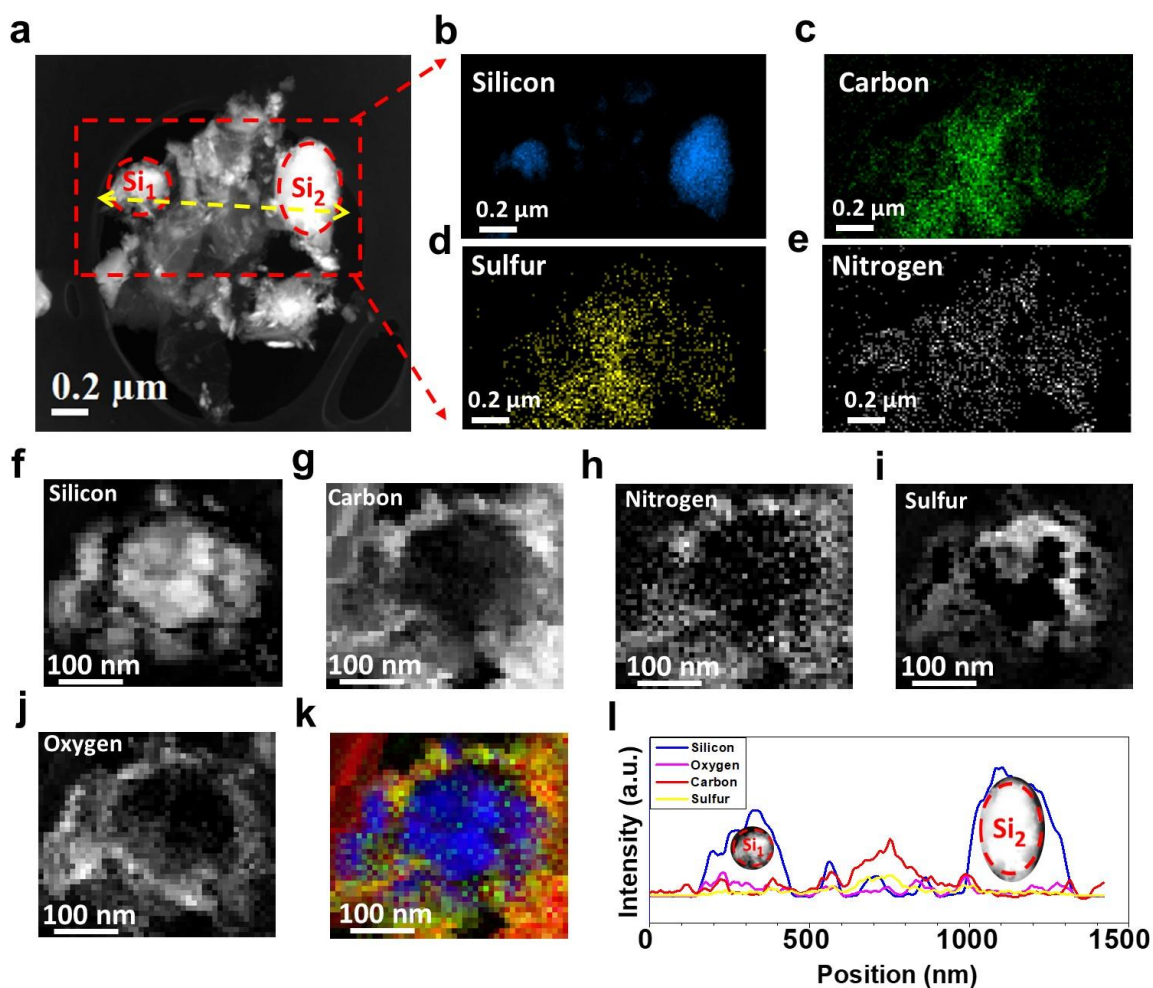
Figure 5-7 (a) HAADF-STEM image of SG-SiMPs-cPAN composite, (b-e) EDX map of selected area for silicon, carbon, sulfur, and nitrogen, (f-j) EELS map of region Si_1, (k) superimposed EELS color map of silicon (blue), carbon (red), nitrogen (green), (l) EELS line scan (yellow arrow in (a)) across two SG-SiMPs-cPAN particles.

86

The electrochemical performance of the fabricated SG-SiMPs-cPAN electrodes are summarized in **Figure 5-8**. Cyclic voltammetry is used to study the lithiation/delithiation behavior of electrodes (**Figure 5-8a**). During lithiation, two peaks are observed at 0.27 and 0.22 V due to the formation of $Li_{12}Si_7$ and $Li_{15}Si_4$ phases, respectively.[99] While delithiating the electrode, two anodic peaks appear at 0.32 and 0.50 V due to the conversion of Li_xSi to silicon. The peaks become progressively larger and broader with cycling as more material is activated by conversion of crystalline silicon into amorphous silicon.

Figure 5-8b demonstrates the galvanostatic voltage profile of the SG-SiMPs-cPAN electrodes tested at 0.1 A g^{-1} between 0.01 and 1.1 V. The discharge profile varies slightly after the first cycle from a typical long plateau to a curve with a gentle slope, which is attributed to the transformation of crystalline silicon into amorphous silicon in subsequent cycles. The first cycle specific discharge capacity of the SG-SiMPs-cPAN electrode is 4125 mAh g^{-1} with a columbic efficiency of 72.5 %. This low coulombic efficiency can be attributed to irreversible lithiation along with SEI formation. However, the coulombic efficiency increases to over 98 % within 5 cycles.

Electrochemical impedance spectroscopy (EIS) is also conducted to monitor the change of resistance of the electrodes. **Figure 5-8c** shows the Nyquist plots of the SG-SiMPs-cPAN electrode and a conventional electrode composed of SiMPs (60 wt%), Super P (20 wt%) and PVDF (20 wt%). Each plot consists of a semi-circle and a tail. The X-axis intercept at high frequency corresponds to the combined resistance (R_S) of the electrolyte, electrode and current collector; whereas the semi-circle diameter represents the combined resistance of charge-

transfer (R_{CT}) and SEI (R_{SEI}). The Nyquist plot shows that the charge transfer resistance of the SG-SiMPs-cPAN electrode is lower than that of the conventional electrode, implying improved electrical connectivity and conductivity of the SG-SiMPs-cPAN electrode. This is reasonable since the PVDF binder of the conventional electrode is electronically insulating, whereas cPAN (after thermolysis) forms an electrically conductive network within the electrode. Thus, cPAN acts both as a binder for mechanical integrity of the electrode and a conductive agent to facilitate charge transfer. Furthermore, the decrease in charge transfer resistance after 50 cycles shows the stability of SG-SiMPs-cPAN electrodes during cycling.

The structural stability of the electrodes is evaluated by testing the cells under various cycling rates. **Figure 5-8d** shows the cycling stability of the SG-SiMPs-cPAN electrode at 0.2 A g^{-1}. The initial discharge capacity of the electrodes stabilizes at ~ 3000 mAh g^{-1} at a rate of 0.1 A g^{-1} within 5 cycles. At a charging rate of 0.2 A g^{-1}, the capacity is 2730 mAh g^{-1} after 50 cycles. The SG-SiMPs-cPAN electrode preserves 91 % of its initial capacity, which may be attributed to the stability of the SEI on the negative electrode. This reveals that the electrode architecture can buffer the volume change and significantly alleviate electrolyte decomposition. This is mainly due to the robust carbon matrix of cPAN and SG sheets wrapping the silicon particles. For comparison, the conventional electrode is also tested under the same conditions, with its cycling stability shown in **Figure 5-8d**. The discharge capacity decays significantly after each cycle and very little remains after only 10 cycles. Upon disassembling the CE cell after testing, it was realized that battery failure resulted from electrode disintegration. This is likely because of the lower binding efficiency of PVDF, which caused active material rupture from the copper

88

current collector and catastrophic performance loss upon charging/discharging (**Figure 5-8i-2**). This highlights the superior electrode structure of SG-SiMPs-cPAN compared to that of the conventional electrode. To better evaluate the electrochemical performance of SG-SiMPs-cPAN electrodes, faster cycling rates were also applied. **Figure 5-8e** shows the cycling stability of SG-SiMPs-cPAN electrode at 1 A g^{-1} which also displays good cycling stability and a discharge capacity of 2256 mAh g^{-1} after 100 cycles. **Figure 5-8f-g** shows the rate capability of the SG-SiMPs-cPAN electrode. The capacity gradually decreased with an increase of cycling rate. Even at 4 A g^{-1} current density, a capacity above 2000 mAh g^{-1} is achieved, representing 70 % retention (**Figure 5-8g**). Moreover, stable cycling performance is attained when the rate is switched back to 2 A g^{-1}, as shown in **Figure 5-8h**. After 500 cycles, the cell has a discharge capacity higher than 1400 mAh g^{-1}. This implies that the electrode integrity is preserved without disintegration even at high rates, despite the fact that the silicon particles undergo rapid volume changes during cycling. To further confirm the structural integrity of the electrode, the cell is disassembled after cycling for characterization. **Figure 5-8i-1** shows that the electrode material of SG-SiMPs-cPAN is not ruptured from the copper foil after 500 cycles. On the contrary, the CE electrode materials have peeled away from the copper current collector and remain attached to the separator (**Figure 5-8i-2**). This further confirms that the silicon anodes prepared with conventional methods do not possess the desired electrode integrity.
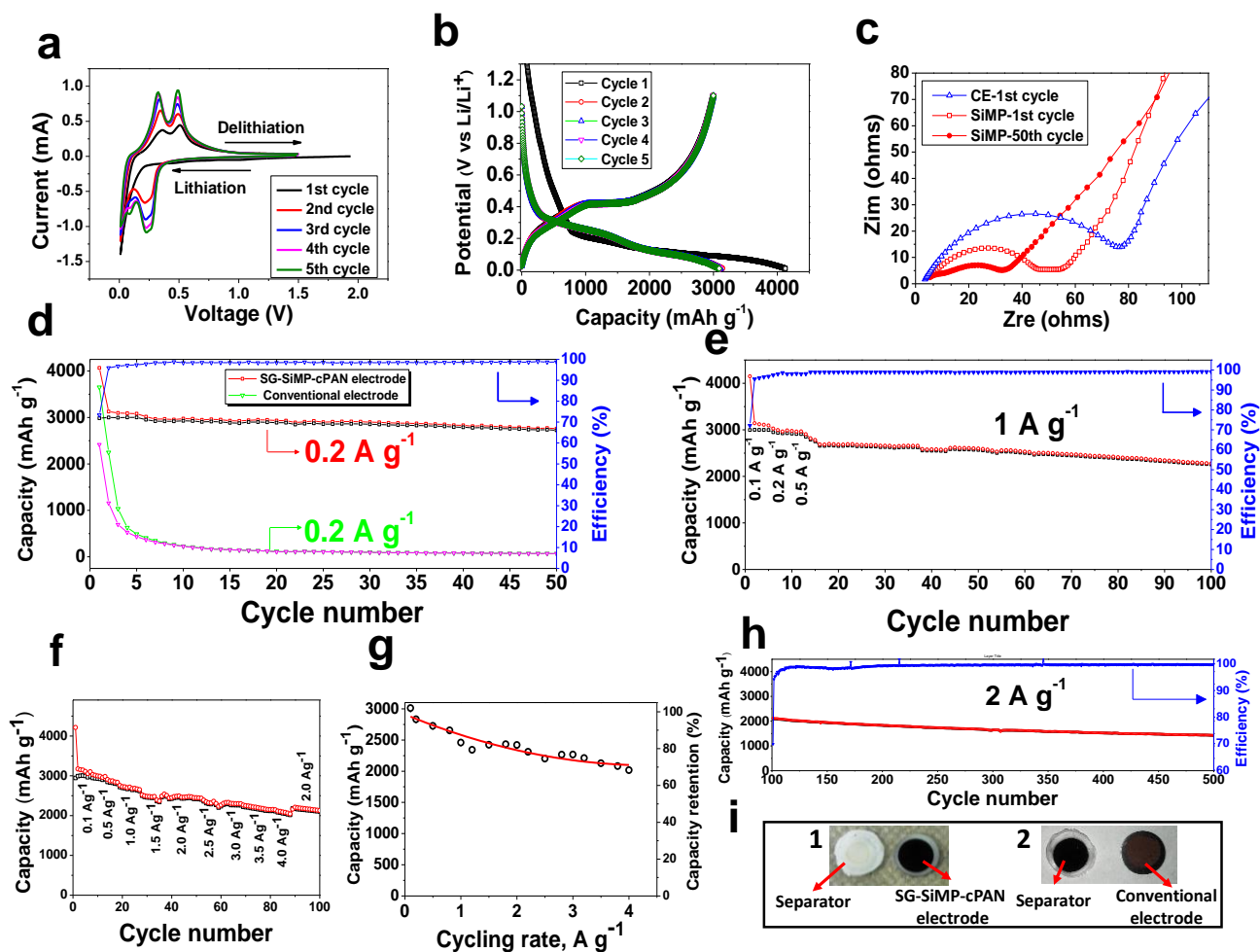
Figure 5-8 (a) Cyclic voltammograms of SG-SiMPs-cPAN electrode, (b) voltage-capacity profile of the SG-SiMPs-cPAN electrode at 0.1 A g^{-1}, (c) Nyquist plot of the SG-SiMPs-cPAN and CE electrodes after 1st and 50th cycles, (d) cycling stability of the SG-SiMPs-cPAN electrode and conventional electrode at 0.2 A g^{-1}, (e) cycling stability of the SG-SiMPs-cPAN electrode at 1 A g^{-1}, (f) rate capability of the SG-SiMPs-cPAN electrode from 0.1 A g^{-1} to 4 A g^{-1}, (g) capacity retention and specific capacity of the SG-SiMPs-cPAN electrode as a function

90

of cycling rate, (h) cycling stability of cell "f" from 100th cycle to 500 cycles at 2 A g^{-1}, (i) SG-SiMPs-cPAN electrode and conventional electrode after cycling and corresponding separators.

A deeper study of the electrode surface is essential to elucidate the mechanism underlying the improved cycling efficiency. Atomic force microscopy (AFM), SEM and TEM have been used to study the surface properties of the electrodes before and after cycling. Before thermolysis, the electrodes have a relatively smooth, continuous surface as shown in **Figure 5-9a** and **d**. In contrast, **Figure 5-9b** and **Figure 5-9e-f** clearly show that non-continuous micro-channels have formed at the SG-SiMPs-cPAN electrode surface after thermolysis due to the internal stress created with the shrinkage of PAN upon cyclization. Furthermore, following long cycling periods, **Figure 5-9c** and **g** show the formation of continuous micro-channels resembling mudcracking. A similar phenomenon was also observed by Dahn et al. in a study of silicon films.[64] We speculate that this morphology arises in a mode similar to mudcrack formation, whereby the delithiation process of the electrode during charge is analogous to dehydration of mud, resulting in shrinkage of silicon particles and crack propagation due to stress fracture. We hypothesize that the void volumes between the electrode "islands" can help to buffer the isotropic silicon volumetric changes during cycling and prevent electrode material rupture and leading to electrode level integrity and good cycling stability. In addition, TEM images (**Figure 5-9h-i**) and corresponding coloured EELS maps (**Figure 5-10)** for the electrode materials show that the silicon particles (bright regions) were distributed evenly and sandwiched between the sheets of NG and SG sheets after cycling, preventing the silicon particle isolation from the carbon matrix. This keeps the integrity at the particle level. Thus,

91

the synergistic effect preserving integrity at the particle and electrode level lead to good cycling stability.
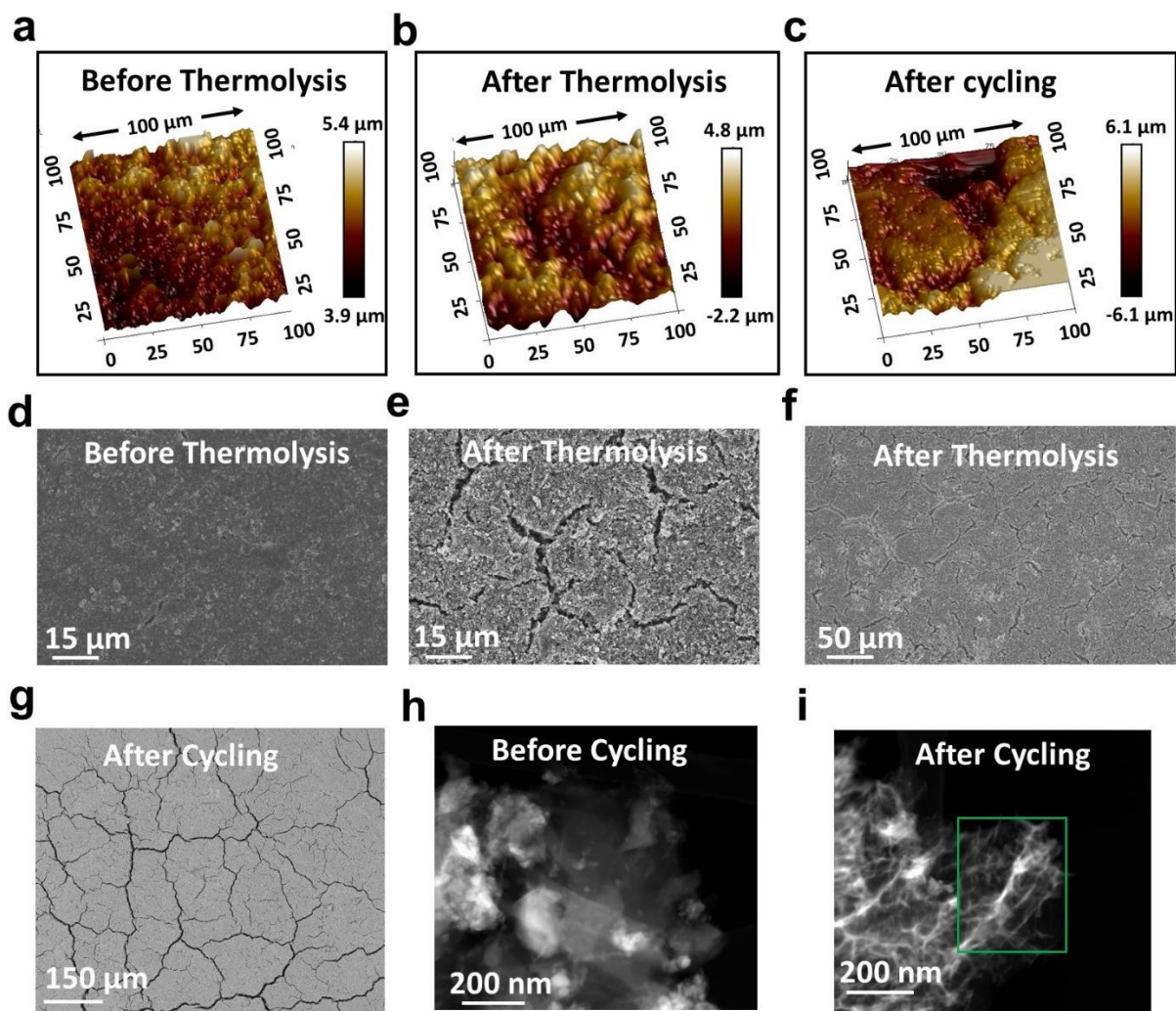
Figure 5-9 (a) AFM image of the SG-SiMPs-PAN electrode surface before thermolysis, (b) AFM image of the SG-SiMPs-cPAN electrode surface after thermolysis, (c) AFM image of the SG-SiMPs-cPAN electrode surface after cycling, (d) SEM image of the SG-SiMPs-PAN electrode surface before thermolysis, (e) SEM image of the SG-SiMPs-cPAN electrode surface after thermolysis, (f) SEM image of the SG-SiMPs-cPAN electrode surface after thermolysis,

(g) SEM image of the SG-SiMPs-cPAN electrode after cycling (back scattering imaging mode) , (h) HAADF-STEM image of the SG-SiMPs-cPAN electrode before cycling, (i) HAADF-STEM image of the SG-SiMPs-cPAN electrode after cycling.
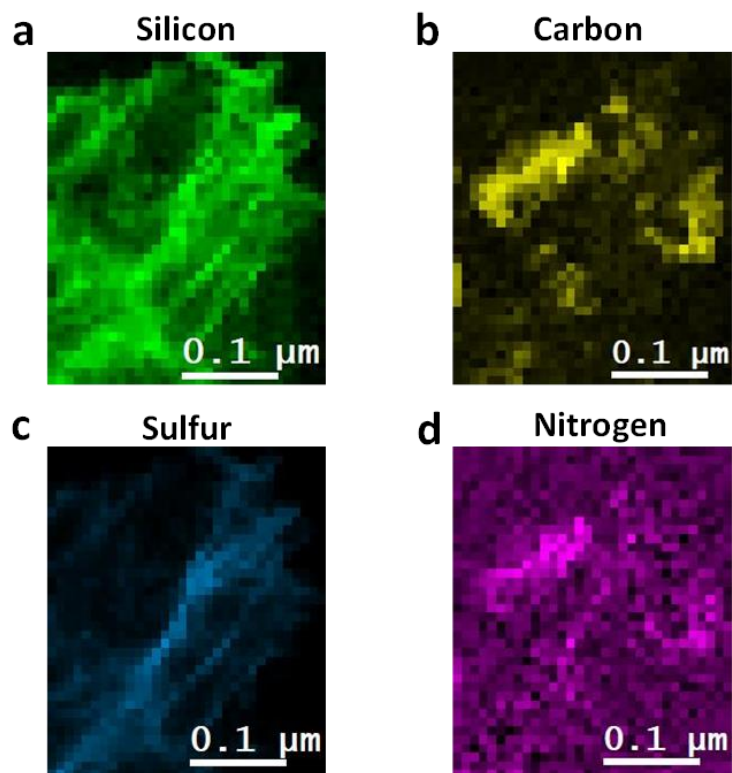
Figure 5-10 (a-d) The elements mapping by EELS for the area marked in Figure 5-9i.

5.4 Conclusion

In summary, we have fabricated a stable silicon-based anode using commercial SiMPs by developing a two-step top-down approach. Applying a fluid-induced fracture concept to SiMPs by milling them within an electrode precursor slurry led to nanostructuring of the silicon by a

straightforward and scalable process. After casting the electrode precursor slurry on the current collector, it was subjected to thermolysis to achieve an ideally tuned SG-SiMPs-cPAN electrode structure. In this structure, the polymer binder (PAN) was converted into a 3D conductive network of cPAN that wrapped the silicon particles and formed micron-sized channels throughout the electrode structure. These void micro-channels acted as a mechanical buffer for the anisotropic volume changes of silicon particles during battery charging/discharging, thereby preventing electrode pulverization. This electrode structure provided excellent capacity (3081 mAh g^{-1} at 0.1 A g^{-1}) in addition to good rate capabilities and cycle life (1423 mAh g^{-1} at 2 A g^{-1} for 500 cycles). Furthermore, the efficiency of this technique makes it possible to expand its application to other anode materials that require mechanical robustness and electrical conductivity with the goal of preparing next generation lithium-ion batteries.

Chapter 6

In-situ Binder Graphenization for the use of Metallurgical Silicon in Lithium-ion Batteries

6.1 Introduction

The development of high-energy density lithium-ion batteries is of intense interest to meet the requirements of emerging markets such as plug-in hybrid electric vehicles (PHEVs) and grid-scale energy storage systems. Research efforts have been made to replace the intercalation-based state-of-the-art graphite anode with alloying materials which can provide higher capacity due to a different lithium storage mechanism. Among these materials, silicon is a strong candidate as a next generation anode material due to its outstanding theoretical capacity (4200 mAh g^{-1}) compared to that of graphite (372 mAh g^{-1}). However, the significant volume change of silicon during battery cycling and the unstable solid electrolyte interface (SEI) leads to poor cyclability and loss of electrode integrity. Despite the success of anodes prepared from silicon nanoparticle-carbon composites to overcome these problems, their commercialization is not currently viable because of the complex and expensive preparation techniques such as chemical vapor deposition and/or template growth [36, 37, 67, 71, 104, 121, 122]. The utilization of metallurgical silicon (mSi) would move the rational design a considerable step closer due to their low cost and commercial abundance. The main challenges of mSi electrodes are cracking at the particle level and mechanical degradation at the electrode level[29, 39, 123]. To address these problems, previous researchers have attempted to etch metallurgical silicon particles (mSiPs) with

hydrogen fluoride (HF) to create buffer regions to accommodate the size change during cycling[43-45, 124-126]. However, the strong corrosive character of HF arises environmental concerns and pushed the research focus to new binder designs that prevent electrode level failure [46, 127]. Despite the success of these binders, their commercial non-availability makes it challenging to scale up the electrode fabrication.

In this chapter, polyacrylonitrile (PAN), which is a readily-available polymer, is chemically modified in-situ for use both as a binder and conductive agent. To do so, a one-pot electrode level thermal treatment is designed to synthesize partially graphenized PAN (gPAN) as a nitrogen-doped carbon sheet network that can maintain the structural integrity of electrode. This capitalizes on the encapsulation of the mSiPs by the gPAN framework. With this design, the original mSiPs can crack, but still can remain safely within the confines of the flexible graphene-like sheets. As a result, the electrode of gPAN/mSiPs shows good cycle stability and rate performance. The improved battery performance of this composite, along with the ease of its preparation makes this fabrication technique a good candidate to produce cost-effective high-performance silicon anodes for lithium-ion batteries.

6.2 Experimental Section

6.2.1 Preparation of Graphene Oxide (GO)

The reaction procedure to prepare GO from natural graphite flakes was adapted from the James Tour method.[72] A 9:1 mixture of concentrated H_2SO_4/H_3PO_4 (360:40 mL) was poured into a beaker containing 3 g graphite powder. The solution was mixed for 30 min in an ice bath before

adding 27 g of KMnO$_4$ and mixing for another 1 hour. The contents were then transferred to a hotplate and stirred at 50 ^{o}C. After the reaction was completed, 600 mL distilled water was added to the solution while it was being stirred in an ice bath. After the addition of water, 30 mL hydrogen peroxide (H$_2$O$_2$) was poured into the solution to reduce the unreacted KMnO$_4$. The final solution was washed several times with 5 % HCl solution and distilled water by centrifugation.

6.2.2 Electrode Fabrication and Coin Cell Assembly

The electrodes were fabricated via direct coating of gPAN/mSiPs slurry onto a copper foil using the Blade method. The gPAN/mSiPs slurry was prepared by mixing 60 wt% mSiPs, 38 wt% PAN, 2 wt% GO in dimethylformamide (DMF) using a magnetic stirrer and sonication. After coating the slurry to the copper foil, it was dried in a convection oven at 80 ^{o}C overnight. The foil was punched by a disc cutter to form circular working electrodes. The electrodes were then subjected to thermolysis at 450 ^{o}C in an argon atmosphere for 10 min, followed by cooling. The heating ramp during annealing was 7.5 ^{o}C min^{-1}.

Coin-type half cells were assembled in a glove box under argon atmosphere containing less than 0.5 ppm oxygen and water moisture. The electrolyte was LiPF$_6$ (1M) dissolved in 60 wt% dimethyl carbonate (DMC), 30 wt% ethylene carbonate (EC) and 10 wt% fluorinated ethylene carbonate (FEC). Lithium metal was used as the counter electrode. The electrodes were separated using a polypropylene separator (PP2075, Celgard). The battery performance was tested by galvanostatic charge/discharge cycling between cut-off voltages of 0.01 V and 1.1 V for discharge and charge, respectively using a BTS 3000 battery tester. Different current

densities were applied to investigate the rate capability. Finally, the coin cells were subjected to cyclic voltammetry between 1.5 V and 0.01 V at a rate of 0.05 mV s^{-1} using an electrochemical testing platform (Princeton Applied Research, VersaSTAT MC Potentiostat). Two conventional/reference cells were fabricated using 60 wt% SiMPs, 20 wt% conductive agent and 20 wt% binder and was tested under the same conditions as the gPAN/mSiPs cells. The conductive agent was SuperP and binders were polyacrylonitrile (PAN) and polyvinylidene fluoride (PVDF).

6.2.3 Material Characterization

The morphology and structure of the electrode materials were examined using scanning electron microscopy (SEM, LEO FESEM 1530) and transmission electron microscopy (TEM, JEOL 2010F TEM/STEM field emission microscope) equipped with a large solid angle for high X-ray throughput and a Gatan imaging filter (GIF) for energy-filtered imaging. Thermal analysis of samples was conducted by differential scanning calorimetry (DSC) and thermogravimetric analysis (TGA) in a TA model Q500. PAN was heated in a nitrogen atmosphere from 25 °C to 850 °C at a ramp rate of 10 °C min^{-1}. Raman spectra of PAN films were obtained using a Bruker Senterra with a laser wavelength of 532 nm. FTIR analysis was conducted with a PerkinElmer-283B FT-IR spectrometer. XRD analysis was done using monochromatic Cu K x-rays (154 nm wavelength) and an Inel XRG 3000 diffractometer.

6.3 Results and Discussion

Figure 6-1a provides the schematic of the electrode fabrication process. mSiPs (Sigma-Aldrich Co, 325 mesh) was mixed with PAN (M_W=150.000, Sigma-Aldrich Co) binder and graphene oxide (GO) in a 60:38:2 wt ratio in dimethylformamide solution (DMF) to form a homogenous solution under magnetic stirring and ultrasonication. The slurry was applied on a copper foil using Doctor Blade method and dried overnight at 80 °C. After the PAN/mSiPs electrodes were punched in circular discs, they were subjected to a controlled heat treatment (CHT) under argon atmosphere by heating gently in a quartz tube up to 450 °C and holding for 10 minutes, followed by cooling. This heat treatment tuned the structure of the PAN binder to form a nitrogen-doped graphene-like (NG) matrix throughout the electrode that could strongly adhere the mSiPs to the current collector. Ideally this would provide a flexible electron transport framework that also prevents the loss of active material during battery cycling. Furthermore, hopefully such a protective framework on the surface of mSiPs would also stabilize the SEI.
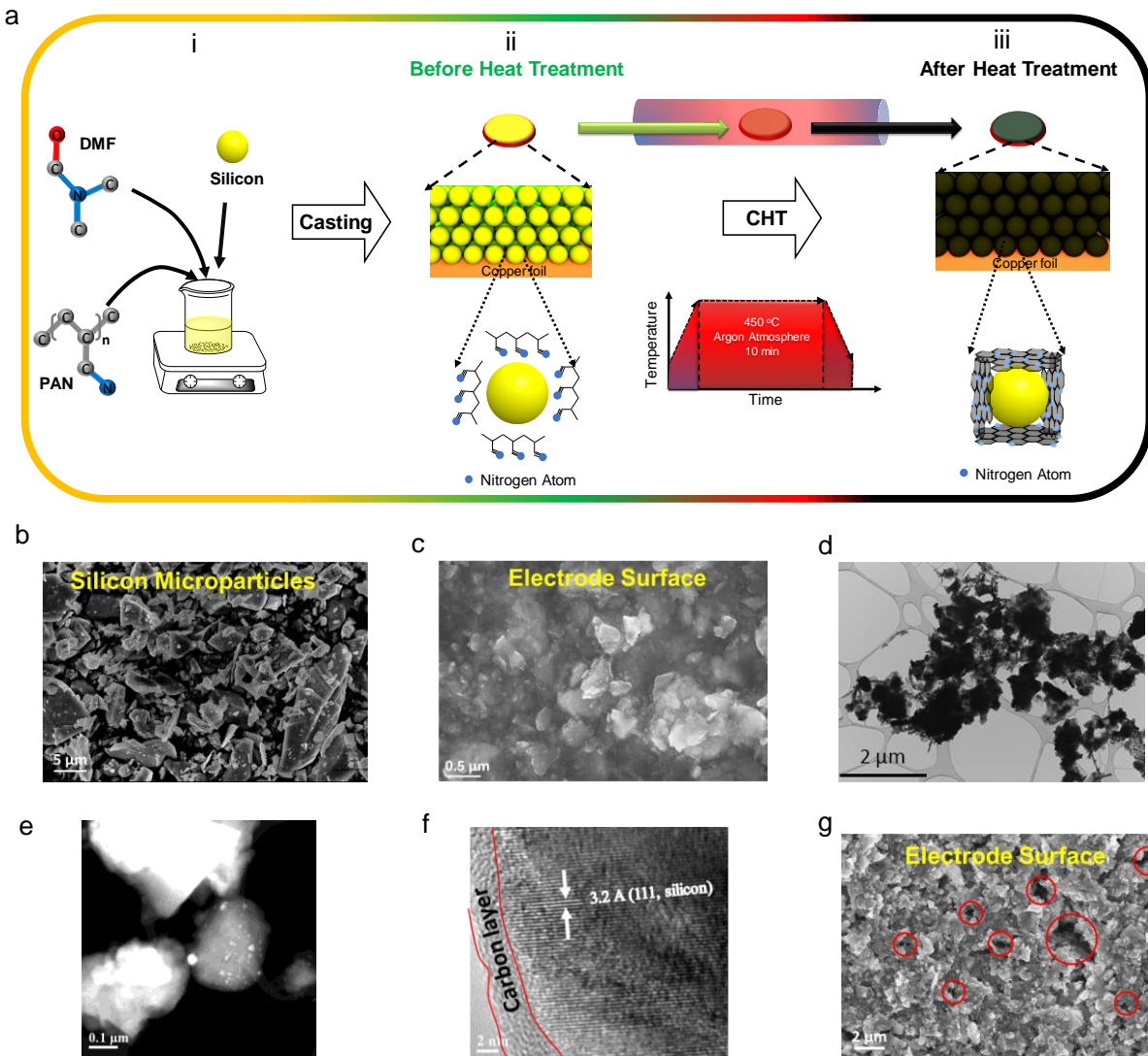
Figure 6-1 (a) Schematic of the electrode fabrication process: (i) mixing of the electrode materials; (ii) morphology of the electrode before CHT showing PAN chains wrapping the silicon particles; (iii) morphology of the electrode after CHT showing that gPAN wrap the silicon particles, (b) SEM image of mSiPs, (c) SEM image of the PAN/mSiPs electrode surface, (d) TEM image of gPAN/mSiPs composite after CHT, (e) HAADF-STEM image of gPAN/mSiPs composite after CHT, (f) HRTEM image of mSiPs with gPAN shell after CHT,

(g) SEM image of gPAN/mSiPs electrode surface showing the formation of channels on the electrode surface.

To observe the effect of CHT, the morphology of electrode was studied by scanning electron microscopy (SEM) and transmission electron microscopy (TEM). **Figure 6-1b** shows the SEM image of bare mSiPs. As seen, silicon particles are irregular in size and shape that can be sharp and angular. **Figure 6-1c** shows the surface morphology of the PAN/mSiPs electrode. The silicon particles appear to be embedded in a glassy medium of PAN which can act as both mechanical support and 3D electron pathway upon CHT. Energy-dispersive X-ray (EDX) analysis of the electrode surface confirmed the presence of silicon in carbon (C) and nitrogen (N) environment. TEM (**Figure 6-1d**) and HAADF-STEM (**Figure 6-1e**) images of the gPAN/mSiPs electrode material also verifies that mSiPs are hosted within gPAN environment. The high-resolution transmission electron microscopy (HRTEM) image presents the thin gPAN layer (~ 3 nm, **Figure 6-1f**) on the surface of silicon particles. Further structural elucidation of electrode material is discussed with **Figure 6-6**. The coarse surface structure of the electrode can be seen in **Figure 6-1g.** The pore formation is attributed to the stress created by the difference in thermal expansion coefficient of PAN and silicon. These pores can facilitate electrolyte infiltration to the bulk of the electrode which is crucial for charge transfer and lithium diffusion.

Figure 6-2a-b show the thermal characterization of PAN with differential scanning calorimetry (DSC) and thermal gravimetric analysis (TGA), respectively. DCS analysis of PAN shows a sharp exothermic peak at 300 °C which is typically attributed to the aromatization

of PAN chains via a free radical reaction of nitrile groups[128, 129]. The mass change during cyclization monitored by TGA reveals that the initial mass loss takes place at the same temperature as the exothermic DSC peak. Thus, the mass loss of gPAN/mSiPs electrodes after CHT can be associated with the cyclization of the PAN binder.

a)

b)
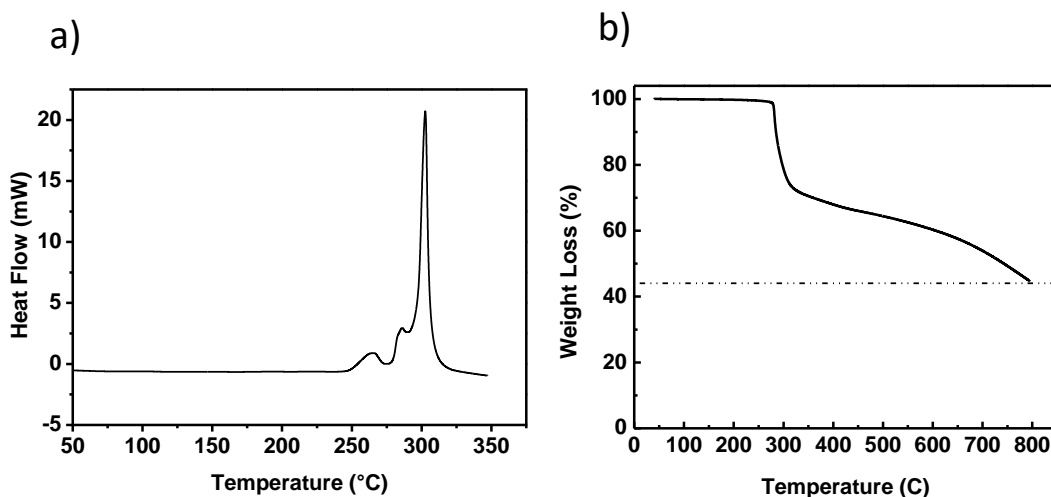
Figure 6-2 Thermal characterization of PAN by (a) DSC and (b) TGA.

The change in chemical structure of PAN after CHT has also been studied with Raman, Fourier-transform infrared spectroscopy (FTIR), X-ray photoelectron spectroscopy (XPS) and X-ray powder diffraction (XRD). **Figure 6-3a** shows the Raman spectra of gPAN after CHT. The annealed PAN exhibits typical D, G and 2D bands at ~ 1372, 1595 and 2760 cm^{-1}, respectively. The appearance of these three peaks are usually attributed to the graphenization [130]. Thus, this verifies the transformation of the 1D polymer backbone to the 2D graphene like structure. FTIR analysis (**Figure 6-3b**) of PAN has been conducted to monitor the evolution of the bonds present in the 1D polymer chains and 2D aromatic structure before and after CHT. Before the CHT, a peak at 2243 cm^{-1} attributed to C≡N stretching appears and shows the

presence of nitrile groups on the polymer backbone. The peaks at 1363, 1456 and 2935 cm^{-1} are characteristic of δ_{C-H} in CH, δ_{C-H} in CH$_2$ and ν_{C-H} in CH$_2$, respectively. After heat treatment, the C≡N peak disappears and C=C and C=N peaks appear, further confirming the conversion of 1D PAN chains into a nitrogen-doped graphene like structure (or 2D graphenized PAN) (**Figure 6-5d-1**, schematic of PAN graphenization).
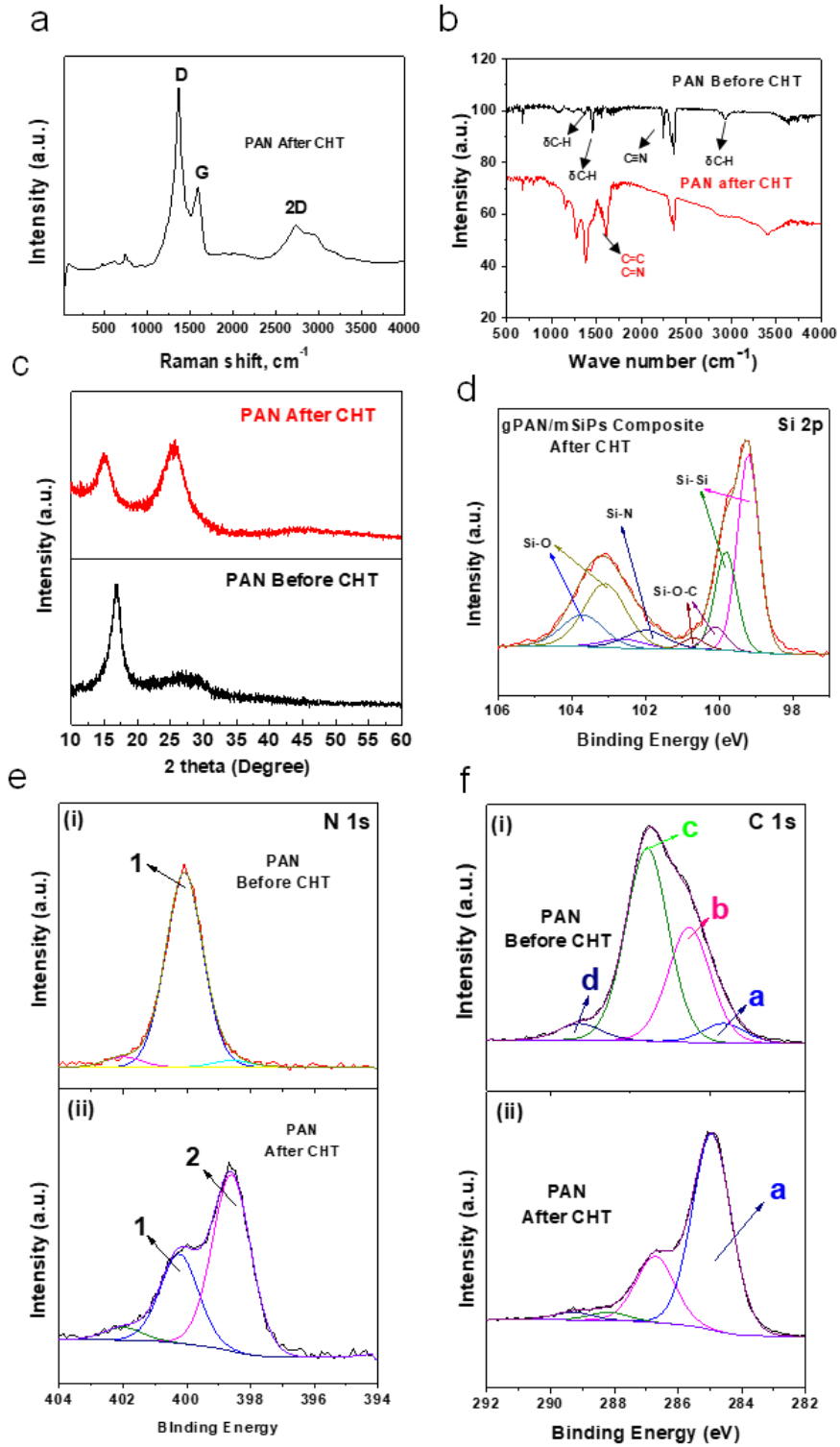
Figure 6-3 (a) Raman spectra of gPAN, (b) FTIR spectra of PAN before and after CHT, (c) XRD spectra of PAN before and after CHT, (d) high resolution XPS spectra of silicon in gPAN/mSiPs composite after CHT, (e) high resolution XPS spectra of nitrogen in gPAN/mSiPs composite before and after CHT, (f) high resolution XPS spectra of carbon in gPAN/mSiPs composite before and after CHT.

To further study the structural evolution of PAN and its interaction with the silicon surface, XPS has been conducted. **Figure 6-3e-f** present the N 1s and C 1s XPS spectra of PAN focusing on the chemical change of PAN with CHT. The high-resolution N 1s spectrum (**Figure 6-3e**) exhibits two main peaks at 400.1 eV (peak 1) and 398.6 eV (peak 2) which are attributed to nitrile (-C≡N) and pyridinic nitrogen (C-N=C). Before the heat treatment, only the nitrile group (1) is observed as no structural modification of the polymer backbone has occurred. After the heat treatment, the reduction of peak 1 and the appearance of peak 2 can be associated with the partial conversion of nitrile into pyridinic nitrogen during the graphenization of PAN. The XPS spectra of C 1s are also good agreement with the N 1s spectra with regard to the graphenization of PAN (**Figure 6-3f).** Prior to CHT, PAN exhibits four distinct peaks at 284.6 eV (a), 285.7 eV (b), 286.9 eV (c) and 289.1 eV (d). Peaks (a) and (b) are attributed to sp^2-bonded carbon (graphitic) and sp^3-hybridized carbon (diamond), respectively. Peaks (c) and (d) arise due to the presence of oxygenated carbon. After heat treatment, a significant increase in percentage of both graphitic carbon and pyridinic nitrogen accompanied with a decrease in nitrile species, again what is expected for the conversion into a graphene-like structure upon heat treatment. Furthermore, more interestingly, the interfacial

bonding of gPAN with the atoms on the surface of mSiPs is revealed by XPS analysis of the gPAN/mSiPs composite (**Figure 6-3d**).The Si 2p XPS spectrum reveals peaks at 99.2 and 99.8 eV (Si-Si), 100.1 and 100.7 eV (Si-O-C), 102 eV (Si-N-C) and 103.1 and 103.7 eV (SiO_x)[131, 132]. Si-N-C bonding can help to keep the fractured mSiPs in the gPAN network and thereby prevent the loss of active material and maintain the integrity of the gPAN/mSiPs electrode.

The XRD spectrum of PAN before annealing **(Figure 6-3c)** exhibits a peak at ~ 16.7º (100 crystallographic planes in PAN[133]) and a wide shoulder between 20º and 30º. After the heat treatment, a sharp peak corresponding to the (002) crystallographic plane appears at ~ 25.8º which is in good agreement with that observed in graphene [134]. This further corroborates the evolution of PAN to a graphene-like structure. Furthermore, XRD of the gPAN/mSiPs composite material shows that the silicon particles do not undergo any phase change or form silicon carbide after heat treatment implying that the silicon particles and gPAN are only physically blended with each other and maintain their respective chemical properties (**Figure 6-4**).
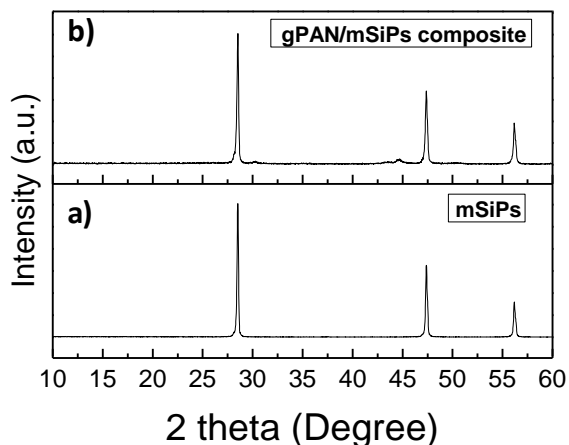
Figure 6-4 XRD spectra of (a) metallurgical silicon particles (mSiPs), (b) gPAN/mSiPs composite material.

Figure 6-5a shows the low magnification TEM image of the gPAN revealing its sheet-like nature. The HRTEM shows the multi-layer structure of the gPAN (**Figure 6-5b**) These chemical characterizations and TEM images of PAN demonstrate that PAN linear chains undergo chemical reaction as depicted in **Figure 6-5d-1** and wrap the silicon particles. Moreover, it is observed that the silicon particles are fractured into smaller pieces after thermal treatment (**Figure 6-5c**). We speculate that the post-annealing of electrodes may induce reduction in size of mSiPs. During CHT of the electrodes, PAN (M_W=150.000, Sigma-Aldrich Co) goes through a glass transition at ~ 85 °C which permits the polymer chains to move freely about each other and increase their volume. Assuming that the PAN chains adhere to the surface of brittle mSiPs, the pulling stress during polymer expansion may cause cracks to form on the silicon particles. The penetration of free moving polymer chains into these cracks can accelerate the fracture of particles, but still remained within the gPAN after the thermal

107

treatment of electrodes. This helped to increase structural integrity, avoid loss of active material and provide a fast-electrical pathway for mSiPs.
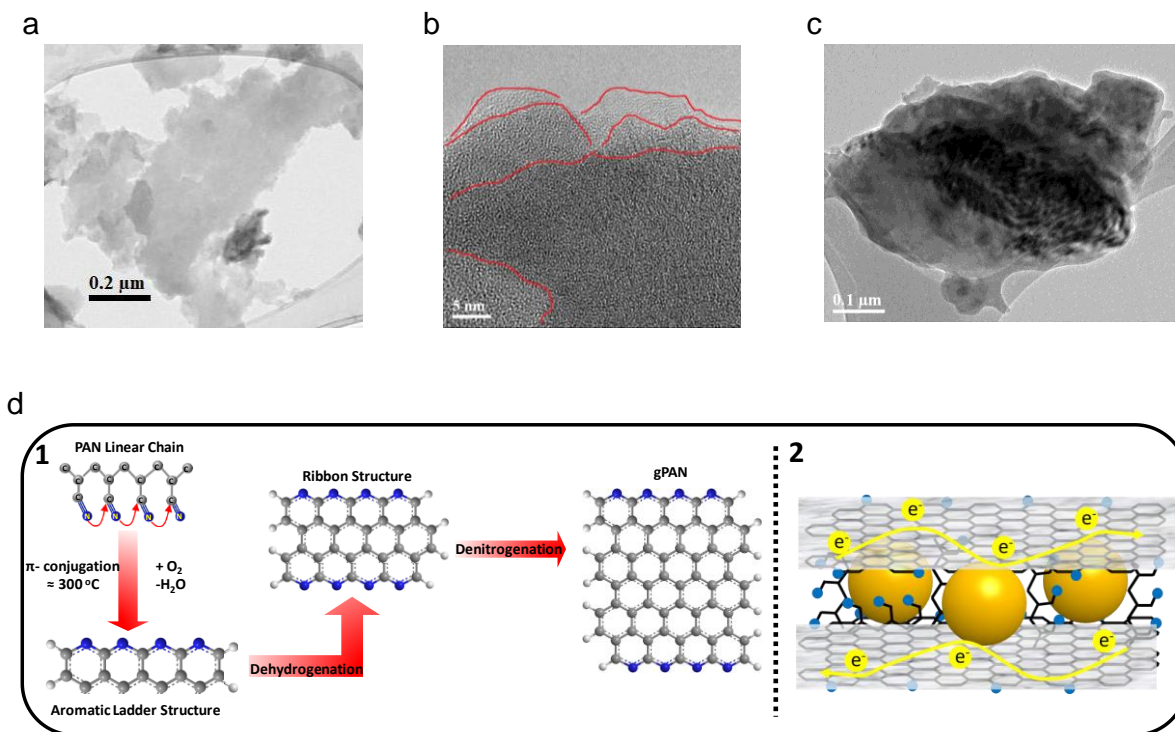
Figure 6-5 (a) TEM image of gPAN after CHT, (b) HRTEM image of gPAN after CHT (c) TEM image of a silicon particle encapsulated with gPAN showing the fracture formation after CHT, (d-1) schematics of the graphenization of PAN with CHT, (d-2) schematics of gPAN/mSiPs electrode material showing that mSiPs are encapsulated within gPAN.

Figure 6-6a shows a TEM image of gPAN/mSiPs composite material removed from the electrode by gently scratching and sonicating in ethanol. Electron energy-loss spectroscopy (EELS) mapping of the surface of silicon particles reveals that the silicon particles are wrapped by carbon (C), nitrogen (N) and oxygen (O) atoms. The carbon and nitrogen atoms stem from

the nitrogen-doped graphene attained from PAN and the oxygen atoms are due to the thin silicon oxide layer surrounding the mSiPs. The overlayed elemental map clearly shows the presence of a nitrogen cage surrounding the silicon particle. Furthermore, since the carbon signal is strongest at the edge of the particle, it confirms that the mSiPs have been successfully encapsulated.
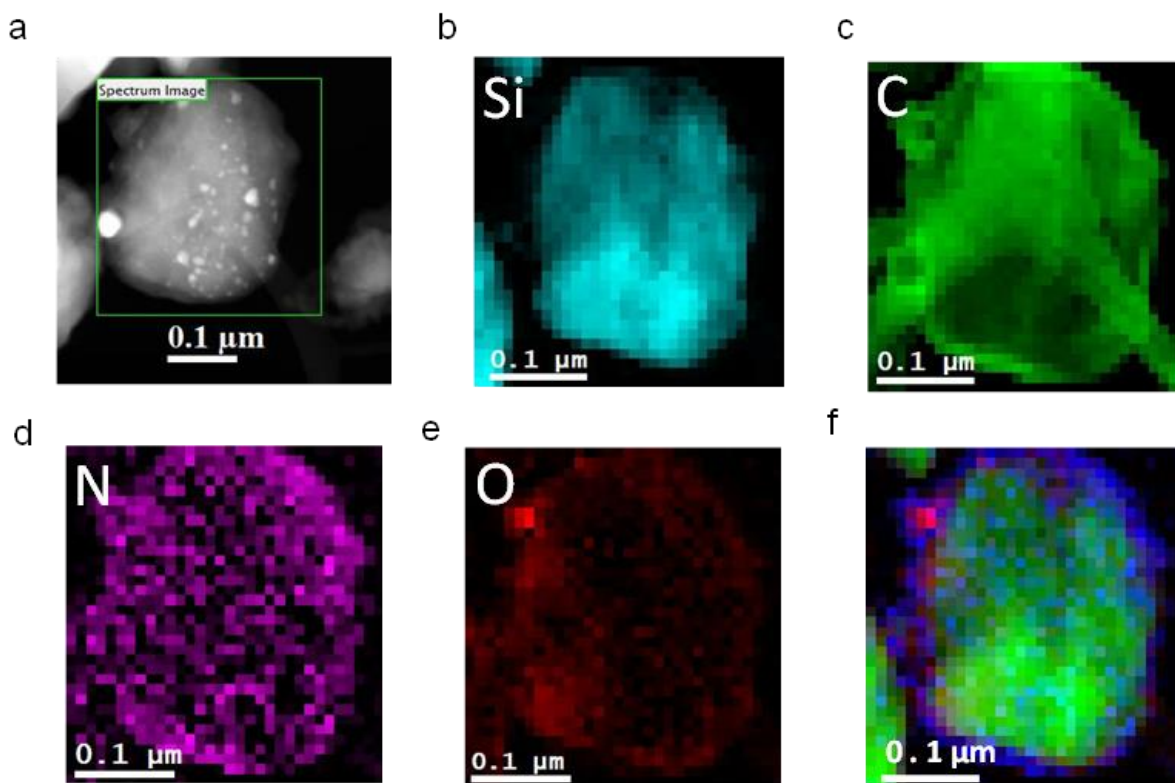
Figure 6-6 (a) HAADF-STEM image of gPAN/mSiPs composite material, (b-e) the EELS mapping of the gPAN/mSiPs composite material marked at (a), (f) superimposed EELS color map of silicon (green), nitrogen (blue) and oxygen (red).

Figure 6-7a presents the cyclic voltammogram conducted on the gPAN/mSiPs electrode. During the cathodic scan, a peak was observed at 0.14 V which is attributed to the formation

of lithiated silicon (Li_xSi). This peak is only observed after the second cycle which reveals the transformation from crystalline silicon to amorphous silicon. In the anodic direction, two peaks located at 0.35 and 0.51 V appear due to the delithiation of Li_xSi. With cycling, the anodic and cathodic peaks become broader and larger due to the activation of more silicon particles. Furthermore, the peak positions remain almost unchanged indicating the reversible character of lithiation and delithiation processes.

Figure 6-7b represents the galvanostatic cycling profile of the gPAN/mSiPs electrode at a current density of 0.1 A g^{-1} between 0.01 and 1.1 V. A typical long lithiation plateau is observed during the first cycle which can be attributed to the transformation of crystalline silicon to amorphous silicon. With subsequent cycles, a gentle slope is observed due to the lithiation of amorphous silicon formed during the first cycle. The electrode delivers an initial specific discharge capacity of 2644 mAh g^{-1} (1.0 mAh cm^{-2}) with a relatively high coulombic efficiency of 80.6 %. Within 3 cycles, the efficiency has boosted to 99.3 % and shows a good cycling stability with a discharge capacity of 1548 mAh g^{-1} (0.62 mAh cm^{-2}) after 85 cycles at 0.2 A g^{-1}. Two conventional cells of mSiPs-SuperP-PVDF and mSiPs-SuperP-PAN have been fabricated for comparison with gPAN/mSiPs cell. They exhibit very low first cycle efficiencies of 49.6 % and 14.7 % and quickly fail after 10 cycles. This shows the superior electrode architecture of gPAN/mSiPs. The graphenized structure of PAN sandwiches the mSiPs and provides a 3D flexible conductive network within the electrode. Although the mSiPs are fractured into smaller pieces with cycling, we speculate that they were kept within the electrode structure by this conductive network (**Figure 6-8a**). This maintains the electrode integrity,

prevents material loss and leads to the formation of a stable solid electrolyte interface (SEI) on the gPAN/mSiPs composite. However, in the conventional cells, silicon particles grow larger during lithiation and then fractures, leading to the loss of contact between SuperP and mSiPs. This is due to the weak binding properties of conventional binders. This leads two detrimental phenomena of reduced electrical conductivity and continuous growth of SEI (**Figure 6-8b**). This causes loss of electrolyte and hinders lithium diffusion. To see the effect of loading on cycle stability the silicon loading increased up to 0.93 mg cm^{-2} and the areal capacity increased up to 3.0 mAh cm^{-2} at 0.1 mA g^{-1} and provided 70 cycles and the capacity gradually decreased to 1.5 mAh cm^{-2} at 2.0 mA g^{-1} (**Figure 6-7e**). However, for such high loadings for metallurgical silicon to get high number of cycles is very challenging due to enormous volume change in silicon particles and the formation of huge stress within the electrode. Thus, we tested the cycling stability at a moderate mSiPs loading of 0.5 mg cm^{-2}. **Figure 6-7f** shows the cycling stability of gPAN/mSiPs at different rates from 0.1 A g^{-1} to 4 A g^{-1}. Even at a high 4 A g^{-1}, our material was able to deliver about 1200 mAh g^{-1}. After 250 cycles the capacity was around 1030 mAh g^{-1} (0.5 mAh cm^{-2}).
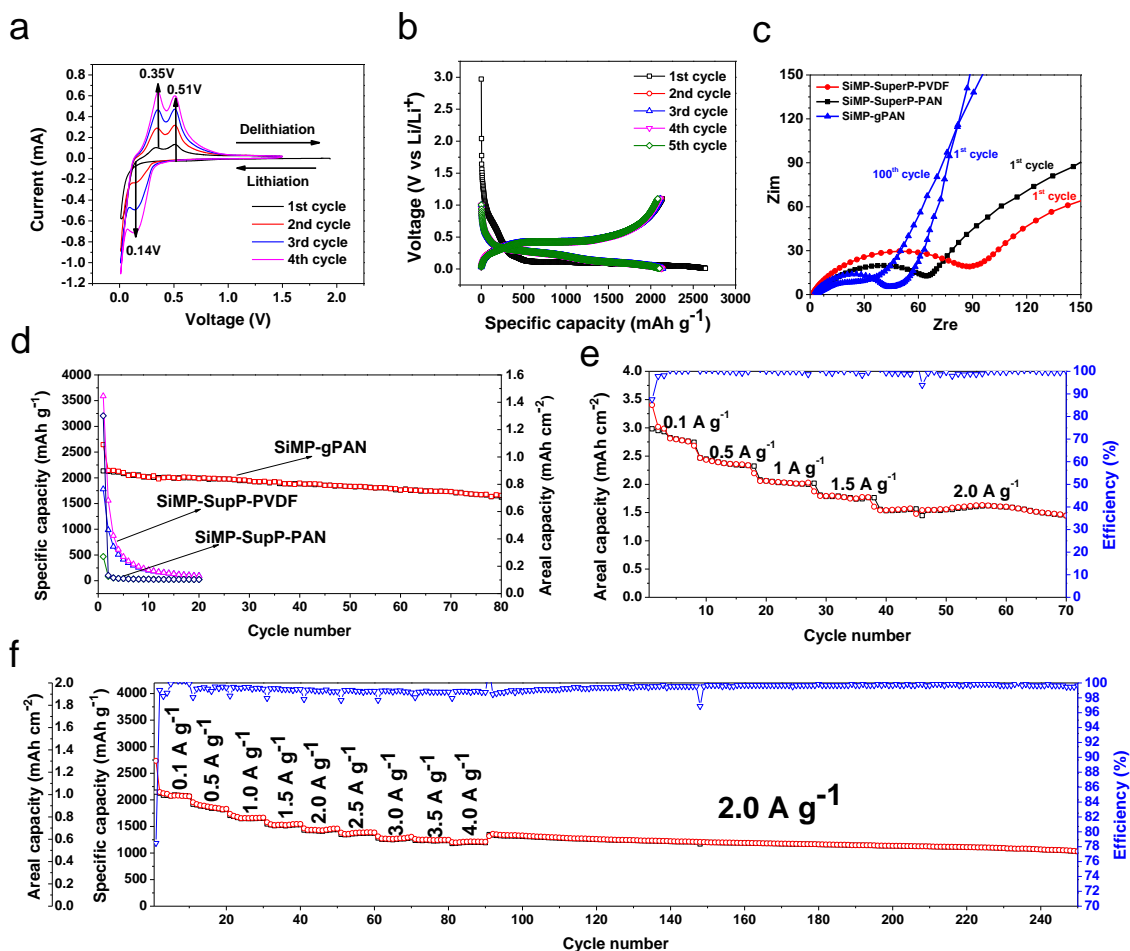
Figure 6-7 (a) Cyclic voltammograms of gPAN/mSiPs electrode, (b) voltage profile of gPAN/mSiPs electrode at 0.1 A g^{-1}, (c) Nyquist plot of gPAN/mSiPs, mSiPs/SuperP/PAN and mSiPS/SuperP/PVDF electrodes, (d) cycle stability of gPAN/mSiPs electrode (0.93 mg mSiPs cm^{-2}) at 0.2 A g^{-1}, (e) rate capability of the gPAN/mSiPs electrode from 0.1 A g^{-1} to 2.0 A g^{-1}, (f) rate capability (from 0.1 A g^{-1} to 4.0 A g^{-1}) and cycle stability (at 2.0 A g^{-1}) of gPAN/mSiPs electrode (0.5 mg mSiPs cm^{-2}).

Figure 6-7c shows the Nyquist plots of gPAN/mSiPs, mSiPs-SuperP-PAN and mSiPs-SuperP-PVDF electrodes. Each plot consists of a semi-circle and a tail representing resistance of charge-transfer and lithium-ion diffusion within the bulk electrode, respectively. The Nyquist plot shows that the charge transfer resistance of gPAN/mSiPs electrode is lower than that of control electrodes, implying improved electrical conductivity. This is reasonable due to the fact that the binders which represents 20 wt % of the electrode materials in the control electrodes (PVDF and PAN) are electronically insulating and thus not contributing to the conductivity. Furthermore, the binders loosely connect SuperP (conductive agent), mSiPs and current collector compared to the gPAN which forms a 3D electrically conductive network around the mSiPs and the current collector surface to facilitate electron transfer within the electrode. Thus, gPAN acts both as a binder for mechanical integrity of the electrode and as a conductive agent to facilitate charge transfer. The decrease in charge transfer resistance after 100 cycles shows evidence for the formation of a stable SEI layer around the gPAN/mSiPs electrode material during cycling (**Figure 6-8a**). This results in intact structural integrity and long cycling.
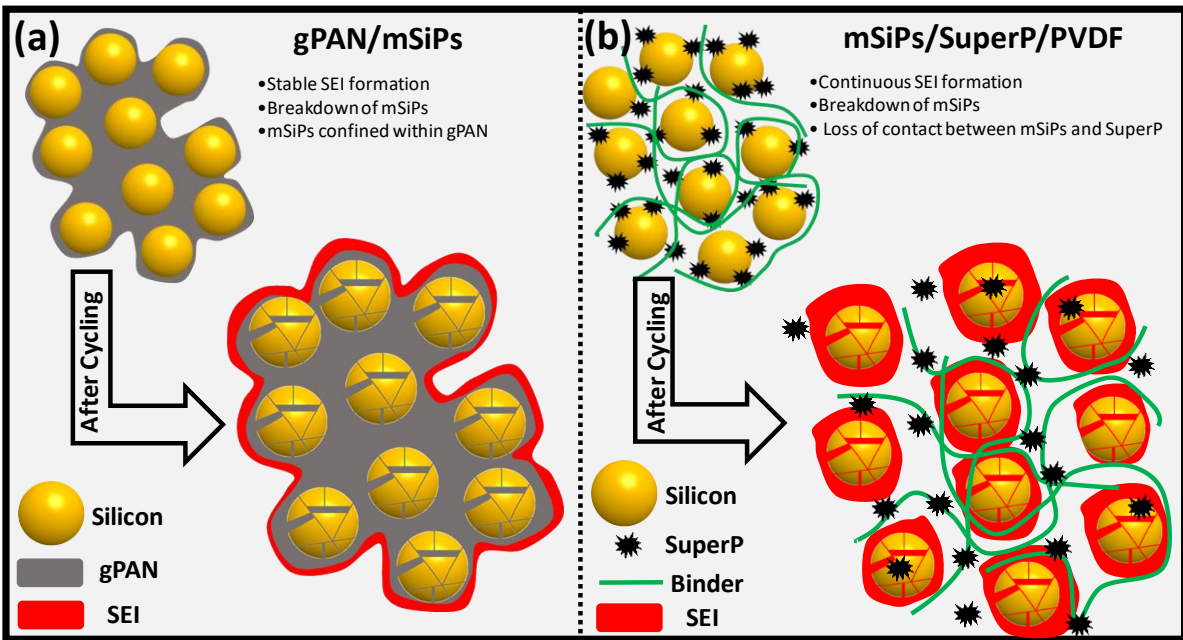
Figure 6-8 Schematics of electrode material morphologies of (a) gPAN/mSiPs and (b) mSiPs/SuperP/PVDF after cycling.

6.4 Conclusions

In conclusion, we have formulated a facile and scalable method capitalizing on the in-situ binder graphenization of the binder to host mSiPs and form a 3D robust electrode architecture. The gPAN served as an electron pathway with its π-conjugated network and provided pores on the electrode surface for good ionic conductivity. This leads to the formation of a good cycling and rate performance. Our approach is easy to scale up due to the commercial availability of PAN, compatibility with industrial slurry fabrication technique and should be adaptable to other electrode materials.

Chapter 7

Conclusions and Future Work

7.1 Conclusions

This thesis focuses on tackling the technological problems of silicon anodes such as poor cycle life and low-rate capability which hinder the commercialization of silicon for high energy density lithium-ion batteries. Thus, the main objectives of the present thesis include:

•   Enhancement of the electronic conductivity of silicon particles,

•   Formation of stable electrolyte interphase,

•   Prevention of electrode structure failure.

The progressive approaches developed in this thesis helped to realize these objectives by performing studies on carbonaceous silicon host materials and post-thermal treatment of the electrodes. The synergistic effect of this approach helped to improve the electronic conductivity, form a stable solid electrolyte interphase and design a flexible electrode architecture to maintain the electrode integrity.

In Chapter 4, we developed an advanced negative electrode relying on commercially available Si nanoparticles (SiNPs). The carbon support used in this study was sulfur-doped graphene (SG) which was prepared from graphene oxide. After preparing the electrodes by mixing these two components, they were subjected to heat treatment to tune the chemical structure of the polyacrylonitrile binder. We proposed that the covalent interaction between SiNPs and SG led to the physiochemical alteration of the electrode structure during cycling. This hierarchical structure (SiNPs/SG/cPAN) stabilized the solid electrolyte interphase leading to superior

115

reversible capacity of over 1,000 mAh g^{-1} for 2,275 cycles at 2.0 A g^{-1}. Furthermore, the nanoarchitectured design is believed to lower the contact of the electrolyte to the electrode, leading not only to a high coulombic efficiency of 99.9% but also to high stability even at a high capacity of 3.4 mAh cm^{-2}. The simple, scalable and non-hazardous approach provides new avenues for engineering electrode structures for enhanced performance.

While excellent rate capability has been achieved through the use of commercially available silicon nanoparticles, it still can not be commercialized due to the high cost. To address this challenge, a low-cost methodology of wet ball-milling is used in Chapter 5, for accelerated nanoscaling of commercial micron-sized silicon and an electrode level thermolysis process is applied to cyclize polyacrylonitrile (cPAN) binder to form a 3D conductive anode matrix with micro-channels. This engineered matrix sandwiches the silicon particles leading to an electrode structure with excellent mechanical robustness which can accommodate the large volumetric changes occurring during battery charging and discharging. It was shown to deliver an excellent capacity of 3081 mAh g^{-1} at 0.1 A g^{-1} and good cycle life (1423 mAh g^{-1} at 2.0 A g^{-1} after 500 cycles). Furthermore, the simplicity and scalability of this approach provides a promising path forward for the commercialization of next generation Li-ion batteries based on high capacity silicon anodes.

In Chapter 6, we established a more facile and scalable method by removing sulfur-doped graphene from the electrode recipe presented in Chapter 6, avoiding ball-milling and using metallurgical silicon as anode material. This capitalized on an in-situ binder graphenization approach to host metallurgical silicon particles (mSiPs) within gPAN and forms a 3D robust

electrode architecture. The gPAN served as an electron pathway with its π-conjugated network and provided openings on the electrode surface for electrolyte penetration to guarantee good ionic conductivity. Thus, we obtained an areal capacity of 3.0 mAh cm^{-2} at 0.1 A g^{-1} and more than 1.5 mAh cm^{-2} at 2.0 A g^{-1} for high loading electrodes. For moderate loadings, 1030 mAh g^{-1} (0.5 mAh cm^{-2}) is achieved after 250 cycles at 2.0 A g^{-1}. Our approach is easy to scale up due to the commercial availability of PAN and metallurgical silicon, compatibility with industrial slurry fabrication technique and adaptability to other electrode materials.

7.2 Future Work

Based on the results from the studies conducted in this research, future projects being planned to leverage the progress of fabricating cost-effective negative anodes from commercially available materials. Thus, metallurgical silicon will be used as the anode material. To address the challenge of using micron-size silicon, the focus of the study will be on the following topics:

- blending polyacrylonitrile with other commercially available polymers and carbon additives,

- modifying the annealing conditions of electrodes (temperature and atmosphere) to further investigate binder carbonization and the interaction with the silicon particles.

7.2.1 Blending PAN with Other Commercially Available Polymers

Recent research studies have shown that using water-soluble binders such as carboxymethyl cellulose (CMC) [135], polyacrylic acid (PAA)[33], alginate[32] and chitosan[136] achieved better

117

results than the PVDF binder and improved the electrochemical performance of Si-based anode materials in lithium-ion batteries. Furthermore, it was demonstrated that a binder mixture of CMC and PAA can be thermally cured to create a three-dimensionally interconnected matrix[137]. This capitalizes on the crosslinking of binders via condensation reaction of hydroxyl groups (-OH) of PAA and carboxymethyl groups (-COOH) of CMC. Since the thermal treatment of silicon electrodes was one of the main focus of this thesis, PAN can be blended with these curable binary binder mixtures to study the effect of thermal treatment on battery performance.

7.2.2 Carbon Additives

Reduced graphene-oxide (GO) and sulfur-doped graphene (SG) were used as additives in this thesis to boost the battery performance. First, they enhanced the conductivity of the electrode due to their aromatic structure. Furthermore, they helped to maintain the integrity of the electrode and prevented the agglomeration of silicon particles. This was attributed to the covalent interaction between hetero-atoms (sulfur and nitrogen) in the carbon scaffold and the silicon particles. However, adapting this method for large scale production may not be favored in this stage due to the current cost of SG. Thus, investigating the effect of other additives such as carbon nanotubes (CNT) and carbon nanofibers (CNF) on battery performance should be further studied.

7.2.3 Post-Treatment Method

Maintenance of the integrity and the conductivity of a silicon electrode upon volume expansion is a critical point for achieving a decent cycle life. To do so, we annealed the freshly prepared electrodes under an argon atmosphere at 450 °C in a tubular furnace. To make this post-treatment method more feasible and to study its effect on binder carbonization, modifications to the heating regime and the annealing atmosphere can be further explored.

Bibliography

1.   Winter, M.; Brodd, R. J. *Chemical reviews* **2004,** 104, (10), 4245-4270.
2.   Tarascon, J.-M.; Armand, M. *Nature* **2001,** 414, (6861), 359-367.
3.   Miyazaki, K. In *Release pattern of combined water of Manganese dioxide under vacuo-heated condition*, Proc. Manganese Dioxide Symp, 1975; pp 111-131.
4.   Whittingham, M. S. *Science* **1976,** 192, (4244), 1126-1127.
5.   Rao, B.; Francis, R.; Christopher, H. *J. Electrochem. Soc.* **1977,** 124, (10), 1490-1492.
6.   Murphy, D.; Di Salvo, F.; Carides, J.; Waszczak, J. *Materials Research Bulletin* **1978,** 13, (12), 1395-1402.
7.   Lazzari, M.; Scrosati, B. *J. Electrochem. Soc.* **1980,** 127, (3), 773-774.
8.   Mizushima, K.; Jones, P.; Wiseman, P.; Goodenough, J. *Materials Research Bulletin* **1980,** 15, (6), 783-789.
9.   Thackeray, M.; David, W.; Bruce, P.; Goodenough, J. *Materials Research Bulletin* **1983,** 18, (4), 461-472.
10.   Basu, S.; Zeller, C.; Flanders, P.; Fuerst, C.; Johnson, W.; Fischer, J. *Materials Science and Engineering* **1979,** 38, (3), 275-283.
11.   Zanini, M.; Basu, S.; Fischer, J. *Carbon* **1978,** 16, (3), 211-212.
12.   Yazami, R.; Touzain, P. *J. Power Sources* **1983,** 9, (3), 365-371.
13.   Yuan, X.; Liu, H.; Zhang, J., *Lithium-ion batteries: advanced materials and technologies*. CRC Press: 2011.
14.   Sigala, C.; Guyomard, D.; Verbaere, A.; Piffard, Y.; Tournoux, M. *Solid State Ionics* **1995,** 81, (3), 167-170.
15.   Arillo, M.; Cuello, G.; López, M.; Martin, P.; Pico, C.; Veiga, M. *Solid state sciences* **2005,** 7, (1), 25-32.
16.   Fang, H.; Wang, Z.; Zhang, B.; Li, X.; Li, G. *Electrochemistry communications* **2007,** 9, (5), 1077-1082.
17.   Yang, S.; Zavalij, P. Y.; Whittingham, M. S. *Electrochemistry Communications* **2001,** 3, (9), 505-508.
18.   Malik, R.; Burch, D.; Bazant, M.; Ceder, G. *Nano Lett.* **2010,** 10, (10), 4123-4127.
19.   Inaba, M., SECONDARY BATTERIES – LITHIUM RECHARGEABLE SYSTEMS – LITHIUM-ION | Negative Electrodes: Graphite. In *Encyclopedia of Electrochemical Power Sources*, Garche, J., Ed. Elsevier: Amsterdam, 2009; pp 198-208.
20.   Park, J.-K., *Principles and applications of lithium secondary batteries*. John Wiley & Sons: 2012.
21.   Larcher, D.; Beattie, S.; Morcrette, M.; Edstroem, K.; Jumas, J.-C.; Tarascon, J.-M. *Journal of Materials Chemistry* **2007,** 17, (36), 3759-3772.
22.   Ma, D.; Cao, Z.; Hu, A. *Nano-Micro Letters* **2014,** 6, (4), 347-358.
23.   Su, X.; Wu, Q.; Li, J.; Xiao, X.; Lott, A.; Lu, W.; Sheldon, B. W.; Wu, J. *Adv. Energy Mater.* **2014,** 4, (1), n/a-n/a.

24.	Lee, S. W.; McDowell, M. T.; Berla, L. A.; Nix, W. D.; Cui, Y. *Proceedings of the National Academy of Sciences* **2012,** 109, (11), 4080-4085.

25.	Liu, X. H.; Zhong, L.; Huang, S.; Mao, S. X.; Zhu, T.; Huang, J. Y. *Acs Nano* **2012,** 6, (2), 1522-1531.

26.	Hassan, F. M.; Batmaz, R.; Li, J.; Wang, X.; Xiao, X.; Yu, A.; Chen, Z. *Nat. Commun.* **2015,** 6.

27.	Liu, N.; Lu, Z. D.; Zhao, J.; McDowell, M. T.; Lee, H. W.; Zhao, W. T.; Cui, Y. *Nat. Nanotechnol.* **2014,** 9, (3), 187-192.

28.	Wu, H.; Yu, G.; Pan, L.; Liu, N.; McDowell, M. T.; Bao, Z.; Cui, Y. *Nat. Commun.* **2013,** 4, 1943.

29.	Sun, Y.; Liu, N.; Cui, Y. *Nat. Energy* **2016,** 1, 16071.

30.	Luo, L.; Xu, Y.; Zhang, H.; Han, X.; Dong, H.; Xu, X.; Chen, C.; Zhang, Y.; Lin, J. *ACS applied materials & interfaces* **2016,** 8, (12), 8154-8161.

31.	Mazouzi, D.; Lestriez, B.; Roue, L.; Guyomard, D. *Electrochem. Solid-State Lett.* **2009,** 12, (11), A215-A218.

32.	Kovalenko, I.; Zdyrko, B.; Magasinski, A.; Hertzberg, B.; Milicev, Z.; Burtovyy, R.; Luzinov, I.; Yushin, G. *Science* **2011,** 334, (6052), 75-79.

33.	Magasinski, A.; Zdyrko, B.; Kovalenko, I.; Hertzberg, B.; Burtovyy, R.; Huebner, C. F.; Fuller, T. F.; Luzinov, I.; Yushin, G. *ACS applied materials & interfaces* **2010,** 2, (11), 3004-3010.

34.	Shi, F.; Song, Z.; Ross, P. N.; Somorjai, G. A.; Ritchie, R. O.; Komvopoulos, K. *Nat. Commun.* **2016,** 7, 11886.

35.	Aurbach, D. *J. Power Sources* **2000,** 89, (2), 206-218.

36.	Wu, H.; Zheng, G.; Liu, N.; Carney, T. J.; Yang, Y.; Cui, Y. *Nano Lett.* **2012,** 12, (2), 904-909.

37.	Liu, N.; Wu, H.; McDowell, M. T.; Yao, Y.; Wang, C.; Cui, Y. *Nano Lett.* **2012,** 12, (6), 3315-3321.

38.	Wu, H.; Chan, G.; Choi, J. W.; Ryu, I.; Yao, Y.; McDowell, M. T.; Lee, S. W.; Jackson, A.; Yang, Y.; Hu, L.; Cui, Y. *Nat. Nanotechnol.* **2012,** 7, (5), 310-315.

39.	Kasavajjula, U.; Wang, C.; Appleby, A. J. *J. Power Sources* **2007,** 163, (2), 1003-1039.

40.	Obrovac, M.; Krause, L. *J. Electrochem. Soc.* **2007,** 154, (2), A103-A108.

41.	Ryu, J. H.; Kim, J. W.; Sung, Y.-E.; Oh, S. M. *Electrochem. Solid-State Lett.* **2004,** 7, (10), A306-A309.

42.	Yi, R.; Dai, F.; Gordin, M. L.; Chen, S.; Wang, D. *Adv. Energy Mater.* **2013,** 3, (3), 295-300.

43.	Bang, B. M.; Kim, H.; Song, H.-K.; Cho, J.; Park, S. *Energy Environ. Sci.* **2011,** 4, (12), 5013-5019.

44.	Bang, B. M.; Lee, J. I.; Kim, H.; Cho, J.; Park, S. *Adv. Energy Mater.* **2012,** 2, (7), 878-883.

45.	Li, Y.; Yan, K.; Lee, H.-W.; Lu, Z.; Liu, N.; Cui, Y. *Nat. Energy* **2016,** 1, 15029.

46.	Choi, S.; Kwon, T.-w.; Coskun, A.; Choi, J. W. *Science* **2017,** 357, (6348), 279-283.

47.   Xu, K., SECONDARY BATTERIES – LITHIUM RECHARGEABLE SYSTEMS | Electrolytes: Overview. In *Encyclopedia of Electrochemical Power Sources*, Garche, J., Ed. Elsevier: Amsterdam, 2009; pp 51-70.

48.   Marassi, R.; Nobili, F., MEASUREMENT METHODS | Structural and Chemical Properties: Scanning Electron Microscopy. In *Encyclopedia of Electrochemical Power Sources*, Garche, J., Ed. Elsevier: Amsterdam, 2009; pp 758-768.

49.   Marassi, R.; Nobili, F., MEASUREMENT METHODS | Structural and Chemical Properties: Transmission Electron Microscopy. In *Encyclopedia of Electrochemical Power Sources*, Garche, J., Ed. Elsevier: Amsterdam, 2009; pp 769-789.

50.   Jacobsson, P.; Johansson, P., MEASUREMENT METHODS | Vibrational Properties: Raman and Infra Red. In *Encyclopedia of Electrochemical Power Sources*, Garche, J., Ed. Elsevier: Amsterdam, 2009; pp 802-812.

51.   Lin, Y.-M.; Klavetter, K. C.; Abel, P. R.; Davy, N. C.; Snider, J. L.; Heller, A.; Mullins, C. B. *Chemical Communications* **2012,** 48, (58), 7268-7270.

52.   Talaie, E.; Bonnick, P.; Sun, X.; Pang, Q.; Liang, X.; Nazar, L. F. *Chem. Mater.* **2016,** 29, (1), 90-105.

53.   Martin, C. *Nat. Nanotechnol.* **2014,** 9, (5), 327-328.

54.   Armand, M.; Tarascon, J. M. *Nature* **2008,** 451, (7179), 652-657.

55.   Choi, N.-S.; Chen, Z.; Freunberger, S. A.; Ji, X.; Sun, Y.-K.; Amine, K.; Yushin, G.; Nazar, L. F.; Cho, J.; Bruce, P. G. *Angewandte Chemie International Edition* **2012,** 51, (40), 9994-10024.

56.   Zhang, W.-J. *J. Power Sources* **2011,** 196, (1), 13-24.

57.   Chan, C. K.; Peng, H. L.; Liu, G.; McIlwrath, K.; Zhang, X. F.; Huggins, R. A.; Cui, Y. *Nat. Nanotechnol.* **2008,** 3, (1), 31-35.

58.   Su, X.; Wu, Q. L.; Li, J. C.; Xiao, X. C.; Lott, A.; Lu, W. Q.; Sheldon, B. W.; Wu, J. *Adv. Energy Mater.* **2014,** 4, (1), 1300882.

59.   Wu, H.; Cui, Y. *Nano Today* **2012,** 7, (5), 414-429.

60.   Chan, C. K.; Ruffo, R.; Hong, S. S.; Cui, Y. *J. Power Sources* **2009,** 189, (2), 1132-1140.

61.   Szczech, J. R.; Jin, S. *Energy Environ. Sci.* **2011,** 4, (1), 56-72.

62.   Huggins, R. A. *J. Power Sources* **1999,** 81–82, (0), 13-19.

63.   Besenhard, J. O.; Yang, J.; Winter, M. *J. Power Sources* **1997,** 68, (1), 87-90.

64.   Beaulieu, L. Y.; Eberman, K. W.; Turner, R. L.; Krause, L. J.; Dahn, J. R. *Electrochem. Solid-State Lett.* **2001,** 4, (9), A137-A140.

65.   Park, C.-M.; Kim, J.-H.; Kim, H.; Sohn, H.-J. *Chemical Society Reviews* **2010,** 39, (8), 3115-3141.

66.   Simon, G.; Goswami, T. *Metall and Mat Trans A* **2011,** 42, (1), 231-238.

67.   Magasinski, A.; Dixon, P.; Hertzberg, B.; Kvit, A.; Ayala, J.; Yushin, G. *Nature Materials* **2010,** 9, (5), 461-461.

68.   Ko, M.; Chae, S.; Jeong, S.; Oh, P.; Cho, J. *ACS Nano* **2014,** 8, (8), 8591-8599.

69.   Li, X.; Gu, M.; Hu, S.; Kennard, R.; Yan, P.; Chen, X.; Wang, C.; Sailor, M. J.; Zhang, J.-G.; Liu, J. *Nat. Commun.* **2014,** 5, 4105.

70.   Hassan, F. M.; Chabot, V.; Elsayed, A. R.; Xiao, X.; Chen, Z. *Nano Lett.* **2013,** 14, (1), 277-283.

71.   Hassan, F. M.; Elsayed, A. R.; Chabot, V.; Batmaz, R.; Xiao, X.; Chen, Z. *ACS Applied Materials & Interfaces* **2014,** 6, (16), 13757-13764.

72.   Marcano, D. C.; Kosynkin, D. V.; Berlin, J. M.; Sinitskii, A.; Sun, Z.; Slesarev, A.; Alemany, L. B.; Lu, W.; Tour, J. M. *ACS Nano* **2010,** 4, (8), 4806-4814.

73.   te Velde, G.; Baerends, E. J. *Physical Review B* **1991,** 44, (15), 7888-7903.

74.   Wiesenekker, G.; Baerends, E. J. *Journal of Physics: Condensed Matter* **1991,** 3, (35), 6721.

75.   Grimme, S.; Antony, J.; Ehrlich, S.; Krieg, H. *The Journal of Chemical Physics* **2010,** 132, (15), 154104.

76.   Li, Y.; Chen, Z. *The Journal of Physical Chemistry Letters* **2012,** 4, (2), 269-275.

77.   Arabi, A. A.; Becke, A. D. *The Journal of Chemical Physics* **2012,** 137, (1), 014104.

78.   Arbab, S.; Mirbaha, H.; Zeinolebadi, A.; Nourpanah, P. *Journal of Applied Polymer Science* **2014,** 131, (11), 40343.

79.   Korobeinyk, A. V.; Whitby, R. L. D.; Mikhalovsky, S. V. *European Polymer Journal* **2012,** 48, (1), 97-104.

80.   Wang, Y.-X.; Wang, C.-G.; Wu, J.-W.; Jing, M. *Journal of Applied Polymer Science* **2007,** 106, (3), 1787-1792.

81.   Wangxi, Z.; Jie, L. *J. Wuhan Univ. Technol.-Mat. Sci. Edit.* **2006,** 21, (1), 26-28.

82.   Wang, H.; Maiyalagan, T.; Wang, X. *ACS Catalysis* **2012,** 2, (5), 781-794.

83.   Takahagi, T.; Shimada, I.; Fukuhara, M.; Morita, K.; Ishitani, A. *Journal of Polymer Science Part A: Polymer Chemistry* **1986,** 24, (11), 3101-3107.

84.   Choi, C. H.; Park, S. H.; Woo, S. I. *Green Chem.* **2011,** 13, (2), 406-412.

85.   Wohlgemuth, S.-A.; Vilela, F.; Titirici, M.-M.; Antonietti, M. *Green Chem.* **2012,** 14, (3), 741-749.

86.   Paraknowitsch, J. P.; Thomas, A.; Schmidt, J. *Chemical Communications* **2011,** 47, (29), 8283-8285.

87.   Morgan, W. E.; Van Wazer, J. R. *Journal of Physical Chemistry* **1973,** 77, (7), 964-969.

88.   Yang, S.; Zhi, L.; Tang, K.; Feng, X.; Maier, J.; Müllen, K. *Advanced Functional Materials* **2012,** 22, (17), 3634-3640.

89.   Higgins, D.; Hoque, M. A.; Seo, M. H.; Wang, R.; Hassan, F.; Choi, J.-Y.; Pritzker, M.; Yu, A.; Zhang, J.; Chen, Z. *Advanced Functional Materials* **2014,** 24, (27), 4325-4336.

90.   Higgins, D. C.; Hoque, M. A.; Hassan, F.; Choi, J.-Y.; Kim, B.; Chen, Z. *ACS Catalysis* **2014,** 4, (8), 2734-2740.

91.   Yang, Z.; Yao, Z.; Li, G.; Fang, G.; Nie, H.; Liu, Z.; Zhou, X.; Chen, X. a.; Huang, S. *ACS Nano* **2011,** 6, (1), 205-211.

92.   Yubero, F.; Holgado, J. P.; Barranco, A.; González-Elipe, A. R. *Surface and Interface Analysis* **2002,** 34, (1), 201-205.

93.   Yu, Y.; Tang, Z.; Jiang, Y.; Wu, K.; Wang, E. *Surface Science* **2006,** 600, (22), 4966-4971.

94.   Grosvenor, A. P.; Biesinger, M. C.; Smart, R. S. C.; McIntyre, N. S. *Surface Science* **2006,** 600, (9), 1771-1779.
95.   Haas, A. *Angewandte Chemie International Edition* **1965,** 4, (12), 1014-1023.
96.   Lai, Y.-H.; Yeh, C.-T.; Lin, Y.-H.; Hung, W.-H. *Surface Science* **2002,** 519, (1–2), 150-156.
97.   Azhakar, R.; Ghadwal, R. S.; Roesky, H. W.; Mata, R. A.; Wolf, H.; Herbst-Irmer, R.; Stalke, D. *Chemistry A European Journal* **2013,** 19, (11), 3715-3720.
98.   Coulter, S. K.; Schwartz, M. P.; Hamers, R. J. *The Journal of Physical Chemistry B* **2001,** 105, (15), 3079-3087.
99.   Liu, B.; Soares, P.; Checkles, C.; Zhao, Y.; Yu, G. *Nano Lett.* **2013,** 13, (7), 3414-3419.
100.   Key, B.; Morcrette, M.; Tarascon, J.-M.; Grey, C. P. *Journal of the American Chemical Society* **2010,** 133, (3), 503-512.
101.   Rochefort, A.; Salahub, D. R.; Avouris, P. *Chemical Physics Letters* **1998,** 297, (1–2), 45-50.
102.   McDowell, M. T.; Lee, S. W.; Nix, W. D.; Cui, Y. *Adv. Mater.* **2013,** 25, (36), 4966-4985.
103.   Hatchard, T.; Dahn, J. *J. Electrochem. Soc.* **2004,** 151, (6), A838-A842.
104.   Wu, H.; Chan, G.; Choi, J. W.; Yao, Y.; McDowell, M. T.; Lee, S. W.; Jackson, A.; Yang, Y.; Hu, L.; Cui, Y. *Nat. Nanotechnol.* **2012,** 7, (5), 310-315.
105.   Cui, L.-F.; Ruffo, R.; Chan, C. K.; Peng, H.; Cui, Y. *Nano Lett.* **2008,** 9, (1), 491-495.
106.   Sim, S.; Oh, P.; Park, S.; Cho, J. *Adv. Mater.* **2013,** 25, (32), 4498-4503.
107.   Kim, I.-S.; Kumta, P. N. *J. Power Sources* **2004,** 136, (1), 145-149.
108.   Wang, G.; Yao, J.; Liu, H. *Electrochem. Solid-State Lett.* **2004,** 7, (8), A250-A253.
109.   Chen, X.; Li, X.; Ding, F.; Xu, W.; Xiao, J.; Cao, Y.; Meduri, P.; Liu, J.; Graff, G. L.; Zhang, J.-G. *Nano Lett.* **2012,** 12, (8), 4124-4130.
110.   Wang, C.; Wu, G.; Zhang, X.; Qi, Z.; Li, W. *J. Electrochem. Soc.* **1998,** 145, (8), 2751-2758.
111.   Zhang, Y.; Zhang, X.; Zhang, H.; Zhao, Z.; Li, F.; Liu, C.; Cheng, H. *Electrochim. Acta* **2006,** 51, (23), 4994-5000.
112.   Holland, G.; Lollar, B. S.; Li, L.; Lacrampe-Couloume, G.; Slater, G.; Ballentine, C. *Nature* **2013,** 497, (7449), 357-360.
113.   Anders, M. H.; Laubach, S. E.; Scholz, C. H. *J. Struct. Geol.* **2014,** 69, 377-394.
114.   Stanchits, S.; Mayr, S.; Shapiro, S.; Dresen, G. *Tectonophysics* **2011,** 503, (1), 129-145.
115.   Rahaman, M. S. A.; Ismail, A. F.; Mustafa, A. *Polym. Degrad. Stab.* **2007,** 92, (8), 1421-1432.
116.   Ouyang, Q.; Cheng, L.; Wang, H.; Li, K. *Polym. Degrad. Stab.* **2008,** 93, (8), 1415-1421.
117.   Arbab, S.; Zeinolebadi, A. *Polym. Degrad. Stab.* **2013,** 98, (12), 2537-2545.
118.   Xue, T. J.; McKinney, M. A.; Wilkie, C. A. *Polym. Degrad. Stab.* **1997,** 58, (1), 193-202.

119.   Scardera, G.; Puzzer, T.; Conibeer, G.; Green, M. *J. Appl. Phys.* **2008,** 104, (10), 104310.

120.   Jansen, R.; Van Bekkum, H. *Carbon* **1995,** 33, (8), 1021-1027.

121.   Chan, C. K.; Peng, H.; Liu, G.; McIlwrath, K.; Zhang, X. F.; Huggins, R. A.; Cui, Y. *Nat. Nanotechnol.* **2008,** 3, (1), 31-35.

122.   Yao, Y.; McDowell, M. T.; Ryu, I.; Wu, H.; Liu, N.; Hu, L.; Nix, W. D.; Cui, Y. *Nano Lett.* **2011,** 11, (7), 2949-2954.

123.   Wu, M.; Sabisch, J. E.; Song, X.; Minor, A. M.; Battaglia, V. S.; Liu, G. *Nano Lett.* **2013,** 13, (11), 5397-5402.

124.   Lu, Z.; Liu, N.; Lee, H.-W.; Zhao, J.; Li, W.; Li, Y.; Cui, Y. *Acs Nano* **2015,** 9, (3), 2540-2547.

125.   Li, X.; Yan, C.; Wang, J.; Graff, A.; Schweizer, S. L.; Sprafke, A.; Schmidt, O. G.; Wehrspohn, R. B. *Adv. Energy Mater.* **2015,** 5, (4).

126.   Kim, H.; Han, B.; Choo, J.; Cho, J. *Angew. Chem.* **2008,** 120, (52), 10305-10308.

127.   Wang, C.; Wu, H.; Chen, Z.; McDowell, M. T.; Cui, Y.; Bao, Z. *Nature Chem.* **2013,** 5, (12), 1042.

128.   Devasia, R.; Nair, C.; Sivadasan, P.; Katherine, B.; Ninan, K. *Journal of Applied Polymer Science* **2003,** 88, (4), 915-920.

129.   Ribeiro, R. F.; Pardini, L. C.; Alves, N. P.; Júnior, B.; Rios, C. A. *Polimeros* **2015,** 25, (6), 523-530.

130.   Ferrari, A. C.; Meyer, J.; Scardaci, V.; Casiraghi, C.; Lazzeri, M.; Mauri, F.; Piscanec, S.; Jiang, D.; Novoselov, K.; Roth, S. *Phys. Rev. Lett.* **2006,** 97, (18), 187401.

131.   Sun, C.-F.; Zhu, H.; Okada, M.; Gaskell, K.; Inoue, Y.; Hu, L.; Wang, Y. *Nano Lett.* **2014,** 15, (1), 703-708.

132.   Sun, X.; Liu, H.; Cheng, H. *RSC Advances* **2017,** 7, (75), 47833-47839.

133.   Liao, X.; Ding, Y.; Chen, L.; Ye, W.; Zhu, J.; Fang, H.; Hou, H. *Chemical Communications* **2015,** 51, (50), 10127-10130.

134.   Feng, K.; Ahn, W.; Lui, G.; Park, H. W.; Kashkooli, A. G.; Jiang, G.; Wang, X.; Xiao, X.; Chen, Z. *Nano Energy* **2016,** 19, 187-197.

135.   Li, J.; Lewis, R.; Dahn, J. *Electrochem. Solid-State Lett.* **2007,** 10, (2), A17-A20.

136.   Yue, L.; Zhang, L.; Zhong, H. *J. Power Sources* **2014,** 247, 327-331.

137.   Koo, B.; Kim, H.; Cho, Y.; Lee, K. T.; Choi, N. S.; Cho, J. *Angew. Chem.* **2012,** 124, (35), 8892-8897.